Studies of the structure and function of Mms6, a bacterial protein that promotes the formation of magnetic nanoparticles

by

Lijun Wang

A dissertation submitted to the graduate faculty

in partial fulfillment of the requirements for the degree of

DOCTOR OF PHILOSOPHY

Major: Biochemistry

Program of Study Committee:
Marit Nilsen-Hamilton, Major Professor
Gaya Amarasinghe
Alan DiSpirito
Surya Mallapragada
Monica Lamm

Iowa State University

Ames, Iowa

2011

TABLE OF CONTENTS

CHAPER 1: GENERAL INTRODUCTION

Dissertation Organization

This dissertation contains 4 chapters. Chapter 1 is a general introduction of the information related to the structural and functional studies of Mms6 protein presented in this dissertation. A detailed literature review of magnetotactic bacteria and magnetotaxis is given first that is followed by an introduction of the formation of magnetosomes and bacterial magnetites. The current understanding of Mms6 protein and its function in bacterial magnetite formation is then discussed. The chapter concludes with a general discussion of the other two major biomineralization systems in living organisms.

Chapter 2 is a manuscript to be submitted to The Journal of Biological Chemistry. In the manuscript, we reported biochemical and biophysical studies of the ferric ion binding pattern of Mms6 protein and reported the discovery of a slow conformational change of Mms6 upon binding of ferric ion. A model of how Mms6 promotes formation of bacterial magnetic nanoparticles is proposed. The co-authors are Lijun Wang (conducted most of the studies described in this manuscript and wrote the manuscript), Shuren Feng (conducted the time-dependent structural change studies of Mms6 protein upon ferric ion binding by fluorescence spectroscopy), Pierre Palo (Expressed and purified the protein samples used in this study), Bruce Fulton (conducted all the NMR spectroscopy studies) and Marit Nilsen-Hamilton (corresponding author, mentored Lijun Wang, Shuren Feng,

initiated the project, oversaw the project including data analysis and revised the manuscript).

Chapter 3 is a manuscript prepared for the submission to The Journal of Biological Chemistry. In this manuscript we reported that the formation of magnetic nanoparticle is associated with the periodical structural change that involves the quaternary structure of Mms6. We also report the discovery of a ferric reductase activity of the C-terminus of Mms6 protein indicates that the reduction of ferric to ferrous iron maybe part of the mechanism of crystal packing. The coauthors are Lijun Wang (studies of the quaternary structure of Mms6 and ferric reductase studies), Shuren Feng (all the fluorescence spectroscopy studies), Pierre Palo (expressed and purified the protein samples), Tanya Prozorov (TEM imaging and magnetic property measurements), Xunpei Liu (magnetite synthesis), Wenjie Wang and David Vaknin (surface fluorescence study and related data analysis), Bruce Fulton (NMR spectroscopy study), Surya Mallapragada (mentored Xunpei Liu and Tanya Prozorov, initiated and oversaw the TEM and polymer aspects of the project, PI on the grant funding the project) and Marit Nilsen-Hamilton (corresponding author, mentored Lijun Wang, Shuren Feng, initiated the project, oversaw the project including data analysis). Contributions to the writing of the manuscript were made by Lijun Wang, Tanya Prozorov, Wenjie Wang and Marit Nilsen-Hamilton with the major contributions being by Lijun Wang and Marit Nilsen-Hamilton.

Chapter 4 is the general conclusions and perspective towards the future direction.

Literature review

Magnetoreception is a sensory system that provides the orientation, navigation, and homing traits for some creatures from bacteria to higher vertebrates (Kirschvink, Walker et al. 2001). The physical basis of this response is thought to be the nanoparticles of single-domain magnetite (Diebel, Proksch et al. 2000). These nanoparticles have been found in fish, pigeons, honeybees, and even in human brains (Kirschvink, Kobayashi-Kirschvink et al. 1992; Diebel, Proksch et al. 2000; Kirschvink, Walker et al. 2001). It is believed that they are responsible for the direction-sensing behaviors of these organisms. The mechanisms regarding biomineralization remain unclear and are under intensive investigation.

Magnetite nanoparticles have been used for drug delivery, magnetic resonance imaging, and array-based assay (Valenti, Rampa et al. 1998; Osaka, Matsunaga et al. 2006). To provide effective nanoparticles for these applications, efforts have focused on their synthesis and characterization of such magnetite nanoparticles in gel matrices, from bacteria or using protein cages (Breulmann, Cöfen et al. 1998; Valenti, Rampa et al. 1998; Okuda, Iwahori et al. 2003). These efforts are strengthened when the mechanism of nanoparticles formation is understood. Magnetotactic bacteria, which can synthesize magnetic nanoparticles *in vivo*, are ideal candidates for studying mechanism (s) of biomineralization.

Magnetotactic Bacteria and Magnetotaxis

Many highly ordered mineralized structures created by living organisms are often hierarchical in structure with fundamental structural elements at nanometer scales. The ability to fabricate such fundamental structures independently of these organisms could open many new and exciting opportunities in nanotechnology. Magnetotactic bacteria provide the ideal model for the studies of biomineralization mechanisms and biomimetic materials.

Magnetotactic bacteria are aquatic prokaryotes that can orient themselves along the local geomagnetic field to find the optimal microaerobic environments for them to live. The first report regarding magnetotactic bacteria was published in 1975 (Blakemore 1975). The first strain of magnetotactic bacteria reported was found in marine sediments. The most intriguing feature of these bacteria is the ability of moving in a magnetic field as weak as 0.5 gauss (Blakemore 1975; Blakemore, Maratea et al. 1979).

After the discovery of the first magnetotactic bacterial strain, a series of magnetotactic bacterial strains have been reported from marine and fresh water (Blakemore, Maratea et al. 1979; Frankel, Blakemore et al. 1979; Blakemore 1982; Schüler 2008). The cellular morphologies of magnetotactic bacteria vary from “cocoid, rod-shaped, helical to even multicellular” (Blakemore 1982; Bazylinski and Frankel 2004).

Despite the diversity of cellular morphologies, magnetotactic bacteria share some common features: All magnetotactic bacteria reported to date are gram-negative bacteria. They have flagella and can move under the direction of the local geomagnetic field. They all have unique intracellular compartments, which are the magnetosomes. When moving, all magnetotactic bacteria have a migration preference for a low oxygen concentration environment (Bazylinski and Frankel 2004).

Magnetotactic bacteria discovered to date fall into three general categories: Obligate microaerophiles, anaerobes or both (Bazylinski and Frankel 2004). In an aqueous environment, they constitute a large portion of the bacterial population in the oxic-anoxic interface (Frankel, Bazylinski et al. 1997; Bazylinski and Frankel 2004). Magnetotactic bacteria are very sensitive to the environmental oxygen concentration and most of them can only synthesize magnetosomes in a very narrow range of low oxygen concentrations: Generally, if the initial oxygen concentration in the atmosphere of sealed cultures is higher than 6%, these bacteria cannot synthesize magnetites (Blakemore, Maratea et al. 1979; Frankel, Blakemore et al. 1979; Bazylinski and Frankel 2004). This fastidious growth requirement of magnetotactic bacteria has limited the progress in this research field for many years and the number of pure cultured strains is still very small (Bazylinski and Frankel 2004).

The term ‘magnetotaxis’ was first used by R.P. Blakemore to describe the responses of magnetotactic bacteria to external magnetic fields (Blakemore 1982).

As Blakemore claimed, “The term of magnetotactic bacteria is only a descriptor and has no taxonomic meaning. Magnetotaxis denotes cell mobility directed by a magnetic field” (Blakemore 1982). In fact, the response of magnetotactic bacteria to external magnetic fields can be more accurately described as ‘magneto-aerotaxis’ rather than ‘magnetotaxis’ (Frankel, Bazylinski et al. 1997). As the term magneto-aerotaxis implies, the magnetic response of magnetotactic bacteria to the external field aligns cells along the magnetic field line, while the sensitivity of cells to the oxygen concentration or redox gradients determines the direction of their migration (Frankel, Bazylinski et al. 1997; Komeili 2007). Now, the term magnetotaxis is used as an abbreviation of magneto-aerotaxis.

Since the report of the first magnetotactic bacterial strain (Blakemore 1975), different strains of magnetotactic bacteria have been found globally. Different strains of magnetotactic bacteria exhibit interesting migration patterns under local geomagnetic fields: Magnetotactic bacteria discovered in the Northern Hemisphere have a preferred migration pattern parallel to the magnetic field, exhibit a northward migration in the geomagnetic field, and are termed north-seeking (NS) magnetotactic bacteria (Blakemore 1975). Magnetotactic bacteria discovered in the Southern Hemisphere have a preferred migration pattern anti-parallel to the magnetic field, exhibit a southward migration in the geomagnetic field, and are termed south-seeking (SS) magnetotactic bacteria (Blakemore, Frankel et al. 1980). Amongst the magnetotactic bacteria discovered in the environments near the geomagnetic equator,

both south-seeking and north-seeking magnetotactic bacteria are equally distributed (Frankel, Blakemore et al. 1981).

To explain these observations of north and south seeking bacteria, Blakemore proposed the original model of magnetotaxis: The geomagnetic field line is tilted downward from the horizon in the Northern Hemisphere and upward in the Southern Hemisphere. Therefore, NS magnetotactic bacteria in the Northern Hemisphere and SS magnetotactic bacteria in the Southern Hemisphere actually both move downwards along the tilted geomagnetic field lines. Magnetotaxis provide the guidance for the migration of cells to low oxygen concentration sediments, where they are believed to stop swimming and adhere to the sediment particles (Blakemore 1975; Blakemore 1982; Bazylinski and Frankel 2004). This hypothesis is consistent with the distribution of NS and SS magnetotactic bacteria on the geosphere (Blakemore 1975; Blakemore, Frankel et al. 1980; Frankel, Blakemore et al. 1981; Bazylinski and Frankel 2004).

However, this original model regarding magnetotaxis in magnetotactic bacteria has some drawbacks: First, this hypothesis did not give a convincing explanation for the benefit magnetotaxis can bring to the magnetotactic bacteria in anoxic aqueous environments. Second, this hypothesis cannot explain how magnetotactic coccoid bacteria form microaerophilc bands in semi-solid, oxygen-gradient media (Bazylinski and Frankel 2004). The facts that large populations of magnetotactic bacteria are discovered at the ‘oxic-anoxic’ interface of aqueous environment and some

magnetotactic coccoid bacterial strains are obligate microaerophiles (Blakemore, Frankel et al. 1980; Frankel, Bazylinski et al. 1997) led to the birth of the term ‘magneto-aerotaxis’, which is thought to be a more accurate description of the unique trait of magnetotactic bacteria (Frankel, Bazylinski et al. 1997). In the proposed ‘magneto-aerotaxis’ model, the magnetotactic bacteria use a two-state sensor machinery to regulate the sense of flagellar rotation (clockwise or counterclockwise) and therefore determine the direction of motion in response to lower or higher oxygen concentration (Frankel, Bazylinski et al. 1997; Faivre and Schüler 2008). This two-state sensor machinery is clearly more efficient than the conventional ‘run-and-tumble’ motion used by *E.coli* and other nonmagnetic bacteria in response to a vertical oxygen gradients found in chemically stratified sediments or water bodies (Smith, Sheehan et al. 2006; Faivre and Schüler 2008). Although this model has been experimentally proven for magnetic coccus strain MC-1 which can migrate in either direction along the external magnetic field to find and maintain their position at their preferred oxygen concentration (Frankel, Bazylinski et al. 1997), it is still unclear whether this model applies to all the magnetotactic bacteria.

In their report describing the magneto-aerotactic trait of magnetotactic bacteria, Frankel et al. investigated the migration patterns in capillary tubes of various strains of NS magnetotactic bacteria in oxygen-concentration gradients. The results showed the joint effects of magnetotaxis and aerotaxis in the magnetotactic bacterial strains investigated (Frankel, Bazylinski et al. 1997). In an aqueous environment,

these magnetotactic bacteria usually migrate towards one direction (north). However, these NS magnetotactic bacteria reversed the direction of their movements towards the higher oxygen concentration when they were put in an oxygen concentration lower than the optimal oxygen concentration required for their growth (Frankel, Bazylinski et al. 1997; Bazylinski and Frankel 2004).

The current explanation of the function and mechanism of magnetotaxis is that magnetotactic bacteria use magnetosomes aligned in chains inside themselves to act as compass needles to direct their migration downwards along the tilted geomagnetic line to find the optimal microaerobic or anaerobic environment for their growth. The magnetotactic trait of magnetotactic bacteria can simplify their search for the preferred microaerobic or anaerobic condition to a two dimensional rather than a random three dimensional search (Blakemore 1975; Frankel, Bazylinski et al. 1997; Bazylinski and Frankel 2004; Komeili 2007). Recent results also demonstrated that magnetotactic bacteria move more quickly and efficiently towards the preferred microaerobic or anaerobic in an applied magnetic field (Smith, Sheehan et al. 2006).

Recently, a novel species of SS magnetotactic bacteria has been found in the Northern Hemisphere (Simmons, Bazylinski et al. 2006). Magnetotactic bacteria with opposing polarities were found coexisting in the same redox environment found in the Northern Hemisphere and the percentage of magnetotactic bacteria with the south-seeking migration pattern increases with redox potential (Simmons, Bazylinski et al. 2006). These south-seeking magnetotactic bacteria found in the Northern

Hemisphere move upwards along the geomagnetic field lines and towards a higher oxygen level which is away from their preferred microaerobic oxygen environments and is opposite to all previously reported magnetotactic bacterial strains (Simmons, Bazylinski et al. 2006). The exact function and mechanism of magnetotaxis trait in magnetotactic bacteria need further investigation and study.

Magnetosome and Bacterial Magnetite

The magnetosome, another intriguing feature of magnetotactic bacteria, is believed to be the biological basis of the intriguing magnetotactic trait of magnetotactic bacteria. It is even more intriguing in the sense of a prokaryotic intracellular compartment (Murat, Byrne et al. 2010). Magnetosomes, the very unique intracellular structures found in all magnetotactic bacteria, are vesicles each with a magnetite nanocrystal (usually 35 ~ 120 nm in diameter) inside and a lipid bilayer membrane with similar composition as the cytoplasmic membrane (Balkwill, Maratea et al. 1980; Bazylinski and Frankel 2004; Komeili 2007). These vesicles are organized into chains by cytoskeletal filaments and fixed inside the cells (Komeili 2007). The magnetite nanoparticles are the physical basis of the magnetotactic trait and the chain alignment of the magnetosome vesicles is the biological basis for this trait (Frankel and Bazylinski 2006; Komeili 2007).

The term ‘magnetosome’ was first used by Balkwill et al. to describe “the electron-dense particles and their associated bounding layers in magnetotactic bacteria” (Balkwill, Maratea et al. 1980). In this report, the authors observed that

the bacterial magnetites were surrounded by electron-dense layers and speculated that it is a true biological membrane and led to the birth of the term ‘magnetosome’ (Balkwill, Maratea et al. 1980). The authors claimed that individual magnetosomes are linked together to form a chain. The magnetosome chain is fixed to the inner cytoplasmic membrane of the cell (Balkwill, Maratea et al. 1980).

Characterization of the magnetosome membrane was first reported in 1988 by Gorby et al. (Gorby, Beveridge et al. 1988). The magnetosome membrane in *Magnetospirillum maglonetotacticum* strain MS-1 is a lipid bilayer with a 3 - 4 nm thickness. The components of magnetosome membranes are mainly phospholipids, fatty acids and some proteins, which are similar to those found in the cytoplasmic membranes of magnetotactic bacteria (Gorby, Beveridge et al. 1988).

Although the observation that the magnetosome membrane has a similar composition to the cytoplasmic membrane indicates that the magnetosome membrane may originate from the cytoplasmic membrane, there was no clear and conclusive experimental report regarding the molecular mechanism of magnetosome formation until recently (Komeili, Vali et al. 2004; Komeili, Li et al. 2006; Scheffel, Gruska et al. 2006).

One critical question regarding magnetosomes in magnetotactic bacteria since their discovery about 30 years ago is how magnetosome vesicles are formed and aligned into chains. It has been long speculated that the formation and chain alignment of magnetosome vesicles are under genetic control (Bazylinski, Frankel et

al. 1995; Frankel and Bazylinski 2006). However, the systematic and detailed investigation of the molecular mechanisms of magnetosome formation was difficult until recently when the genomes of several magnetotactic bacteria, *Magnetospirillum magneticum* strain AMB-1 (Matsunaga, Okamura et al. 2005), *Magnetospirillum gryphiswaldense* strain MSR-1 (Richter, Kube et al. 2007), *Magnetospirillum magnetotacticum* strain MS-1 (Joint Genome Institute, http://genome.jgi-psf.org/draft_microbes/magma/magma.home.html), and *Magnetospirillum magneticum* strain MC-1 (Joint Genome Institute, http://genome.jgi-psf.org/draft_microbes/magm1/magm1.home.html), were sequenced and annotated (Richter, Kube et al. 2007).

The comparative genomic analysis of these four magnetotactic bacteria reveals that a magnetobacterial core genome of about 891 genes was shared by all four magnetotactic bacteria (Richter, Kube et al. 2007). Among these genes, 28 genes were identified as magnetotactic bacteria-specific genes. These genes include all *mam* (magnetosome membrane) and *mms* (magnetic particle membrane specific) genes (Richter, Kube et al. 2007; Faivre and Schüler 2008; Schüler 2008). In *Magnetospirillum magneticum* strain AMB-1, all these conserved 28 genes are located within a 130 kb genomic magnetosome island (MAI) which contains the majority of magnetosome protein genes, a high percentage of transposase genes and many hypothetical genes (Schübbe, Kube et al. 2003; Ullrich, Kube et al. 2005; Schüler 2008).

In 2004, Komeili et al. used the *Magnetospirillum magneticum* strain AMB-1 as a model system for magnetotactic bacteria and clearly demonstrated that magnetosome vesicles are present before magnetite formation, and that the protein MamA is required for their formation (Komeili, Vali et al. 2004). By using cryo-ultramicrotomy, the authors observed intact chains of empty magnetosome vesicles in magnetotactic bacteria cultured under iron-limited conditions. The result demonstrated that magnetosome vesicles are formed and aligned into chains before magnetite synthesis. Deletion of the *mamA* gene, a gene encoding magnetosome protein MamA, resulted in shorter magnetosome chains (1-5 vesicles per cell) being synthesized inside the cells. Two possible functions of the protein MamA in magnetosome formation were proposed: One function of MamA is that it may be involved in magnetosome assembly. Another possibility is that MamA may be used by magnetotactic bacteria to control the number of magnetosome vesicles they synthesize and therefore the length of magnetosome chains when there is not enough iron available (Komeili, Vali et al. 2004).

In 2006, two research groups reported the functions of protein MamJ and MamK in magnetosome formation in two different *Magnetospirillum* strains using essentially the same approaches and techniques. Komeili et al. investigated the functions of the magnetosome protein MamK in magnetosome formation in the *Magnetospirillum magneticum* strain AMB-1 (Komeili, Li et al. 2006). The authors used electron cryotomography (ECT) to study magnetosome formation. When cells were grown in

iron-limited conditions, empty magnetosome chains were observed (Komeili, Li et al. 2006). The ECT images clearly showed that about 34 % of the magnetosome vesicles were invaginations of the inner membrane and that the remaining 66 % were located close enough to the membrane to be the results of invaginations (Komeili, Li et al. 2006). These results demonstrated that magnetosome vesicles originate from the invagination of the inner cytoplasmic membranes of the cells. Deletion of the mamK gene, a gene encoding the magnetosome protein MamK, disrupted the magnetosome chains and the magnetosome vesicles were dispersed in the cells (Komeili, Li et al. 2006). Complementation of the Δ*mamK* mutant with *mamK*–GFP restored the magnetosome chains (Komeili, Li et al. 2006). The authors thus proposed that the protein MamK may form cytoskeletal filaments that align individual magnetosome vesicles into chains that are fixed in the cell (Komeili, Li et al. 2006). Later, by using immunogold staining and fluorescence microscopy, Pradel et al. demonstrated the authenticity of the MamK filaments and found that the MamK alone can form straight filaments in *Escherichia coli* (Pradel, Santini et al. 2006).

Scheffel et al. investigated the role of the other acidic magnetosome protein MamJ in the formation of magnetosomes in *Magnetospirillum gryphiswaldense* (Scheffel, Gruska et al. 2006). In the deletion mutant of *mamJ*, the magnetosome vesicles clustered together and no longer formed chains. By using *mamJ-eGFP* and electron cryotomography (ECT), the authors demonstrated that the MamJ protein was localized adjacent to a filament that extended through the length of cell. When cells

were cultured under iron-insufficient conditions, empty magnetosome vesicles linked to the linear filament were observed in wild type cells. However, in Δ*mamJ* mutants, empty vesicles were dissociated from the filaments when cultured with insufficient iron (Scheffel, Gruska et al. 2006). The authors proposed a model for magnetosome chain formation: First MamJ links empty magnetosome vesicles to the cytoskeletal filaments formed by MamK inside cells. Then magnetite particle synthesis initiates inside the vesicles. As the magnetite particles continue to grow, the magnetic moments between the particles start to take effect and bring them together, forming stable magnetosome chains (Scheffel, Gruska et al. 2006).

Nearly 35% of all proteins associated with the magnetosome membrane of *Magnetospirillum gryphiswaldense* are MamGFDC proteins (Grünberg, Müller et al. 2004). Recent deletion mutagenesis and complementary analysis of *mamGFDC* operon demonstrated that these major magnetosome membrane proteins are not essential for the biomineralization of bacterial magnetites, but control the size of magnetites (Scheffel, Gardes et al. 2008). The deletion of *mamGFDC* operon failed to completely abolish the formation of bacterial magnetites in *Magnetospirillum gryphiswaldense.* In the deletion mutant of *mamGFDC*, the magnetites formed were only 75% of the wild-type size with irregular morphology. The complementation of the deletion mutant with one, two, and three genes of the *mamGFDC* operon gradually restored the formation of wild-type size bacterial magnetites. The authors thus proposed that the MamGFDC proteins may have partially redundant functions

and control the size of magnetite crystals in a cumulative way (Scheffel, Gardes et al. 2008). The mechanism of this process remains unclear.

In a recent review, Komeili proposed the molecular mechanism of magnetosome formation in the *Magnetospirillum magneticum* Strain AMB-1 (Komeili 2007). This model involves three steps: First, membrane invagination occurs at the inner part of the cytoplasmic membrane of the magnetotactic bacteria. Second, individual invaginations are assembled into a chain by MamK and MamJ. Third, iron is transported into the magnetosome vesicles and the synthesis of magnetite nanocrystals with defined structures is stimulated by Mms6 (Bazylinski and Frankel 2004; Komeili 2007). Recent comprehensive functional analysis of the *mamAB* gene cluster in *Magnetospirillum magneticum* strain AMB-1 identified addition proteins participated in the formation of magnetosome and confirmed that the formation of magnetosome is a step-wise process under strict genetic control (Murat, Quinlan et al. 2010). The formation of magnetosome starts with the invagination of cytoplasmic membrane which requires the action of MamI, MamL, MamQ and MamB proteins. Then the chain assembly of individual invaginations was accomplished by MamK and MamJ protein. MamM, MamN and MamQ proteins appear to participate in the iron uptake process. The size and morphology of bacterial magnetites seem to be under the control of MamGFDC and Mms6 proteins (Arakaki, Webb et al. 2003; Scheffel, Gardes et al. 2008; Murat, Quinlan et al. 2010). In the current model, evidence regarding membrane invagination and magnetosome

vesicle assembly is convincing, but the mechanism of Mms6 stimulated bacterial magnetites formation inside magnetosome vesicles remains unclear.

The chain alignment of the magnetite nanoparticles formed inside the magnetosome vesicles by magnetotactic bacteria is thought to be the physics basis of the magnetotactic trait of magnetotactic bacteria (Penninga, de Waard et al. 1995; Dunin-Borkowski, McCartney et al. 1998; Bazylinski and Frankel 2004). The magnetite particles synthesized by magnetotactic bacteria have high chemical purity. It is the first direct evidence to demonstrate that the presence of magnetites in living organisms may participate in their responses to external magnetic fields (Frankel, Blakemore et al. 1979; Bazylinski and Frankel 2004).

The size of magnetite crystals synthesized by magnetotactic bacteria is within the single-magnetic-domain (SD) size range (Dunlop 1973; Butler and Banerjee 1975). Magnetite particles within the SD size range are permanently magnetic and the magnetic moments remain stable in ambient environments (Bazylinski and Frankel 2004; Komeili 2007). Magnetite particles smaller than the SD size are superparamagnetic and their magnetic moments are not permanent in ambient environments (Bazylinski and Frankel 2004).

Under transmission electron microscopy (TEM), the magnetite particles synthesized by magnetotactic bacteria can be seen as chain(s) within the cell (Blakemore 1975; Frankel, Blakemore et al. 1979; Bazylinski and Frankel 2004). In the first paper investigating the physical properties of bacterial magnetite particles, the

authors assumed that the total magnetic moments of the whole cell were the sum of the magnetic moments of individual SD magnetic particles and had a calculated magnetic moments as $1.3X10^{-12}$ electromagnetic units, which provided enough magnetic moment for cells to align themselves along geomagnetic field lines as low as 0.5 gauss (Frankel, Blakemore et al. 1979). Subsequent light-scattering measurements of magnetic-moment of the *Magnetospirillum magnetotacticum* strain MS-1 (Rosenblatt, Dearaujo et al. 1982), remanence measurements on individual *Aquaspirillum magnetotacticum* ATCC 31632 (Penninga, de Waard et al. 1995) and magnetic force microscopy of the submicron magnetic assembly of the marine magnetotactic vibrio strain MV-1 (Proksch, Schaffer et al. 1995) confirmed this calculation. It has been concluded that the magnetite particles synthesized by magnetotactic bacteria, aligned into chain(s) that are fixed within cells, act as “tiny compass needles” to direct the migration of magnetotactic bacteria (Bazylinski and Frankel 2004). It is the chain-aligned magnetite particles fixed inside the cells that confer the magnetotactic trait on magnetotactic bacteria.

Definitive studies of the chemical composition of magnetite particles synthesized in magnetotactic bacteria had not been possible until the first pure culture of magnetotactic bacteria, *Magnetotactic Spirillium* strain MS-1, was isolated in 1979 (Blakemore, Maratea et al. 1979). By using Mössbauer spectroscopy, Frankel et al. clearly demonstrated that the iron-containing mineral synthesized inside

Magnetotactic Spirillium strain MS-1 is ferromagnetic Fe_3O_4 with an average size (maximum dimension) of about 50 nm (Frankel, Blakemore et al. 1979).

Magnetotactic bacteria usually synthesize ferricmagnetic magnetites (Fe_3O_4). But it has also been reported that in some magnetotactic bacteria, which were discovered in sulphide rich aqueous environments, the iron mineral crystals are present in the form of ferricmagnetic greigite (Fe_3S_4) (Farina, Esquivel et al. 1990; Mann, Sparks et al. 1990). The compositions of iron mineral crystals are strain specific and under strict control by the bacteria (Bazylinski and Frankel 2004). Meldurm and colleagues demonstrated that two cultured magnetotactic bacterial strains, MC-1 and MV-2, which synthesize magnetites inside their magnetosome vesicles, continue to synthesize Fe_3O_4 instead of Fe_3S_4 even when hydrogen sulphide was supplied in the culture medium (Meldrum, Mann et al. 1993; Meldrum, Mann et al. 1993). Only one magnetotactic bacterial strain has been reported that can synthesize both magnetite (Fe_3O_4) and greigite (Fe_3S_4), but the pure culture of this magnetotactic bacterium has not yet been isolated (Bazylizinki, Heywood et al. 1993; Bazylinski, Frankel et al. 1995; Bazylinski and Frankel 2004).

Usually, the size of Fe_3O_4 or Fe_3S_4 synthesized by magnetotactic bacteria ranges from 35 nm to 120 nm but is consistent within each species or strain of magnetotactic bacterium (Bazylinski, Garrattreed et al. 1994). The morphologies of the mineral crystals reported to date fall into three general categories: “roughly cuboidal,

elongated prismatic (roughly rectangular), and tooth-, bullet- or arrowhead-shaped" (Bazylinski and Frankel 2004).

Little is known about the real process and mechanism of magnetite particle synthesis inside magnetotactic bacteria. It has been proposed that it may involve three stages (Frankel, Papaefthymiou et al. 1983; Bazylinski, Frankel et al. 1995; Bazylinski and Frankel 2004): First, ferric ions are taken up by the cells through some specific iron transport systems and then reduced to ferrous ions and transported into the magnetosome vesicles where the magnetite particles are synthesized. Second, ferrous ions are reoxidized to ferric ions and form hydrous ferric oxides. The final stage is reducing one-third of the ferric ions in ferric oxides into ferrous ions and then transforming the hydrous iron oxides into magnetite nanoparticles with defined uniform structures.

From the currently available information, it seems that different magnetotactic bacterial strains adopt different strategies to transport iron into magnetosome vesicles in different redox forms. In the *Magnetospirillum magneticum* Strain AMB-1, it has been reported that iron is transported into magnetosome vesicles in the form of Fe (III). The protein Mag A, which is believed to be a homolog of the cation-efflux protein Kef C in *Escherichia coli*, is involved in iron transport in the *Magnetospirillum magneticum* Strain AMB-1 (Nakamura, Burgess et al. 1995). Studies on iron transport in the *Magnetospirillum magnetotacticum* strain MS-1 demonstrated that Fe (II) is transported into magnetosome vesicles with the aid of

siderophores (Paoletti and Blakemore 1986). In the *Magnetospirillum gryphiswaldense* Strain MSR-1, evidence showed that both ferric and ferrous iron can be taken up into magnetosome vesicles (Schüler and Baeuerlein 1998; Bazylinski and Frankel 2004).

Recently, Faivre et al. systematically studied the magnetite biomineralization pathway in *Magnetospirillum gryphiswaldense* Strain MSR-1 (Faivre, Böttger et al. 2007). The results showed iron was taken up from the environment either as ferric or ferrous ion into the cell through the cytoplasmic membrane of *Magnetospirillum gryphiswaldense* Strain MSR-1. Then a pool of ferric and ferrous iron was then formed at cytoplasmic membrane. The ferric iron was chelated by some unknown organic substrate, while the ferrous iron was sequestered in membrane associated bacterial ferritin. The ferric and ferrous iron then were released and transported into the invaginated magnetosome vesicles by mechanisms as yet unknown. The magnetite formation then was initiated by the fast coprecipitation of ferric and ferrous ions without any precursor phase. The growth and maturation of magnetites appears to be completed in the magnetosome vesicles and controlled by other proteins (Faivre, Böttger et al. 2007). It is unclear whether this magnetite biomineralization process is universal to all magnetotactic bacteria species.

However, another study of the formation of magnetosome in *Magnetospirillum gryphiswaldense* Strain MSR-1 showed contrary results (Staniland, Ward et al. 2007). The magnetosome materials of *Magnetospirillum gryphiswaldense* Strain MSR-1 was

investigated *in vivo* by real-time x-ray magnetic circular dichroism. The authors reported the observation of the formation of full size nanocrystal with nonmagnetic surface layers constituted by hematite (the nonmagnetic precursor of magnetite) within 15 minutes after the formation was initiated. The transformation of hematite to mature magnetite nanoparticles was completed within another 15 minutes. The fact that bacteria only take 30 minutes to synthesize the magnetites suggests that this process may be catalytic as proposed by the authors (Staniland, Ward et al. 2007).

Mms6 Protein and Biomineralization

Mms6, a magnetosome-associated protein, may be the most intriguing protein found in the magnetosome. The Mms6 protein was first reported by Arakaki et al. as a magnetosome membrane-associated protein which is tightly bound to magnetite nanoparticles isolated from the *Magnetospirillum magneticum* strain AMB-1 (Arakaki, Webb et al. 2003). In their report, Arakaki et al. identified several small proteins, Mms5, Mms6, Mms7, Mms13 that were tightly bound to the bacterial synthesized magnetite nanoparticles. The most intriguing feature of Mms6 protein is its ability to promote the formation *in vitro* of magnetite nanoparticles with the similar size and morphology as those made by magnetotactic bacteria (Arakaki, Webb et al. 2003).

Mms5, Mms6, Mms7 and Mms13 have been categorized as proteins tightly bound to the bacterial magnetite nanoparticles. These small proteins are encoded by the *mamCD* and *mms6* gene clusters, which are adjacent to each other in the

Magnetospirillum magneticum strain AMB-1 genome (Grünberg, Wawer et al. 2001; Komeili 2007). Mms5, Mms6 and Mms7 share some common features: They all have a hydrophobic N-terminal domain, which is proposed to be the membrane domain of these proteins, and a hydrophilic C-terminal domain, which may be involved in magnetite nanoparticle formation. Only Mms6 has been reported to promote the formation of magnetite nanoparticles with similar morphology to bacterial magnetites *in vitro* by co-precipitation of ferric and ferrous ion (Arakaki, Webb et al. 2003). But the critical magnetization measurements and structural characterizations of these magnetite particles synthesized in the present of recombinant Mms6 protein were lacking in this report.

In 2007, Prozorov et al. reported magnetization measurements and structural characterization of magnetite nanoparticles synthesized in the presence of recombinant Mms6 protein (Prozorov, Mallapragada et al. 2007). The Mms6 protein was expressed as recombinant protein with a poly-His tag attached to its N-terminus. Genomic DNA was obtained from *Magnetospirillum magneticum* strain AMB-1. The DNA was amplified using primers that are complementary to internal sites on the Mms6 gene coding region. The genomic DNA was amplified using primers that are complementary to internal sites on the Mms6 gene coding region. The primers were designed to amplify the region of the gene corresponding to the mature Mms6 protein. The polymerase chain reaction (PCR) amplicon was cloned into the plasmid pTrcHis TOPO. This cloned expression vector was used to

prepare recombinant mature Mms6 protein. Cells of *E.coli* transformed by Mms6 expression vectors were used to produce His-tagged Mms6. A large fraction of the expressed Mms6 was present in inclusion bodies. The inclusion bodies were dissolved in 8 M urea, and purified by TALON column which specifically binds histidine. The captured His-Mms6 protein was refolded by sequential dialysis against increasingly lower concentrations of urea in 20 mM Tris, 500 mM KCl, 0.2 mM phenylmethanesulfonyl fluoride, 1 mM EDTA, pH 7.5. The His-Mms6 was then dialysis against 2 changes of 20 mM Tris, 100 mM KCl, pH7.5. BSA, ferritin and Lcn2 were used as controls to compare magnetite particles synthesized in the presence of proteins with different iron binding properties. The X-ray powder diffraction pattern of the His-Mms6 derived particles identified them as magnetites. The magnetization measurements and transmission electron microscopy results showed that magnetite particles with defined structures can only be synthesized when Mms6 is present (Prozorov, Mallapragada et al. 2007).

Mms6, or its C-terminal part, promotes the synthesis of cobalt ferrite nanoparticles, which are not known to be present in any living organism (Prozorov, Palo et al. 2007). The authors covalently attached His-Mms6 or the C-terminal part of Mms6 to self-assembling polymers and used the resulting polymers as templates to synthesize cobalt ferrite nanocrystals. The resulting cobalt ferrite nanocrystals exhibited 50 - 80 nm thin hexagon-like structures that are difficult to produce using conventional techniques. The authors proposed that when the self-assembling

polymers were covalently attached with His-Mms6 or its C-terminal part, they may act in a manner similar to the bacterial magnetosome membranes and allow a surface-controlled crystal growth (Prozorov, Palo et al. 2007).

Amemiya et al. reported the synthesis of magnetite nanoparticles by partial oxidation of ferrous hydroxide in the presence of Mms6 (Amemiya, Arakaki et al. 2007). The results showed that cubo-octahedral magnetites with narrow size distribution were formed after ferrous hydroxides were partially oxidized at 90 ℃ in the presence of Mms6 for 4 h. While in the absence of Mms6, only octahedral magnetites with broad size distribution were formed under the same experimental conditions. The authors thus proposed that Mms6 may control the morphology of magnetite to be specifically cubo-octahedral by binding to the specific crystal face of the magnetites thus control the growth of magnetites in the above *in vitro* synthesis (Amemiya, Arakaki et al. 2007).

A study in *Magnetospirillum magnetotacticum* strain MS-1 showed that the cubo-octahedral morphology of MS-1 bacterial magnetites can be disturbed when the cells are grown in the presence of Ni. The cellular content of Mms6 in this case was also decreased. The correlation between the morphology of magnetites and the cellular content of Mms6 indicated that the role Mms6 *in vivo* may be to control the growth of bacterial magnetic nanoparticles (Kundu, Kale et al. 2009). The exact effect of Ni on cellular Mms6 content remains unclear.

Recently, Tanaka et al. reported the *in vivo* study of the effect of Mms6 on the formation bacterial magnetites in *Magnetospirillum magneticum* strain AMB-1 (Tanaka, Mazuyama et al. 2011). In the deletion mutant of the *mms6* gene (*⊿mms6*), only smaller size bacterial magnetites with uncommon crystal faces were observed. While the complementation strains of *⊿mms6* mutant synthesized magnetites similar with the wild type with uniformed cubo-octahedral morphorlogy (Tanaka, Mazuyama et al. 2011). This is the first *in vivo* study that clearly demonstrated that Mms6 can control the morphology and size of bacterial magnetites. Interestingly, deletion of the *mms6* gene resulted in a significant decrease of the amount of Mms5, Mms7, and Mms13 on the surfaces of bacterial magnetites. The authors thus proposed that Mms6 may serve as a scaffold protein to form a protein complex with other Mms proteins and co-locate these proteins onto the bacterial magnetite surface thus control the morphology and size of these nanoparticles (Tanaka, Mazuyama et al. 2011). The authors provided evidence that demonstrated Mms6 may control the morphology and size of magnetites in magnetotactic bacteria by regulating the surface of crystal during crystal growth. But the critical question of how does Mms6 (or the protein complex that includes Mms6) regulate the surface growth of crystals still remains unclear and need further investigation.

The genomic and proteomic studies of *Magnetospirillum magneticum* AMB-1 have identified 48 magnetosome-associated proteins (Matsunaga, Okamura et al. 2005). Mms6 is one of these magnetosome membrane-associated proteins

consisting of 59 amino acids with a hydrophobic N-terminus and hydrophilic C-terminus (Arakaki, Webb et al. 2003). The hydrophilic C-terminal region of Mms6 contain a series of amino acid residues with either hydroxyl or carboxyl groups. The N-terminal domain of Mms6 contains a Leu-Gly-rich region, which is similar to some self-aggregating proteins of other biomineralization systems (Amemiya, Arakaki et al. 2007; Komeili 2007; Faivre and Schüler 2008; Schüler 2008). It has been speculated that the hydroxyl or carboxyl groups in the C-terminus of Mms6 may provide a template for magnetic nanoparticle synthesis and can control the morphology of the magnetite (Arakaki, Webb et al. 2003).

Although a lot of effort has been focused on understanding the mechanism of magnetosome formation by proteomic and genetic approaches, there are very few reports that describe biomineralization mechanism in magnetotactic bacteria or *in vitro* (Faivre, Böttger et al. 2007; Prozorov, Palo et al. 2007; Staniland, Ward et al. 2007; Tanaka, Mazuyama et al. 2011). The detailed mechanism of Mms6 promoted magnetite nanoparticle formation remains unclear.

Calcification and Silicification

In those cases for which there is some understanding of the biological mechanisms involved in biomineralization, proteins have been found responsible for forming the mineral structures. But, the mechanisms by which mineralization proteins function are poorly understood. It has been proposed that the mechanism(s) involved in biomineralization may include the control of size, morphology,

orientation, composition and the location of crystals synthesized by organisms (Gower 2008). The role of proteins in the biomineralization process is critical considering that biomineralization occurs readily under mild physiological conditions compared with the high temperatures and pressures required to achieve the same goals *in vitro*.

Unlike the magnetite formation in magnetotactic bacteria, calcification and silicification are the two major systems used in nature to fabricate hard skeletal tissues and have been under extensive investigation (Bonucci 2009). We can learn from these well studied cases and gain some valuable information in elucidating the mechanism of magnetite formation in magnetotactic bacteria.

Studies of the biomineralization processes that occur in calcification of bone and teeth have extended for decades and yet detailed mechanisms to described these processes still remains ambiguous (Posner and Betts 1975; Cölfen 2010). The key question of calcification in organism, which is whether the bone mineralized by means of ion-based or amorphous precursors, has been debated for decades (Weiner 2006; Grynpas and Omelon 2007; Olszta, Cheng et al. 2007; Cölfen 2010; Mahamid, Aichmayer et al. 2010).

The main function of collagen in bone mineralization is to act as the protein scaffold for the organized arrangement of apatite (Traub, Arad et al. 1989; Hulmes, Wess et al. 1995). Recent *in vitro* and *in vivo* studies have provided evidence to demonstrate that the function of collagen is as an active scaffold involved in bone

mineralization rather than being passive (Dey, Bomans et al. 2010; Mahamid, Aichmayer et al. 2010; Nudelman, Pieterse et al. 2010).

To study the calcium biomineralization process *in vitro,* Dey et al. used an arachidic acid monolayer system to mimic the *in vivo* biological surfaces that induce calcium phosphate biomineralization. By using cryo-TEM, the investigators provided high resolution, time-resolved images of the surface-induced calcium phosphate crystallization. The authors reported existence of small nanometer-sized prenucleation clusters in the concentrated calcium solution in which the biomineralization of calcium phosphate starts. These prenucleation clusters then aggregate and further coalesce on the surface of monolayer to form amorphous spherical small particles. The development of mature crystals was accomplished by the oriented nucleation of amorphous particles directed by the monolayer (Dey, Bomans et al. 2010).

Collagens, the insoluble super macromolecules, are called the structural matrix in bone and teeth biomineralization and usually considered as the inactive protein scaffold. A recent study showed the possible active role of collagens in the process of apatite biomineralization for bone and tooth formation (Nudelman, Pieterse et al. 2010). By using cryo-TEM and molecular modeling of the electrostatic potential energy distribution of the collagen fibril, the authors reported that the prenucleation clusters are stabilized by polyaspartic acid and form negatively charged loosely packed mobile structures. Modeling of the electrostatic potential energy

distribution of the collagen fibrils revealed the existence of positively charged regions at the border of gap and the overlap zone. The authors thus concluded that this positively charge region can be used for mineral infiltration and electrostatic interaction, which enabled the formation of a dense network of prenucleation clusters inside the collagen fibrils. These prenucleation clusters were then transformed into amorphous calcium phosphates and oriented as crystalline hydroxyapatite inside the fibrils. The results showed an active role of collagen for the biomineralization of hydroxyapatite, which was to provide the nucleation sites for hydroxyapatite crystallization within a charged amino acid domain of the collagen fibrils (Cölfen 2010; Nudelman, Pieterse et al. 2010).

Mahamid et al. used zebrafish as the model system to investigate the bone mineralization process *in vivo*. By using cryo-SEM imaging and small-angle scattering, the investigators validated the hypothesis that the *in vivo* process of bone mineralization starts with the aggregation of prenucleation clusters followed by the formation of amorphous apatite calcium phosphates in the collagen fibrils where the maturation of crystalline of apatites occurs (Mahamid, Aichmayer et al. 2010).

The formation of enamel is another well-studied subject in the calcification system, which is the outcome of the mineralization of carbonate-apatite with the most unusual morphology in biological system. Mature enamel contains crystals that are tens of microns in length with a length to width ratio larger than 1000 (Daculsi and Kerebel 1978). The formation of enamel occurs in an extracellular

environment and consists of three main stages: secretory, transition and maturation (Eastoe 1979; Simmer and Fincham 1995). As the development of enamel continues, the extracellular matrix (ECM) proteins are cleaved by various proteases and removed from the mineralization sites in the extracellular matrix, which in turn results in the hardness of enamel (Eastoe 1979; Moradian-Oldak 2001).

Amelogenin, the major component of the extracellular matrix during the secretory stage, is believed to be responsible for the formation of the hierarchical structure in enamel (Eastoe 1979; Moradian-Oldak 2001). Amelogin shares many similarities with Mms6, the protein of focus for this thesis. The sequences of amelogenins from different species are highly conserved at the carboxyl and amino terminal regions. The C-terminus consists of hydrophilic charged amino acid residues and the N-terminus is the TRAP (tyrosine rich amelogenin polypeptide) region. The remaining part of amelogenin is the hydrophobic core which is rich in proline and leucine residues (Moradian-Oldak, Paine et al. 2000). The conserved TRAP region and the hydrophilic C-terminal region are believed to be the functional motifs important for the enamel biomineralization (Simmer and Fincham 1995; Fincham, Leung et al. 1998).

The full length mouse amelogenin has 179 amino acids. Early research results demonstrated that amelogenin can self-assemble into ‘nano-sphere’ structures with a hydrodynamic diameters ranging from 15 to 20 nm *in vitro* (Fincham, Moradian-Oldak et al. 1994). A similar quaternary structure of amelogenin was

observed *in vivo* from high resolution transmission electron microscopy (TEM) studies. The TEM images of the developing enamel from mouse, bovine and hamster showed the amelogenin nano-spheres as 'beaded rows aligned with and separating the enamel crystallites' (Fincham, Moradian-Oldak et al. 1995). It was thus proposed that the nano-sphere structure of amelogenin may function to control the crystallite spacing of enamel which is found to be about 20 nm (Fincham, Moradian-Oldak et al. 1995; Zeichner-David, Diekwisch et al. 1995).

The driven force of the self-assembly of amelogenin nano-spheres seems to be hydrophobic interactions as it is evident in the primary sequence of amelogenin contains a large portion of hydrophobic amino acids. Proteolysis digestion of amelogenin nano-spheres revealed that both the N-terminus and C-terminus of amelogenin are exposed (Moradian-Oldak, Jimenez et al. 2001). Subsequent studies further revealed the formation of higher levels of ordered structures which were termed as 'micro-ribbons' from amelogenin nano-spheres (Du, Falini et al. 2005). The authors reported that the amelogenin monomer forms a bipolar globular structure with the highly negatively charged C-terminus exposed on the surface of molecule. The oligomerization of amelogenin is driven by inter-molecular hydrophobic interactions. The amelogenin forms dimer, trimer and hexamers. The further assembly of the monomeric and multimeric amelogenin molecules results in the formation of stable nano-spheres. These nano-spheres then further self-associate and form linear chain structures made of 10 to 15 nano-spheres. The

bipolar nature of amelogenin has been proposed responsible for the re-organization of the chain structures to eventually result in formation of the micro-ribbon (Du, Falini et al. 2005; Moradian-Oldak, Du et al. 2006).

The C-terminal segment of amelogenin is highly negatively charged. Removal of the C-terminus results in the formation of more loosely organized and larger nano-spheres than formed by the full length amelogenin (Moradian-Oldak, Bouropoulos et al. 2002). A C-terminal deletion mutant of amelogenin failed to form micro-ribbon structures (Du, Falini et al. 2005). More importantly, the affinity of C-terminal deletion mutant of amelogenin to apatite crystals was significantly lower than that of the full length amelogenin (Moradian-Oldak, Bouropoulos et al. 2002). A solid-state nuclear resonance microscopy (SSNMR) study of the LRAP (leucine-rich amelogenin protein, the alternative splicing product of the primary amelogenin transcript) revealed that the C-terminal segment of amelogenin was oriented to the surface of hydroxyapatite (HAP) so that the acidic amino acid residues in the C-terminus can direct interact with the HAP surface direct interaction and regulate mineralization (Shaw, Campbell et al. 2004).

Silicification is another biomineralization process frequently used by organisms to fabricate silica-based hard structures such as diatom walls, sponge spicules and radiolarian micro skeletons in nature (Crookes-Goodson, Slocik et al. 2008; Bonucci 2009). The representative example of silica-based biomineralization process is the silicatein directed silicification by sponges.

Sponges used high concentrations of silicon in the environment to build spicules, which are robust structures of amorphous silica (Crookes-Goodson, Slocik et al. 2008). The sponges are constructed with a central proteinaceous axial filament surrounded by the annular layers of silica nanoparticles (Weaver and Morse 2003). The central proteinaceous axial filaments are composed of three proteins, silicatein α, β and γ (Cha, Shimizu et al. 1999; Weaver and Morse 2003). These three proteins form dimers, tetramers and hexamers respectively and undergo phosphorylation (Müller, Boreiko et al. 2007).

The silicatein filaments function in the biomineralization of silicon as both templates for silica deposition and dehydrolase for silicon ethoxide condensation (Cha, Shimizu et al. 1999; Yan, Katsuhiko et al. 1999). Silicatein shares high sequence homology to cathepsins which are cysteine proteases. Of the catalytic triad of cathepsins, two of amino acid residues, His and Asn, are conserved in silicatein. The mechanism of silicatein-catalyzed polymerization of silica was proposed to resemble the catalytic mechanism of a serine protease. Both the dehydration of silicon ethoxide promoted by the silicatein and the cleavage of peptides catalyzed by serine proteases must precede through an obligatory hydrolysis reaction and both are accelerated by general acid–base catalysis (Cha, Shimizu et al. 1999; Yan, Katsuhiko et al. 1999; Schübbe, Kube et al. 2003). Later, this proposed catalytic mechanism of silicatein directed silicon formation was confirmed by mutagenesis studies (Yan, Katsuhiko et al. 1999).

References

Amemiya, Y., A. Arakaki, et al. (2007). "Controlled formation of magnetite crystal by partial oxidation of ferrous hydroxide in the presence of recombinant magnetotactic bacterial protein Mms6." Biomaterials **28**(35): 5381-5389.

Arakaki, A., J. Webb, et al. (2003). "A novel protein tightly bound to bacterial magnetic particles in Magnetospirillum magneticum strain AMB-1." J. Biol. Chem. **278**(10): 8745-8750.

Balkwill, D. L., D. Maratea, et al. (1980). "Ultrastructure of a magnetotactic spirillum." J. Bacteriol. **141**(3): 1399-1408.

Bazylinski, D. A. and R. B. Frankel (2004). "Magnetosome formation in prokaryotes." Nature Reviews Microbiology **2**(3): 217-230.

Bazylinski, D. A., R. B. Frankel, et al. (1995). "Controlled biomineralization of Magnetite (Fe_3O_4) and Greigite (Fe_3S_4) in a Magnetotactic Bacterium." Appl. Environ. Microbiol. **61**(9): 3232-3239.

Bazylinski, D. A., A. J. Garrattreed, et al. (1994). "Electron-microscopic studies of magnetosomes in magnetotactic bacteria." Microscopy Research and Technique **27**(5): 389-401.

Bazylizinki, D. A., B. R. Heywood, et al. (1993). "Fe_3O_4 and Fe_3S_4 in a bacterium." Nature **366**(6452): 218-218.

Blakemore, R. (1975). "Magnetotactic bacteria." Science **190**: 377-379.

Blakemore, R. P. (1982). "Magnetotactic bacteria." Annual Review of Microbiology **36**(1): 217-238.

Blakemore, R. P., R. B. Frankel, et al. (1980). "South-seeking magnetotactic bacteria in the southern hemisphere." Nature **286**: 384-385.

Blakemore, R. P., D. Maratea, et al. (1979). "Isolation and pure culture of a freshwater magnetic spirillum in chemically defined medium." J. Bacteriol. **140**(2): 720-729.

Bonucci, E. (2009). "Calcification and silicification: a comparative survey of the early stages of biomineralization." Journal of Bone and Mineral Metabolism **27**(3): 255-264.

Breulmann, M., H. Cöfen, et al. (1998). "Elastic magnets: Template-controlled mineralization of iron oxide colloids in a sponge-like gel matrix." Advanced Materials **10**(3): 237-241.

Butler, R. F. and S. K. Banerjee (1975). "Theoretical single-domain grain-size range in magnetite and titanomagnetite." Journal of Geophysical Research **80**(29): 4049-4058.

Cha, J. N., K. Shimizu, et al. (1999). "Silicatein filaments and subunits from a marine sponge direct the polymerization of silica and silicones *in vitro*." PNAS **96**(2): 361-365.

Cölfen, H. (2010). "Biomineralization: A crystal-clear view." Nat Mater **9**(12): 960-1.

Crookes-Goodson, W. J., J. M. Slocik, et al. (2008). "Bio-directed synthesis and assembly of nanomaterials." Chemical Society Reviews **37**(11): 2403-2412.

Daculsi, G. and B. Kerebel (1978). "High-resolution electron microscope study of human enamel crystallites: Size, shape, and growth." Journal of Ultrastructure Research **65**(2): 163-172.

Dey, A., P. H. H. Bomans, et al. (2010). "The role of prenucleation clusters in surface-induced calcium phosphate crystallization." Nat Mater **9**(12): 1010-1014.

Diebel, C. E., R. Proksch, et al. (2000). "Magnetite defines a vertebrate magnetoreceptor." Nature **406**(6793): 299-302.

Du, C., G. Falini, et al. (2005). "Supramolecular assembly of amelogenin nanospheres into birefringent microribbons." Science **307**(5714): 1450-4.

Dunin-Borkowski, R. E., M. R. McCartney, et al. (1998). "Magnetic microstructure of magnetotactic bacteria by electron holography." Science **282**(5395): 1868-1870.

Dunlop, D. J. (1973). "Superparamagnetic and single-domain threshold sizes in magnetite." Journal of Geophysical Research **78**(11): 1780-1793.

Eastoe, J. E. (1979). "Enamel protein chemistry - Past, present and future." Journal of Dental Research **58**(2 suppl): 753-764.

Faivre, D., L. H. Böttger, et al. (2007). "Intracellular magnetite biomineralization in bacteria proceeds by a distinct pathway involving membrane-bound ferritin and an iron(II) species." Angewandte Chemie International Edition **46**(44): 8495-8499.

Faivre, D. and D. Schüler (2008). "Magnetotactic bacteria and magnetosomes." Chemical Reviews **108**(11): 4875-4898.

Farina, M., D. M. S. Esquivel, et al. (1990). "Magnetic iron-sulphur crystals from a magnetotactic microorganism." Nature **343**(6255): 256-258.

Fincham, A. G., W. Leung, et al. (1998). "Does amelogenin nanosphere assembly proceed through intermediary-sized structures?" Connect Tissue Res **38**(1-4): 237-40; discussion 241-6.

Fincham, A. G., J. Moradian-Oldak, et al. (1995). "Evidence for amelogenin "nanospheres" as functional components of secretory-stage enamel matrix." J Struct Biol **115**(1): 50-9.

Fincham, A. G., J. Moradian-Oldak, et al. (1994). "Self-assembly of a recombinant amelogenin protein generates supramolecular structures." J. Struct. Biol. **112**(2): 103-109.

Frankel, R. B. and D. A. Bazylinski (2006). "How magnetotactic bacteria make magnetosomes queue up." Trends in Microbiology **14**(8): 329-331.

Frankel, R. B., D. A. Bazylinski, et al. (1997). "Magneto-aerotaxis in marine coccoid bacteria." Biophys. J. **73**(2): 994-1000.

Frankel, R. B., R. P. Blakemore, et al. (1981). "Magnetotactic bacteria at the geomagnetic equator." Science **212**(4500): 1269-1270.

Frankel, R. B., R. P. Blakemore, et al. (1979). "Magnetite in freshwater magnetotactic bacteria." Science **203**(4387): 1355-1356.

Frankel, R. B., G. C. Papaefthymiou, et al. (1983). "Fe_3O_4 precipitation in magnetotactic bacteria." Biochimica et Biophysica Acta (BBA) - Molecular Cell Research **763**(2): 147-159.

Gorby, Y. A., T. J. Beveridge, et al. (1988). "Characterization of the bacterial magnetosome membrane." Journal of Bacteriology **170**(2): 834-841.

Gower, L. B. (2008). "Biomimetic model systems for investigating the amorphous precursor pathway and its role in biomineralization." Chem. Rev. **108**(11): 4551-4627.

Grünberg, K., E.-C. Müller, et al. (2004). "Biochemical and proteomic analysis of the magnetosome membrane in *Magnetospirillum gryphiswaldense*." Appl. Environ. Microbiol. **70**(2): 1040-1050.

Grünberg, K., C. Wawer, et al. (2001). "A large gene cluster encoding several magnetosome proteins is conserved in different species of magnetotactic bacteria." Appl. Environ. Microbiol. **67**(10): 4573-4582.

Grynpas, M. D. and S. Omelon (2007). "Transient precursor strategy or very small biological apatite crystals?" Bone **41**(2): 162-164.

Hulmes, D. J., T. J. Wess, et al. (1995). "Radial packing, order, and disorder in collagen fibrils." Biophysical Journal **68**(5): 1661-1670.

Kirschvink, J. L., A. Kobayashi-Kirschvink, et al. (1992). "Magnetite biomineralization in the human brain." PNAS **89**(16): 7683-7687.

Kirschvink, J. L., M. M. Walker, et al. (2001). "Magnetite-based magnetoreception." Current Opinion in Neurobiology **11**(4): 462-467.

Komeili, A. (2007). "Molecular mechanisms of magnetosome formation." Annual Review of Biochemistry **76**(1): 351-366.

Komeili, A., Z. Li, et al. (2006). "Magnetosomes are cell membrane invaginations organized by the actin-like protein MamK." Science **311**(5758): 242-245.

Komeili, A., H. Vali, et al. (2004). "Magnetosome vesicles are present before magnetite formation, and MamA is required for their activation." PNAS **101**(11): 3839-3844.

Kundu, S., A. A. Kale, et al. (2009). "On the change in bacterial size and magnetosome features for Magnetospirillum magnetotacticum (MS-1) under high concentrations of zinc and nickel." Biomaterials **30**(25): 4211-4218.

Mahamid, J., B. Aichmayer, et al. (2010). "Mapping amorphous calcium phosphate transformation into crystalline mineral from the cell to the bone in zebrafish fin rays." PNAS **107**(14): 6316-6321.

Mann, S., N. H. C. Sparks, et al. (1990). "Biomineralization of ferrimagnetic greigite (Fe_3S_4) and iron pyrite (FeS_2) in a magnetotactic bacterium." Nature **343**(6255): 258-261.

Matsunaga, T., Y. Okamura, et al. (2005). "Complete genome sequence of the facultative anaerobic magnetotactic bacterium magnetospirillum sp. strain AMB-1." DNA Res **12**(3): 157-166.

Meldrum, F. C., S. Mann, et al. (1993). "Electron-microscopy study of magnetosomes in 2 cultured vibrioid magnetotactic bacteria." Proceedings of the Royal Society of London Series B-Biological Sciences **251**(1332): 237-242.

Meldrum, F. C., S. Mann, et al. (1993). "Electron-microscopy study of magnetosomes in a cultured coccoid magnetotactic bacterium." Proceedings of the Royal Society of London Series B-Biological Sciences **251**(1332): 231-236.

Moradian-Oldak, J. (2001). "Amelogenins: assembly, processing and control of crystal morphology." Matrix Biology **20**(5-6): 293-305.

Moradian-Oldak, J., N. Bouropoulos, et al. (2002). "Analysis of self-assembly and apatite binding properties of amelogenin proteins lacking the hydrophilic C-terminal." Matrix Biology **21**(2): 197-205.

Moradian-Oldak, J., C. Du, et al. (2006). "On the formation of amelogenin microribbons." European Journal of Oral Sciences **114**: 289-296.

Moradian-Oldak, J., I. Jimenez, et al. (2001). "Controlled proteolysis of amelogenins reveals exposure of both carboxy- and amino-terminal regions." Biopolymers **58**(7): 606-16.

Moradian-Oldak, J., M. L. Paine, et al. (2000). "Self-assembly properties of recombinant engineered amelogenin proteins analyzed by dynamic light scattering and atomic force microscopy." J. Struct. Biol. **131**(1): 27-37.

Müller, W. E. G., A. Boreiko, et al. (2007). "Fractal-related assembly of the axial filament in the demosponge Suberites domuncula: Relevance to biomineralization and the formation of biogenic silica." Biomaterials **28**(30): 4501-4511.

Murat, D., M. Byrne, et al. (2010). "Cell biology of prokaryotic organelles." Cold Spring Harbor Perspectives in Biology **2**(10).

Murat, D., A. Quinlan, et al. (2010). "Comprehensive genetic dissection of the magnetosome gene island reveals the step-wise assembly of a prokaryotic organelle." PNAS **107**(12): 5593-5598.

Nakamura, C., J. G. Burgess, et al. (1995). "An iron-regulated gene, magA, encoding an iron transport protein of *Magnetospirillum sp.* strain AMB-1." J. Biol. Chem. **270**(47): 28392-28396.

Nudelman, F., K. Pieterse, et al. (2010). "The role of collagen in bone apatite formation in the presence of hydroxyapatite nucleation inhibitors." Nat Mater **9**(12): 1004-1009.

Okuda, M., K. Iwahori, et al. (2003). "Fabrication of nickel and chromium nanoparticles using the protein cage of apoferritin." Biotechnology and Bioengineering **84**(2): 187-194.

Olszta, M. J., X. Cheng, et al. (2007). "Bone structure and formation: A new perspective." Materials Science and Engineering: R: Reports **58**(3-5): 77-116.

Osaka, T., T. Matsunaga, et al. (2006). "Synthesis of magnetic nanoparticles and their application to bioassays." Analytical and Bioanalytical Chemistry **384**(3): 593-600.

Paoletti, L. C. and R. P. Blakemore (1986). "Hydroxamate production by aquaspirillum-magnetotacticum." Journal of Bacteriology **167**(1): 73-76.

Penninga, I., H. de Waard, et al. (1995). "Remanence measurements on individual magnetotactic bacteria using a pulsed magnetic field." Journal of Magnetism and Magnetic Materials **149**(3): 279-286.

Posner, A. S. and F. Betts (1975). "Synthetic amorphous calcium phosphate and its relation to bone mineral structure." Accounts of Chemical Research **8**(8): 273-281.

Pradel, N., C.-L. Santini, et al. (2006). "Biogenesis of actin-like bacterial cytoskeletal filaments destined for positioning prokaryotic magnetic organelles." Proceedings of the National Academy of Sciences **103**(46): 17485-17489.

Proksch, R. B., T. E. Schaffer, et al. (1995). "Magnetic force microscopy of the submicron magnetic assembly in a magnetotactic bacterium." Applied Physics Letters **66**(19): 2582-2584.

Prozorov, T., S. K. Mallapragada, et al. (2007). "Protein-mediated synthesis of uniform superparamagnetic magnetite nanocrystals." Advanced Functional Materials **17**(6): 951-957.

Prozorov, T., P. Palo, et al. (2007). "Cobalt ferrite nanocrystals: Out-performing magnetotactic bacteria." ACS Nano **1**(3): 228-233.

Richter, M., M. Kube, et al. (2007). "Comparative genome analysis of four magnetotactic bacteria reveals a complex set of group-specific genes implicated in magnetosome biomineralization and function." J. Bacteriol. **189**(13): 4899-4910.

Rosenblatt, C., F. F. T. Dearaujo, et al. (1982). "Light-scattering determination of magnetic-moments of magnetotactic bacteria." Journal of Applied Physics **53**(3): 2727-2729.

Scheffel, A., A. Gardes, et al. (2008). "The major magnetosome proteins MamGFDC are not essential for magnetite biomineralization in *Magnetospirillum*

gryphiswaldense but regulate the size of magnetosome crystals." J. Bacteriol. **190**(1): 377-386.

Scheffel, A., M. Gruska, et al. (2006). "An acidic protein aligns magnetosomes along a filamentous structure in magnetotactic bacteria." Nature **440**(7080): 110-114.

Schübbe, S., M. Kube, et al. (2003). "Characterization of a spontaneous nonmagnetic mutant of *Magnetospirillum gryphiswaldense* reveals a large deletion comprising a putative magnetosome island." J. Bacteriol. **185**(19): 5779-5790.

Schüler, D. (2008). "Genetics and cell biology of magnetosome formation in magnetotactic bacteria." FEMS Microbiology Reviews **32**(4): 654-672.

Schüler, D. and E. Baeuerlein (1998). "Dynamics of iron uptake and Fe_3O_4 biomineralization during aerobic and microaerobic growth of magnetospirillum gryphiswaldense." J. Bacteriol. **180**(1): 159-162.

Shaw, W. J., A. A. Campbell, et al. (2004). "The COOH terminus of the amelogenin, LRAP, is oriented next to the hydroxyapatite surface." J. Biol. Chem. **279**(39): 40263-40266.

Simmer, J. P. and A. G. Fincham (1995). "Molecular mechanisms of dental enamel formation." Critical Reviews in Oral Biology & Medicine **6**(2): 84-108.

Simmons, S. L., D. A. Bazylinski, et al. (2006). "South-seeking magnetotactic bacteria in the Northern Hemisphere." Science **311**(5759): 371-374.

Smith, M. J., P. E. Sheehan, et al. (2006). "Quantifying the magnetic advantage in magnetotaxis." Biophys. J.: biophysj.106.085167.

Staniland, S., B. Ward, et al. (2007). "Rapid magnetosome formation shown by real-time x-ray magnetic circular dichroism." PNAS **104**(49): 19524-19528.

Tanaka, M., E. Mazuyama, et al. (2011). "Mms6 protein regulates crystal morphology during nano-sized magnetite biomineralization *in vivo*." J. Biol. Chem. **286**(8): 6386-6392.

Traub, W., T. Arad, et al. (1989). "Three-dimensional ordered distribution of crystals in turkey tendon collagen fibers." PNAS **86**(24): 9822-9826.

Ullrich, S., M. Kube, et al. (2005). "A hypervariable 130-kilobase genomic region of *Magnetospirillum gryphiswaldense* comprises a magnetosome island which undergoes frequent rearrangements during stationary growth." J. Bacteriol. **187**(21): 7176-7184.

Valenti, P., A. Rampa, et al. (1998). "Biomagnetic nanoparticle formation and application." Supramolecular Science **5**: 391-394.

Weaver, J. C. and D. E. Morse (2003). "Molecular biology of demosponge axial filaments and their roles in biosilicification." Microscopy Research and Technique **62**(4): 356-367.

Weiner, S. (2006). "Transient precursor strategy in mineral formation of bone." Bone **39**(3): 431-433.

Yan, Z., S. Katsuhiko, et al. (1999). "Efficient Catalysis of Polysiloxane Synthesis by Silicatein α Requires Specific Hydroxy and Imidazole Functionalities." Angewandte Chemie International Edition **38**(6): 779-782.

Zeichner-David, M., T. Diekwisch, et al. (1995). "Control of ameloblast differentiation." Int J Dev Biol **39**(1): 69-92.

CHAPTER 2: IRON-DRIVEN STRUCTURAL CHANGE AND IRON ACCUMULATION BY A BACTERIAL PROTEIN THAT PROMOTES THE FORMATION OF MAGNETIC NANOPARTICLES

A manuscript to be submitted to *The Journal of Biological Chemistry*

Lijun Wang[†,¶], Shuren Feng[†,¶], Pierre Palo[†,] D. Bruce Fulton[¶], and Marit Nilsen-Hamilton[†,¶,*]

†Ames Laboratory, U. S. Department of Energy, Ames, Iowa 50011, ¶Department of Biochemistry, Biophysics and Molecular Biology, Iowa State University, Ames, IA 50011

Address correspondence to: Marit Nilsen-Hamilton, 3206 Molecular Biology Building, Dept of Biochemistry, Biophysics and Molecular Biology, Iowa State University, Ames, IA 50011; Phone: 515-294-9996; Fax: 515-294-0453; Email: marit@iastate. edu

Abstract

Highly ordered mineralized structures are created by living organisms that are often hierarchical in structure with fundamental structural elements at nanometer scales. Proteins have been found responsible for forming many mineral structures, but the mechanisms by which biomineralization proteins function are generally poorly understood. We discuss studies of the magnetotactic bacterial protein, Mms6, which promotes the formation *in vitro* of superparamagnetic magnetite nano-

crystals. Mms6 has two phases of iron binding, one high affinity (K_d=10^{-16} M) and stoichiometric and the other low affinity (K_d =5.5 ± 4.0 μM), high capacity, cooperative with respect to iron and temperature sensitive. Iron binding initiates a very slow structural change in the protein. We propose a model for the mechanism of action of Mms6 in which a conformational change driven by iron bound to the C-terminal domain initiates a coordinated structural change involving multiple proteins to form a surface that can accumulate a cluster of iron atoms, which might then be organized into seed crystals.

Introduction

Magnetotactic bacteria are aquatic prokaryotes that can move under the direction of local geomagnetic field lines (1). All magnetotactic bacteria have unique intracellular structures called magnetosomes that consist of magnetic nanoparticles surrounded by lipid bilayer membranes (2-4). The composition, size and morphology of magnetites synthesized by magnetotactic bacteria are genetically-defined (5,6). Magnetotaxis is proposed to simplify the bacterial search for the optimal oxygen environment to a one-dimensional rather than a random three dimensional path (1,5,7,8).

The formation of magnetosomes in bacteria involves membrane invaginations to form vesicles in which iron accumulates and magnetite nanoparticles grow by a controlled mechanism (5). Recent genomic and proteomic studies of

Magnetospirillum magneticum strain AMB-1 have identified 48 magnetosome-associated proteins (9). One of these, Mms6, is a magnetosome membrane-associated protein, the mature form consisting of 59 amino acids (10). Magnetite nanoparticles with similar size and shape to the wild-type bacterial magnetite crystals are formed *in vitro* in the presence of recombinant Mms6 alone (10,11). Deletion of the Mms6 gene from the bacterial genome results in a change in crystal structure of the magnetites formed by these mutant bacteria and a decrease in the number of magnetosome proteins associated with the magnetite nanoparticles (12). Although these results show that Mms6 is not required to promote the formation of iron particles in magnetotactic bacteria, it has not yet been determined if the particles produced by the mutant bacteria have the same magnetic characteristics as the wild-type particles. Thus, it is unclear if Mms6 is required to form magnetic nanoparticles in this strain of magnetotactic bacteria. As well, it is well known that many biological systems that are critical for the organism to survive contain redundancy in the protein required activities. Thus, it remains to be seen to what extent Mms6 is unique in its ability to form magnetic particles in magnetotactic bacteria. However, its ability to do so *in vitro* provides us an opportunity of understanding the mechanism by which this protein can promote the formation of magnetic nanoparticles.

Here, we observed that Mms6 forms a micellar quaternary structure *in vitro* that may provide a surface for magnetite nanoparticle formation. Mms6 consists of two

subdomains, with the N-terminal domain responsible for anchoring the C-terminal domain in a micelle from which the C-terminal domain interacts with iron to form magnetic nanoparticles. Analysis of Mms6 and its C-terminal domain by fluorescence, and NMR spectroscopy provides evidences that the protein undergoes a slow structural change upon binding iron and that the protein interacts with iron in two ways, the first stoichiometric and high affinity (K_d=10^{-16} M) and the second low affinity (K_d =5.5 ± 4.0 μM), high capacity (~20 Fe^{3+}/Mms6) and cooperative with respect to iron. We propose that the structural basis of formation of magnetic particles by Mms6 is the C-terminal-driven formation of a platform of iron-binding C-terminal domains on the membrane of the magnetosome or on a micellar surface that concentrate iron and nucleate the formation of crystal seeds.

Experimental Procedures

Materials- The mature form of Mms6 was expressed with a poly-histidine tag extending from the N-terminus with an enterokinase cleavage site located between the tag and Mms6 (referred to here as His-Mms6) and purified as described previously (11). The C-terminal domain of Mms6 (C21Mms6: KSRDIESAQSDEE VELRDALA) was synthesized by Genscript (Genscript Corp., www. genscript.com), provided as a solution in water, and used as received. The concentration of C21Mms6 was determined fluorescently by OPA with C25Mms6

(YAYMKSRDIESAQSDEEVELRDALA) as standard (The concentration of C25Mms6 was determined by A280 using extinction coefficient of 2980 M^{-1} cm^{-1}).

His-Mms6 mutants- Expression vectors for His-m2Mms6 and His-m3Mms6 were prepared using annealed complementary oligonucleotides encoding the appropriate mutant sequence to replace the previously cloned wild-type sequence (11). The proteins were expressed and purified as for His-Mms6 (11). The sequences of the 21 C-terminal part of His-m2Mms6 and His-m3Mms6 are KDR**S**I**DE**AQ**ESDS**VEL R**E**ALA and QSLERAEDEDADISAVEKLSR respectively compared with the sequence of the His-Mms6 C-terminal domain (KSRDIESAQSDEEVELRDALA). For the m2 mutant the instances of amino acid replacement are bolded and also underlined when a -OH and -COOH side chain have been interchanged. The sequences of all other parts of these three proteins are the same. CLC protein workbench software (CLC bio) was used to identify the sequences for His-m2Mms6 and His-m3Mms6 that possessed similar hydropathy plots to that of Mms6.

Analytical ultracentrifugation- One half mL of 0.46 mg/mL (A280=0.702) His-Mms6 in 137 mM NaCl, 2.7 mM KCl, 4.3 mM Na_2HPO_4,1.4 mM KH_2PO_4, pH 7.2 was loaded into the cell and placed in an AN60 rotor in a Beckman Proteome Lab XL-A Protein Characterization System (Beckman) for centrifugation. The time-dependent sedimentation of His-Mms6 was monitored at 280 nm, 65,520 x *g*, 4 ℃ for 2 h. The profile of sedimentation coefficient of His-Mms6 was generated by the method of van Holde and Weichet using Ultrascan 8.0 for Windows system

(13-15). The v-bar (0.72) calculated by Ultrascan 8.0 from a weight average of the partial specific volumes of the component amino acid residues of His-Mms6 were used in the analysis. The apparent molecular mass was estimated by the calculator provided in Ultrascan 8.0 using the sedimentation coefficients observed assuming His-Mms6 protein is globular.

Size exclusion chromatography- Chromatography was performed in an AKTA FPLC system (GE healthcare) through prepacked Superose 12 10/300GL (separation range: 1 kDa to 300 kDa) and Superdex Peptide 10/300GL (separation range: 700 Da to 20 kDa) columns at 4 ℃. Flow rates were 0.4-0.5 mL/min. All column samples were prepared by centrifugation at 14,000 *g* at 4 ℃ for 1 h before loading onto the columns. Blue dextran was used to determine the void column volume (V_o) of each column. The elution volumes (V_e) of cytochrome c (MM 10.37 kDa, aprotinin (MM 6.5 kDa), insulin B chain oxidized form (MM 3495 Da) and B12 (MM 1355 Da) (all from Sigma) from a Superdex Peptide 10/300GL column were used to generate the standard curve for the apparent molecular mass estimations of C21Mms6. The C21Mms6 was identified using o-phtalaldehyde (16) (OPA, Thermo Scientific) by adding 200 μL of OPA to 20 μL of column fraction and measuring fluorescence (Ex: 350 nm, Em: 450 nm).

Liposome preparation- 1-palmitoyl-2-oleoyl-*sn*-glycero-3-phosphocholine (POPC) and 1,2-dioleoyl-*sn*-glycero-3-phospho-L-serine (DOPS) in chloroform at a molar ratio of 85:15, were dried by vacuum and resuspended in 20 mM Tris-HCl, 100 mM

KCl, pH 7.5. Liposomes were prepared by extrusion through polycarbonate filters (all reagents from Avanti Polar Lipids) (17).

Proteolytic digestion- Two conditions were used for proteolytic digestion of His-Mms6. In the first case, 1 mg/mL His-Mms6 was digested with 0.1 mg/mL proteinase K (Sigma) in 20 mM Tris-HCl, 100 mM KCl, pH 7.5 and incubated at 25℃ for up to 24 h. In the second case, 1 mg/mL His-Mms6 was first incubated with 10 mM (total lipid concentration) liposome in 20 mM Tris-HCl, 100 mM KCl, pH 7.5 with and without 0.5 % Triton X-100 and incubated at 25 ℃ or 4 ℃ for 1 h with constant mixing by inversion. Samples that included 0.5 % Triton X-100 were then dialyzed against 20 mM Tris-HCl, 100 mM KCl, pH 7.5 with three changes in the presence of Bio-Beads SM-2 detergent adsorbent beads (Bio-Rad) to remove the Triton X-100 (17). His-Mms6 (0.8 mg/mL) with liposomes was digested with 0.2 mg/mL proteinase K in 20 mM Tris-HCl, 100 mM KCl, pH 7.5 at 25℃ for up to 24 h. All reactions were stopped with 9 mM phenylmethylsulfonyl fluoride (Sigma) then 95 ℃ for 5 min. The samples were then resolved by polyacrylamide gel electrophoresis (PAGE) through a 15 % gel in the presence of 0.1 % SDS.

Fluorescence spectroscopy- The tryptophan fluorescence of His-Mms6 was measured in either 96-well plates or in a quartz cuvette at 25 ℃ with a fluorescence spectrophotometer (Varian, Model: Cary Eclipse), at excitation and emission wavelengths of 290 nm and 345 nm respectively. The quenching of His-Mms6 tryptophan fluorescence in the presence of different concentrations of ferric citrate

was used to calculate the fraction of binding sites occupied, B: $B= (F_b-F)/(F_b-F_f)$ where F is the fluorescence signal at a given concentration of iron and F_b and F_f are the signals when the binding sites are fully unoccupied and occupied respectively.(18) In this assay, His-Mms6 (5 μM) was incubated with ferric-citrate (Sigma) at concentrations ranging from 0 to 100 μM in 20 mM Tris-HCl, 100 mM KCl, pH 7.5 in separate brown test tubes for 2 h at 25 ℃ before the fluorescence measurements were taken.

For the studies of the time dependent fluorescence change of His-Mms6 upon free ferric ion addition, 5 μM His-Mms6 or His-m2Mms6 in 50 mM sodium formate, 100 mM KCl, pH 3 were mixed with or without $FeCl_3$ at molar ratios of protein:$FeCl_3$ from 1:2 to 1:6 (inclusive of all unit values) and monitored every 15 min (Ex: 290 nm, Em: 340 nm) at 25 ℃ with a fluorescence spectrophotometer (Varian, Cary Eclipse).

$^{55}Fe^{3+}$ binding assays- In measuring the affinity of His-Mms6 for iron by the filter assay (19), the concentration of His-Mms6 was 100 nM or 1 μM throughout. The solution contained 100 mM KCl and the pH was either pH 3 (adjusted with HCl) or pH 7.5 for all studies with ferric-citrate (established with 20 mM Tris-HCl). Under these conditions, His-Mms6 was incubated with ^{55}Fe (PerkinElmer) in the form of ferric chloride or ferric citrate at various concentrations of iron as indicated for individual experiments in the legends to figures. Unless otherwise noted, the incubations were two hours at 4 ℃ or 25 ℃. The incubations with ferric citrate

were done in brown test tubes to prevent possible auto-reduction of ferric citrate (20). The incubated samples were filtered through 0.45 μm nitrocellulose membranes (Millipore) that had been prewashed with the same buffer solution and at the same temperature as during the incubation. The membranes were washed with two consecutive 5 mL volumes of buffer at the same temperature as during the incubation then removed and the captured radioactivity was counted using Scintiverse BD LSC Cocktail scintillation solution (Fisher Scientific) and liquid scintillation analyzer (Packard model 1600 TR). The highest background observed with this method was less than 1% of the maximum bound values. The retention efficiency of His-Mms6 hold by the filter with this method was about 90% (Supplementary Table 1)

Scatchard plots were used to calculate the K_d of His-Mms6 for iron in all binding assays (21). The equation used is: $B/F=B_{max}/K_d-B/K_d$, where B is the amount of iron bound by His-Mms6, F is the free, unbound iron concentration in solution and B_{max} is the maximum amount of iron bound by His-Mms6. By plotting B/F versus B, the B_{max} and K_d can be calculated from the Y and X-axis intercepts. The stoichiometry between iron and protein was then determined by B_{max}/protein (molar ratio). The absolute K_d of His-Mms6 for ferric iron at pH 7.5 was calculated by the equation $K_d=K_d^{app} \times K_{d\ (ferric\text{-}citrate)}$, where K_d^{app} is the binding constant of His-Mms6 for iron observed at pH 7.5, $K_{d\ (ferric\text{-}citrate)}$ is the dissociate constant of ferric citrate at pH 7.5.

Nuclear magnetic resonance (NMR) spectroscopy- NMR analysis was performed on a Bruker AVII700 equipped with a 5 mm TCI cryoprobe. All NMR analyses were performed at 25 ℃. Each 1H1D spectra was acquired using pre-saturation for solvent suppression (Bruker pulse program zgpr) and consisted of 64 scans with an acquisition time of 3 min. 2D 1H-1H TOCSY and NOESY spectra were collected using standard experimental protocols (Bruker pulse programs mlevgpgp19 and noesygpph19, respectively) with WATERGATE solvent suppression. The TOCSY experiment consisted of 256 time increments of 8 scans each, with a total acquisition time of 43 min and MLEV17 mixing time of 80 ms. The NOESY experiment consisted of 512 time increments of 64 scans each, with a total acquisition time of 7.5h and NOESY mixing time of 400 ms. All NMR data were processed and analyzed using Bruker Topspin 2.1 software.

Dynamic Light Scattering (DLS)- His-Mms6 (0.5 mg/ml) in 100 µL of 137 mM NaCl, 2.7 mM KCl, 4.3 mM Na_2HPO_4, 1.4 mM KH_2PO_4, pH 7.2 at 25 ℃ were analyzed with a Zetasizer Nanoparticle analyzer (Model: ZEN3690, Malvern Instrument Ltd.). Each measurement consisted of 11 acquisitions of 10s with 3 repeats. Data were processed by using Dispersion Technology Software 5.00 (Malvern Instrument Ltd). The buffer was filtered through a 0.45 µm nitrocellulose membrane and the protein samples were centrifuged for 1h (14000 *g*, 4 ℃) prior to use.

Results

High affinity iron binding by Mms6. The affinity of Mms6 for iron has so far only been shown qualitatively (10,11). We determined the binding constant and stoichiometry of iron to Mms6 using ^{55}Fe and ferric citrate ($^{55}FeCl_3$:citric acid = 1:1 (M/M)) to accurately provide adequately low concentrations of $^{55}Fe^{3+}$ to assess high affinity binding at pH 7.5. A Scatchard plot of the results yielded a K_d^{app} of 30 μM for ferric citrate bound to His-Mms6 protein with a 1:1 stoichiometry (Fig. 1A.●). After taking into consideration the K_d ($10^{-11.5}$ M) of ferric citrate for Fe^{3+} (22,23) the K_d of His-Mms6 for iron was calculated to be 10^{-16} M.

The amino acid side chains that could chelate iron are located in the C-terminal domain. To examine if the C-terminal sequence of Mms6 is responsible for this high affinity iron binding, we tested two mutant forms of His-Mms6. The first mutant (His-m2Mms6) had the same sequence as His-Mms6 through to the final 21 amino acids, in which the residues containing –OH and –COOH groups, that are expected to be involved in chelating the Fe^{3+}, were shuffled. The second mutant (His-m3Mms6) also had the same sequence as His-Mms6 up to the last 21 amino acid residues, which were scrambled. Neither His-m2Mms6 nor His-m3Mms6 showed high affinity binding of Fe^{3+} (Fig. 1A, □, ▲). The estimated K_d of His-m2Mms6 was 52 μM (The number of Fe^{3+} bound per His-m2Mms6 at saturation was 0.2). The estimated K_d of His-m3Mms6 was 9.8 μM (The number of Fe^{3+} bound

per His-m2Mms6 at saturation was 0.1). The fitting of the scatchard plot was poor in both case (R^2=0.54 and 0.66 respectively).

The C-terminal segment of Mms6 alone was also tested for iron binding. The initial trial of test of the C-terminal for iron binding by filter assay was not successful because the C-terminal peptide (C21Mms6) is not sufficiently hydrophobic to be adsorbed by the nitrocellulose membrane filters and too small to be retained by the 0.45 μm diameter pores of the filters. The iron binding activity of C21Mms6 was qualitatively examined by size exclusion chromatography at pH7.5 using ferric citrate (Fig. 1B). The C21Mms6-bound and unbound Fe^{3+} were separated by size exclusion chromatography (Fig. 1B). The Fe^{3+}-bound C21Mms6 fraction was quantified fluorescently by OPA with C25Mms6 (YAYMKSRDIESA QSDEEVELRDALA) as standard (its concentration was determined by A280 using extinction coefficient of 2980 M^{-1} cm^{-1}). Using the ferrozine assay to determine the concentration of iron bound by C21Mms6, the binding of Fe^{3+} by C21Mms6 was found to be stoichiometric. Although this method does not provide an affinity constant of the C-terminal segment of Mms6 for Fe^{3+}, the fact that C21Mms6 binds Fe^{3+} stoichiometrically in the presence of excess citrate indicates that it has a higher affinity than citrate for Fe^{3+}, which is $10^{-11.5}$ M These results, combined with previous observations that the C-terminal segment of Mms6 can promote the formation of magnetic particles (24,25), identifies the C-terminal domain of Mms6 as responsible for high affinity stoichiometric iron binding.

Two distinct phases of iron binding by Mms6. Due to the necessity of maintaining equilibration between Fe^{3+} and citrate, the previously described studies were performed at pH 7.5 at which pH the affinity of citrate for Fe^{3+} is high ($10^{-11.5}$ M). However, nanoparticle formation by His-Mms6 *in vitro* is achieved at high iron concentrations (mM) that cannot be achieved at neutral pH due to the insolubility of hydrated Fe^{3+} for which the equilibrium concentration cannot exceed 10^{-17} M at pH 7 (26). Therefore, the concentration dependence of Fe^{3+} binding to His-Mms6 was also determined at pH 3 (Fig. 2). Again evidence of stoichiometric, high affinity Fe^{3+} binding was observed (Fig. 2,●). However, with increasing concentrations of iron, a second phase of iron binding to His-Mms6 was discovered with an apparent low affinity and a stoichiometry much higher than 1:1 (Fig. 2,●). Scatchard plots revealed two phase of binding (Fig. 2 lower right Inset). The first high affinity phase revealed stoichiometric (Fe^{3+}:His-Mms6=1:1). Although a high apparent affinity (K_d^{app} = 0.44 ± 0.06 μM) was measured, this value cannot be accurately determined in this context due to the high ratio of protein to Fe^{3+}. The second binding phase has a much lower apparent affinity (K_d^{app} = 5.5 ± 4.0 μM) of iron with His-Mms6 and a stoichiometry of about 19:1 (19 ± 8). To test whether the high stoichiometry binding of iron for His-Mms6 was due to iron precipitation, His-m2Mms6 (shuffled C-terminal –OH and –COOH groups) and His-m3Mms6 (scrambled C-terminal amino acid sequence) were incubated with iron under the same conditions as for His-Mms6 (Fig. 2, ■, ◊). Neither showed evidence of either

phase of iron binding observed with His-Mms6. A Hill plot revealed cooperativity of the second binding phase of Fe^{3+} binding to His-Mms6 (Hill n value ~3, Fig. 2 upper left Inset). As a control for nonspecific binding, His-m2Mms6 (shuffled C-terminal –OH and –COOH groups) and His-m3Mms6 (scrambled C-terminal amino acid sequence) were incubated with iron under the same conditions as for His-Mms6 (Fig. 2, ■, ◊). Nonspecific iron binding did not become apparent until the iron concentration was about 3 μM (Fig. 2, ◊).

The low affinity high capacity binding of iron by Mms6 cannot be readily explained by the number of potential chelating residues in the C-terminal domain this protein (7 -COOH and 3 -OH), particularly as the first high affinity binding likely involves more that one of these residues. To resolve this inconsistency, we postulated that the initial stoichiometric binding of iron might result in a structural change in Mms6 to promote their interactions to form a larger complex that promotes iron clustering. This explanation is also consistent with the observed cooperativity of Fe^{3+} binding with respect to iron concentration. Based on results reported in the next section that are consistent with Mms6 forming a micellar quaternary structure, we also speculated that the structural change might involve the N-terminal segment in strong hydrophobic and van der waals interactions and might be prevented or slow down at lower temperatures. Therefore, we determined the binding curve of His-Mms6 as a function of Fe^{3+} concentration at 4℃ with and without incubation for 2h at 4℃ before capturing on the filters. Under these

conditions, His-Mms6 only demonstrated high affinity stoichiometric binding (K_d^{app} = 1.1 ± 0. 3 μM, Fig. 2, O, ▲) and no high capacity binding was observed.

His-Mms6 exists in aqueous solution as large micelles. The high capacity iron binding and almost equal length of the hydrophobic N-terminal domain and hydrophilic C-terminal domain suggested that Mms6 might form micelles or larger quaternary structures. To investigate this hypothesis, the apparent molecular mass of His-Mms6 was investigated by size exclusion chromatography (Fig. 3A), analytical ultracentrifugation (Fig. 3B) and DLS (Fig. 3C). These studies showed that His-Mms6 exists in large complexes. The monomeric molecular mass of His-Mms6 is 10.2 kDa. But, the peak of His-Mms6 eluted through a Superose 12 column (separation range: 1 kDa to 300 kDa) in the void volume as identified by blue dextran, which suggests an apparent molecular mass equal of or greater than 300 kDa (Fig. 3A). Assuming that His-Mms6 is a globular protein, we expected a sedimentation coefficient of 1.16S for monomeric His-Mms6. The observed sedimentation coefficients, distributed from 20 to 100S with the majority between 20 and 40S, also indicate that His-Mms6 forms large multimers with an estimated apparent molecular mass between 200 kDa and 400 kDa (Fig. 3B and Supplementary Fig. 4). Dynamic light scattering showed two particles sizes between which the protein mass is almost equally distributed (Fig. 3C). Peak 1 was 59% of the mass and particles with a mean radius of 5.1 ± 1.5 nm and an estimated molecular mass of ~200 kDa (Fig. 3C). Peak 2 contained 41% of the protein mass

and particles with a mean radius of 12 ± 6.5 nm and an estimated molecular mass of ~2000 kDa (Fig. 3C). Although these latter particles contained a significant portion of the mass, they only represent 6% of all particles. Thus, the results of size exclusion chromatography, analytical ultracentrifugation and DLS studies show that His-Mms6 forms large multimers with most of the particles containing 20-40 protein molecules.

To test the hypothesis that the quaternary structure of His-Mms6 is a micelle with the N-terminal domain inside and the C-terminal domain outside, we first examined if the C-terminal domain is external and accessible for proteolytic cleavage (Fig. 3D). Digestion of His-Mms6 with proteinase K resulted in a significant decrease in its monomeric size within 5 min (Fig. 3D, middle panel). This rate of loss of His-Mms6 molecular mass was similar to the rate of degradation of C21Mms6 incubated under the same conditions (Fig. 3D, bottom panel). A protease-resistant fragment of His-Mms6 remained even after 24 h digestion (Fig. 3D, middle panel) whereas, like C21Mms6, BSA was digested almost completely by this time (Fig. 3D, top panel). The proteinase K-resistant portion of His-Mms6 was not soluble in aqueous buffer (no detergent was present in the buffer) and was found as a precipitate, which is consistent with the presence of a hydrophobic resistant core. N-terminal sequencing results also confirmed that the precipitate consisted mainly of hydrophobic and aromatic amino acids (Supplementary Table 2). At higher

concentrations of proteinase K the N-terminal domain was also degraded (Fig. 3E, last lane)

Although it has some characteristics of a membrane protein, His-Mms6 does not require detergent for its solubility in aqueous solution. If it forms a micellar quaternary structure, these micelles should also fuse directly with liposomes without the aid of a detergent. His-Mms6 was mixed with liposomes in the presence or absence of Triton X-100 and at either 4℃ or 25 ℃ (Fig. 3E). To determine if the protein had been incorporated into the liposomes, the mixture was incubated with a high concentration of proteinase K (His-Mms6 : proteinase K=4 : 1) that completely degraded His-Mms6 alone (Fig. 3E, last lane). A proteinase K-resistant fragment was observed when His-Mms6 was incubated with liposomes in the presence or absence of Triton X-100 (Fig. 3E, lanes 2 and 4). This proteinase K resistant fragment is larger than that produced when Mms6 is incubated with proteinase K in the absence of liposome at higher His-Mms6/proteinase K ratio (10:1) (Fig. 3E, lanes 5), which is consistent with the expectation that, when buried in the liposome, more of the Mms6 N-terminal domain might be protected from proteolysis than in the absence of liposome membrane such as in Fig. 3D and Fig. 3E, lane 5. Thus, as expected of a micelle, detergent is not required for His-Mms6 to incorporate into liposomes. The inclusion of Triton X-100 during membrane insertion also resulted in a portion of full-length His-Mms6 being completely proteinase resistant (Fig. 3E, lanes 2). This could be due to the inclusion of some of the His-Mms6 either inside

the liposomes or incorporated into the membrane with the C-terminus in the liposome lumen rather than on the outside where it is susceptible to the proteolytic action of proteinase K. Decreasing the incubation temperature below the liquid to solid phase transition temperature of the liposomes resulted in less protection of His-Mms6 from proteinase K (Fig. 3E, lane 3), which is also consistent with the protein incorporating into the liposomes in the absence of detergent. In the absence of liposomes, a low ratio (4:1) of His-Mms6 to proteinase K resulted in complete degradation of His-Mms6, which did not occur at the higher His-Mms6/proteinase K ratio used for the remaining conditions in experiment described in Figure 3D and E.

In summary, we have found that His-Mms6 1) exists in large particles in aqueous solution and in the absence of detergent and its 2) C-terminal domain can readily be cleaved leaving a protease-resistant core, 3) can fuse in a temperature-dependent manner with liposomes, and 4) form monolayer on an aqueous surface in a Langmuir trough (Supplementary Fig 1). In their entirety, these results provide strong evidence that His-Mms6 forms a micellar quaternary structure.

The C-terminal domain of Mms6 adopts a defined conformation. Many short peptides are inherently disordered. But, the Mms6 C-terminal domain alone can direct the formation of magnetic nanoparticles *in vitro* when linked to polymer (21). If the mechanism of nanoparticles formation by Mms6 involves the C-terminal domain binding iron at high stoichiometry then C21Mms6 might be capable of forming a defined structure. We used 2D 1H-1H TOCSY and NOESY spectra to

investigate the structure of C21Mms6 (Fig. 4A). The TOCSY (total correlation spectroscopy) transfers magnetization through the chemical bonds between adjacent protons within the same spin system. The NOESY (total correlation spectroscopy) transfers magnetization between protons that are close in space (< 5Å) and the intensity of the cross peaks are proportional to $1/r^{-6}$. So, by overlay the TOCSY and NOESY spectra, we can identified those protons which are not in the same spin system while spatially close which can be used as an indication of the existence of a structured molecule. We found that the NOESY spectrum of C21Mms6 included numerous non-sequential, inter-residue amide to side-chain NOE cross peaks and, most notably, six amide to amide cross peaks. These cross peaks indicate that C21Mms6 has a stable conformation in solution (Fig. 4A). The detailed assignments of the NMR spectra and the modeling of the structure of C21Mms6 are ongoing

To determine if interactions between C-termini might contribute to the micellar structure, we also investigated the hypothesis that C21Mms6 forms multimers. The monomeric form of C21Mms6 has a molecular mass of 2.36 kDa. The apparent molecular mass of C21Mms6 in 100mM KCl at pH7.5 and pH3 was estimated to be 4.6 and 5.3 kDa respectively (Fig. 4B). The results of analysis by size exclusion chromatography showed that C21Mms6 exhibited dimeric apparent molecular mass in 100 mM KCl at both pH 7.5 and pH 3 (Fig. 4B). In the presence of 6M guanidinium HCl, C21Mms6 runs as a monomer (Supplement Fig. 2).

Mms6 conformation changes on iron binding. The biphasic iron binding of His-Mms6 combined with its multimeric quaternary structure suggested that the protein itself might change in conformation on binding iron. To examine the effect of iron on His-Mms6 structure, we took advantage of the presence of two trp residues in the N-terminal domain (W5 and W21), and looked for an effect of iron binding on trp fluorescence. His-Mms6 was incubated with a range of concentrations of ferric-citrate at pH7.5 for 2h and the fluorescence was monitored (Fig. 5A). From this study the K_d^{app} of His-Mms6 was determined to be 22 ± 8.6 µM by Scatchard plot (Fig. 5 B) and thus the K_d to be 6×10^{-17} M, which matches well the K_d determined using the ^{55}Fe filter binding assay (Fig. 1A). Similar fluorescence quenching was not observed for His-m3Mms6 (Supplementary Fig.5▲) which did not bind ferric citrate when measured with filter binding assay (Fig. 1▲). This result indicates that the fluorescence quenching was resulted from the binding of ferric iron at the C-terminal domain of Mms6 protein.

Mms6 undergoes a slow structural change after the addition of iron. The change in Mms6 structure, as reflected by the trp fluorescence quenching, was surprisingly slow and occurred over a period of hours (Fig. 5C, ●). The slow kinetics is also supported by a similarly timed change in line broadening in the ^{1}H-NMR proton spectra, which again sharpen after 4 h and before 24 h (Fig. 5D). A similar change in fluorescence quenching was not observed with His-m2Mms6 (Fig. 5C, ■).

Discussion

To understand how a protein, such as Mms6, promotes the alignment of iron atoms to form a crystal, it is important to know the structure of this protein and how it might respond to the presence of iron. With Mms6 being a very small protein (59 amino acids), it seemed likely that the relevant functional form of this protein involves a larger multimeric assembly. The N-terminal domain of Mms6 contains a Leu-Gly rich region, which is similar to some self-aggregating proteins of other bio-mineralization systems (7,27-29), and is consistent with the possibility that His-Mms6 similarly forms a larger structure. We examined the quaternary structure of His-Mms6 and found that the N-terminal domain self-assembles into relatively uniform micelles of 20-40 units with the C-terminal domain on the surface. Although, it would be desirable to solve the structure of full length Mms6 by X-ray cryptography or NMR spectroscopy, we have not yet been able to obtain a homogenous Mms6 monomer. No homogenous monomeric form of His-Mms6 was obtained in either 4 M urea or 6 M GnCl (Supplementary Fig 6). Therefore, we have used other biophysical and biochemical analyses to understand the structure of this unusual protein such as fluorescence spectroscopy, size exclusion chromatography, dynamic light scattering, analytical ultracentrifugation, and filter binding assay.

When linked to Pluronic® F127, a block copolymer, both C21- and C25Mms6 are able to promote magnetite nanoparticle formation *in vitro* similarly to the full

length protein (unpublished and 25). Here we show that C21Mms6 binds Fe^{3+} tightly and that His-Mms6 binds one Fe^{3+} with a very high affinity ($K_d = 10^{-16}$ M) that is close to the affinity of transferrin for Fe^{3+} ($K_d = 10^{-18}$ M) (30). However, 10^{-16} M is well below the concentration of iron expected to be present in the magnetosome during crystal formation and is also well below the mM concentration of Fe^{3+}/Fe^{2+} present during *in vitro* synthesis. To achieve these higher iron concentrations we measured His-Mms6 binding to iron at pH 3 and observed two binding phases with respect to iron concentration: a high affinity phase ($K_d^{app} = 0.44 \pm 0.06$ μM) and a second low affinity phase ($K_d^{app} = 5.5 \pm 4.0$ μM). Both iron-binding phases are likely to be relevant to iron crystal formation. We speculate that the first high affinity phase alters the C-terminal conformation, which results in a structural change in a multimeric protein complex that enables the second low affinity iron binding phase in which iron clusters on the protein cooperatively and at high stoichiometry.

In these studies, we have used a recombinant form of Mms6 that includes a histidine tag (His-Mms6). Although it would be desirable to obtain the protein without the histidine tag, we have not yet found a reliable means of achieving this goal. The optimization of the enzymatic cleavage conditions (incubation time, metal ion) used to remove the His-tag of His-Mms6 by enterokinase resulted in the nonspecific cleavage at the C-terminus of Mms6 with the His-tag uncleaved (31). The inclusion of detergents or urea also did not promote cleavage of the His-tag

(Supplementary Fig.7). His-Mms6 has the same activity as originally described for Mms6 (10) in that it promotes the formation of magnetic magnetite nanoparticles of a size and shape similar to the biologically formed crystals in magnetosomes as we previous characterized using magnetic property measurement, TEM and powder X-ray diffraction analysis (11). The mutant proteins, His-m2Mms6 and His-m3Mms6, were controls for actions, if any, of the His tag. In addition, studies with the C-terminal peptide (C21Mms6), which has no His tag, confirmed or supplemented results obtained with the full-length protein.

The low affinity iron-binding activity of His-Mms6 is cooperative with respect to iron concentration (Hill n value ~3) and involves a massively high stoichiometry of iron/His-Mms6 (~19/1). The observed cooperativity suggests that the protein is organizing the iron on its surface in such a way that the presence of some iron atoms on the surface promotes the incorporation of other iron atoms. This might reflect the beginning of crystal packing. The high stoichiometry of iron/His-Mms6 that is achieved in the low affinity phase of iron binding is difficult to explain based on the number of potential chelating residues in the His-Mms6 sequence.

The results reported here provide the basis for a model of a mechanism by which Mms6 promotes iron crystallization *in vitro* (Fig. 6). In this model, it is proposed that the high affinity and stoichiometric binding of iron by the C-terminal domain of Mms6 changes the monomer structure causing a change in quaternary structure of

the micellar protein complex that allows the cooperative binding of iron at high stoichiometry. *In vivo* a similar mechanism might operate on the membrane.

References

1. Blakemore, R. (1975) *Science* **190**, 377-379
2. Balkwill, D. L., Maratea, D., and Blakemore, R. P. (1980) *J. Bacteriol.* **141**, 1399-1408
3. Ofer, S., Nowik, I., Bauminger, E. R., Papaefthymiou, G. C., Frankel, R. B., and Blakemore, R. P. (1984) *Biophys. J.* **46**, 57-64
4. Gorby, Y. A., Beveridge, T. J., and Blakemore, R. P. (1988) *Journal of Bacteriology* **170**, 834-841
5. Bazylinski, D. A., and Frankel, R. B. (2004) *Nature Reviews Microbiology* **2**, 217-230
6. Frankel, R. B., and Bazylinski, D. A. (2006) *Trends in Microbiology* **14**, 329-331
7. Komeili, A. (2007) *Annual Review of Biochemistry* **76**, 351-366
8. Frankel, R. B., Bazylinski, D. A., Johnson, M. S., and Taylor, B. L. (1997) *Biophys. J.* **73**, 994-1000
9. Matsunaga, T., Okamura, Y., Fukuda, Y., Wahyudi, A. T., Murase, Y., and Takeyama, H. (2005) *DNA Res* **12**, 157-166
10. Arakaki, A., Webb, J., and Matsunaga, T. (2003) *J. Biol. Chem.* **278**, 8745-8750
11. Prozorov, T., Mallapragada, S. M., Narasimhan, B., Wang, L., Palo, P., Nilsen-Hamilton, M., Williams, T. J., Bazylinski, D. A., Prozorov, R., and Canfield, P. C. (2007) *Advanced Functional Materials* **17**, 951-957
12. Tanaka, M., Mazuyama, E., Arakaki, A., and Matsunaga, T. (2010) *Journal of Biological Chemistry* **In press**
13. Van Holde, K. E., and Weischet, W. O. (1978) *Biopolymers* **17**, 1387-1403
14. Demeler, B., and van Holde, K. E. (2004) *Analytical Biochemistry* **335**, 279-288
15. Demeler, B. *The University of Texas Health Science Center at San Antonio, Department of Biochemistry.* *http://www.ultrascan.uthscsa.edu*
16. Drescher, D. G., and Lee, K. S. (1978) *Analytical Biochemistry* **84**, 559-569
17. Lu, X., Zhang, Y., and Shin, Y.-K. (2008) *Nat Struct Mol Biol* **15**, 700-706
18. Baldwin, G. S., Curtain, C. C., and Sawyer, W. H. (2001) *Biochemistry* **40**, 10741-10746
19. Leblanc, B., Moss, T., and Stockley, P. G. (2009) Filter-Binding Assays. in *DNA-Protein Interactions*, Humana Press. pp 1-14
20. Francko, D. A., and T.Heath, R. (1982) *Limnology and Oceanography* **27**, 564-569
21. Scatchard, G. (1949) *Annals of the New York Academy of Sciences* **51**, 660-672
22. Musílková, J., Kriegerbecková, K., Krůsek, J., and Kovár, J. (1998) *Biochimica et Biophysica Acta (BBA) - Biomembranes* **1369**, 103-108

23. Kotrly, S., and Sucha, L. (1985) *Handbook of chemical equilibria in analytical chemistry*, Horwood ; Halsted Press, Chichester : New York :
24. Arakaki, A., Masuda, F., Amemiya, Y., Tanaka, T., and Matsunaga, T. (2010) *J Colloid Interface Sci* **343**, 65-70
25. Prozorov, T., Palo, P., Wang, L., Nilsen-Hamilton, M., Jones, D., Orr, D., Mallapragada, S. K., Narasimhan, B., Canfield, P. C., and Prozorov, R. (2007) *ACS Nano* **1**, 228-233
26. Baker, H. M., Anderson, B. F., and Baker, E. N. (2003) *PNAS* **100**, 3579-3583
27. Amemiya, Y., Arakaki, A., Staniland, S. S., Tanaka, T., and Matsunaga, T. (2007) *Biomaterials* **28**, 5381-5389
28. Schüler, D. (2008) *FEMS Microbiology Reviews* **32**, 654-672
29. Faivre, D., and Schüler, D. (2008) *Chemical Reviews* **108**, 4875-4898
30. Lehrer, S. S. (1969) *J. Biol. Chem.* **244**, 3613-3617
31. Wang, L. (2007) Biochemical studies of Mms6---A biomineralization protein (M.S. thesis). in *Biochemistry, Biophysics and Molecular Biology*, Iowa State University, Ames

Figure Legends

Fig. 1. Iron binding characteristics of Mms6. A) Single high affinity binding site of Mms6 for iron. ^{55}Ferric citrate, over the concentration range of 1 to 50 μM was incubated with 1 μM His-Mms6 in 20 mM Tris-HCl, 100 mM KCl, pH 7.5 in brown test tube for 2 h, followed by capture of the bound iron by the filter assay. All data points are the average of duplicate values. The inset shows the Scatchard plot used to calculate the K_d of ferric ion binding to His-Mms6. His-Mms6 (●), His-m2Mms6 (□), His-m3Mms6 (▲). In the Scatchard plot, B/F is the amount of iron bound by His-Mms6 (B) versus free unbound iron concentration (F). B) Iron is bound by the C-terminal domain of Mms6. The elution profile is shown of C21Mms6 with Fe^{3+}-citrate from a Superdex peptide 10/300GL (separation range 700 Da-20 kDa) gel filtration column run at 0.4mL/min (●). Fe^{3+}-citrate was also run through the column in the absence of peptide at 0.4 mL/min (○). The total iron content of each fraction was determined by the ferrozine assay (A562). The molar ratio of iron to C21Mms6 at saturation was determined to be 1. The elution profile of C21Mms6 was established by PAGE of each sample and confirmed to coincide with the elution profile of the identified Fe^{3+}-bound-C21Mms6. Arrow indicates the void volume of the column

Fig. 2. Two phases of iron binding by Mms6. Binding of His-Mms6 to free ferric ion was measured using $^{55}FeCl_3$ with the filter assay at pH 3. The reaction mixtures

contained 100 nM His-Mms6 (●,▲, O), His-m2Mms6 (◊), or His-m3Mms6 (■) in 20mM Tris-HCl, 100mM KCl, pH 3. Incubation was for 2 h at 25 ℃ (●,◊,■) or at 4 ℃ (O) or no preincubation at 4 ℃ (▲) followed by collection and analysis by the filter assay. All data are the average of duplicate values. Error bars represent the standard deviations. **Inset** (**Upper left):** Hill plot of the second phase of iron binding by Mms6. $\theta=Y/(1-Y)$, where Y is the fraction of the occupied sites bound by iron. Y was defined by the equation: $Y=[Fe]^n/(K_d+[Fe]^n)$, n: Hill coefficient, [L]:free iron concentration, K_d: dissociate constant of His-Mms6 for free ferric iron. Because $\log(\theta)=n*\log[Fe]-\log K_d$, the Hill coefficient can be obtained by plotting log (θ) versus log [Fe]. **Inset (Lower right):** Scatchard plot reveals 2 phases of binding.

Fig. 3. His-Mms6 forms micelles. His-Mms6 assembles into large multimers as shown by A) size exclusion chromatogram of His-Mms6 (0.2 mL of 1 mg/mL His-Mms6) from Superose 12 column and B) the sedimentation velocity profile of His-Mms6 and C) Dynamic light scattering. D) His-Mms6 has a proteinase K resistant core. His-Mms6 and C21Mms6 were digested by proteinase K [His-Mms6: proteinase K = 10:1] for the indicated time periods then resolved by SDS-PAGE. The brackets identify the remaining protease-resistant protein fragments. E) His-Mms6: liposome fusion characteristics are consistent with a micellar structure. His-Mms6 was incubated with and without liposomes and then incubated with proteinase K as identified on the figure. Legends above the figure and the added components listed

below the figure identify the conditions in each tube that deviated from the standard conditions, which were 20 mM Tris, 100 mM KCl, pH 7.5, 25 ℃, and His-Mms6: Proteinase K = 4:1. The brackets identify the same protease-resistant fragments as in D. The open arrowheads identify the protease-resistant band formed when the protein is associated with liposomes. Dots represent the positions of different MM markers on the gel (from top to bottom: 25 kDa, 20 kDa, 15 kDa and 10 kDa)

Fig. 4. C21Mms6 is structured. A. NMR spectra. The 1H TOCSY (black) and NOESY (gray) spectra of C21Mms6 (850 μM) were determined in 5% (v/v) D_2O, 100mM KCl, pH 4. 9. The results show distinct peaks in the NOESY spectrum that do not overlap with the TOCSY spectrum (The assignments of spectra and structure modeling are ongoing). B. The dimeric apparent molecular mass of C21Mms6. The elution profile of C21Mms6 in 100 mM KCl, pH7.5 (O) or 50 mM sodium formate, 100 mM KCl, pH 3 (■) from a Superdex peptide 10/300GL column with a flow rate of 0. 4 mL/min at 4 ℃. **Inset:** The standard curve used to estimate the apparent molecular mass of C21Mms6 (standards: ▲, Log (MM): log of the molecular mass of the standards used). The standards used to create this standard curve were: cytochrome C, aprotinin, insulin B chain (oxidized form) and vitamin B12 (Chromatograms are showed in Supplementary Fig. 8). The elution profiles of the insulin B chain (oxidized form) and vitamin B12 were essentially the same under both buffer conditions. Neither cytochrome C nor aprotinin was stable at pH 3.

Fig. 5. Slow change in Mms6 structure with time after adding iron. A) Fluorescence quenching in the N-terminal domain responds to iron binding by His-Mms6. **Inset:** Emission spectrum of 5 μM His-Mms6 in the absence of iron or with 5, 15, 20, 100 μM ferric citrate (the arrow indicates the change in peak height with increasing concentration of ferric citrate). His-Mms6 (5 μM) was incubated with ferric-citrate at concentrations ranging from 0 to 100 μM in 20 mM Tris-HCl, 100 mM KCl, pH 7.5 in separate brown test tubes for 2 h at 25 ℃ before the fluorescence measurements were taken. B) A scatchard analysis of the data in A) that was used to obtain the K_d^{app}. C) Slow change in fluorescence quenching after adding iron. Shown are the averages of the results of five (His-Mms6) or four (His-m2Mms6) independent experiments with the standard deviations in which the values were first normalized to the value of the Fe^{3+}-free sample of each experimental data set. The resulting averages for His-Mms6 (●) and His-m2Mms6 (■) were again normalized to the zero time value for each protein. D) Slow change in the 1H-NMR spectrum after adding iron. C21Mms6 (850 μM) was incubated for the indicated times with 1.7 mM ferric-citrate in 20 mM Tris, 100 mM KCl, 5% D2O (v/v), pH 7.5 followed by measurement of the spectrum by 1H-NMR.

Fig. 6. Model for the mechanism of action of Mms6. Based on the results discussed here, a model is proposed to describe the mechanism by which Mms6 can promote the formation of crystalline nanoparticles. The N-terminus of the protein is seen as tethered in a micelle or a hydrophobic compartment such as a membrane.

The C-termini form minimal quaternary complexes of 2 domains (represented as a dimer of Mms6). Upon binding ferric iron at very high affinity with a molar ratio of 1, the C-termini undergo a conformational change, coordinated with the N-terminal domain that initiates a slow rearrangement of the multiprotein complex to create a surface on which many iron atoms can organize. This slow rearrangement allows the initiation of a crystal that is propagated on the protein surface to form a cluster of iron, which then becomes a crystal seed. Mobility of Mms6 protein islands in the membrane or micelle is proposed to promote fusion of the crystal seeds to grow the magnetic nanoparticles. (Note: The mechanism of oxygen incorporation into the magnetite particles is not considered in this model).

Figure 1

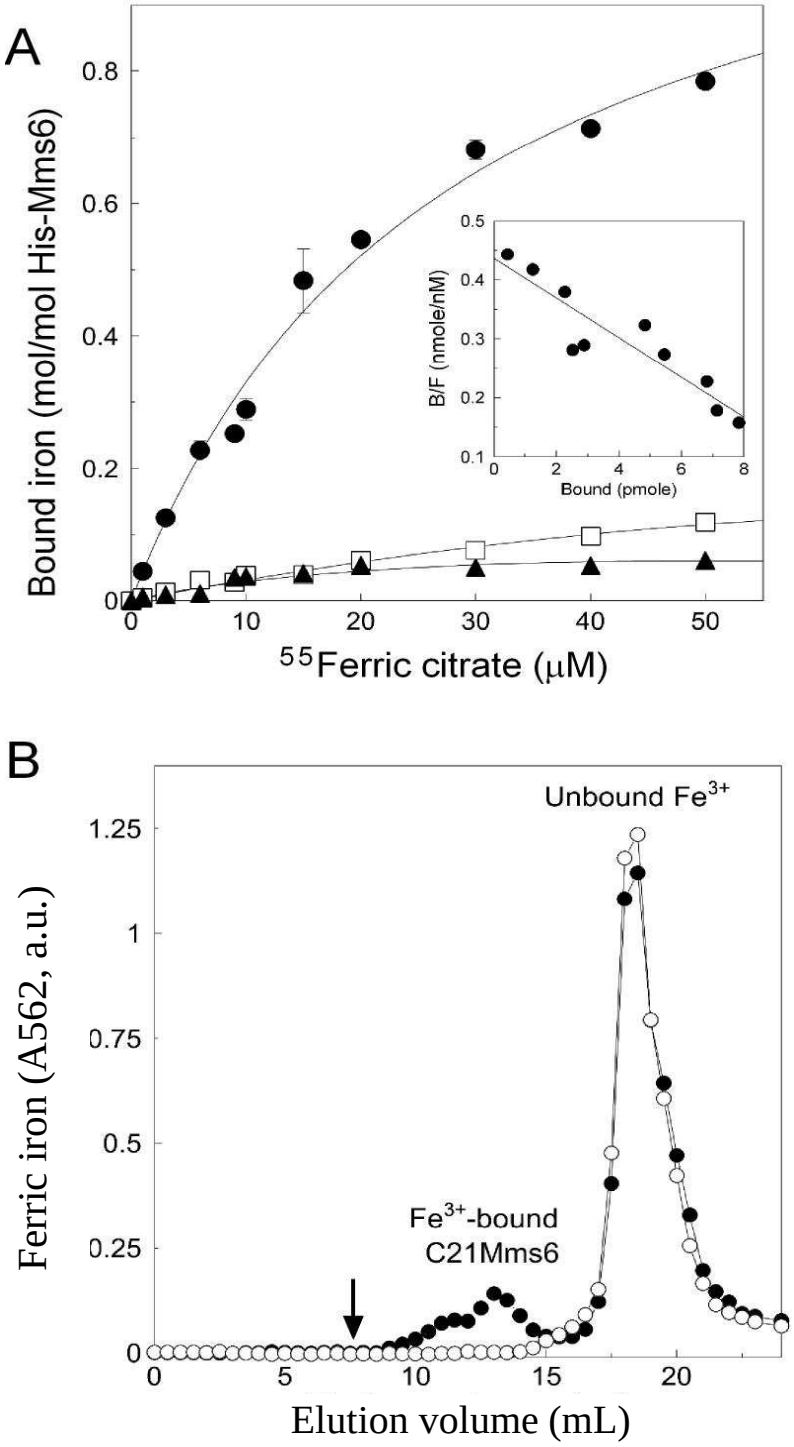
A
Bound iron (mol/mol His-Mms6)
0.8
0.6
0.4
0.2
0
0
10
20
30
40
50
55Ferric citrate (μM)
B/F (nmole/nM)
0.5
0.4
0.3
0.2
0.1
0
2
4
6
8
Bound (pmole)
B
Ferric iron (A562, a.u.)
1.25
1
0.75
0.5
0.25
0
0
5
10
15
20
Elution volume (mL)
Unbound Fe3+
Fe3+-bound
C21Mms6

Figure 2

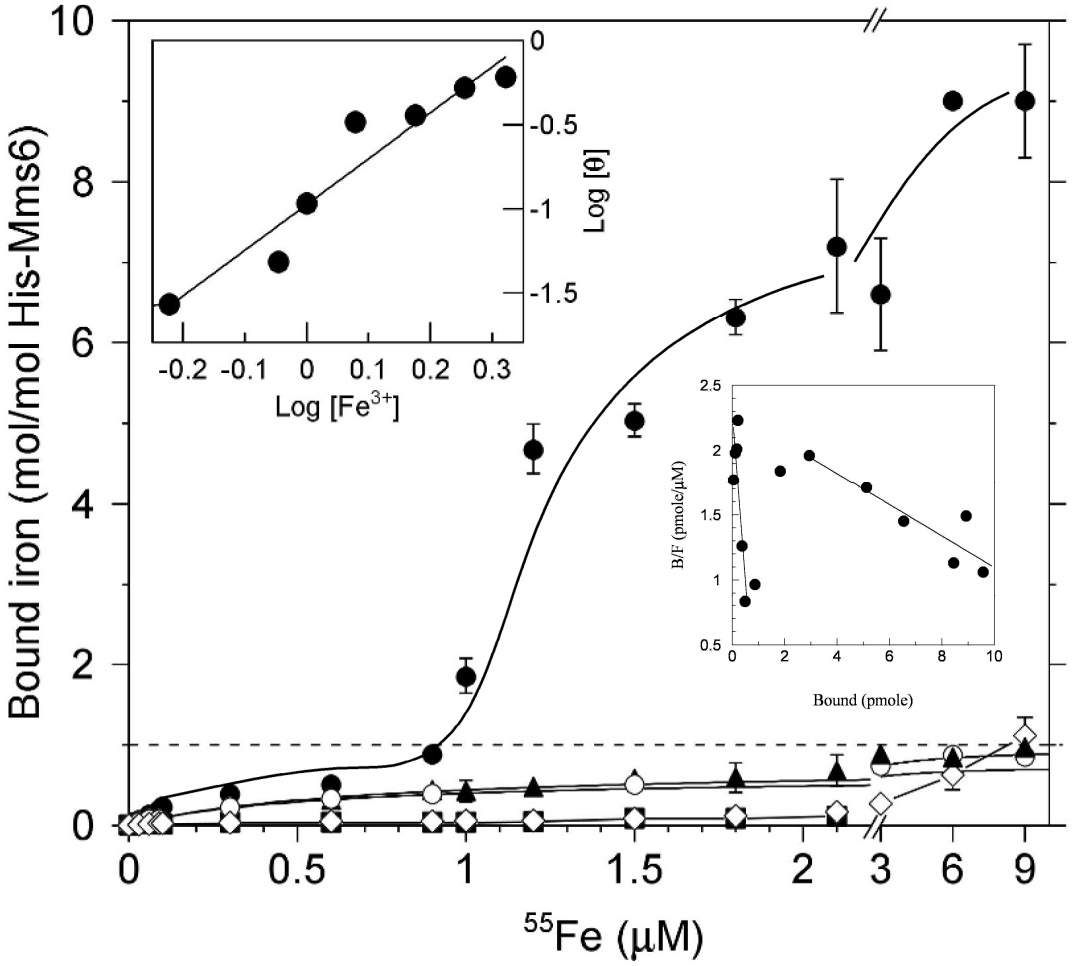
Bound iron (mol/mol His-Mms6)
^{55}Fe (μM)
Log [θ]
Log [Fe^{3+}]
B/F (pmole/μM)
Bound (pmole)

Figure 3

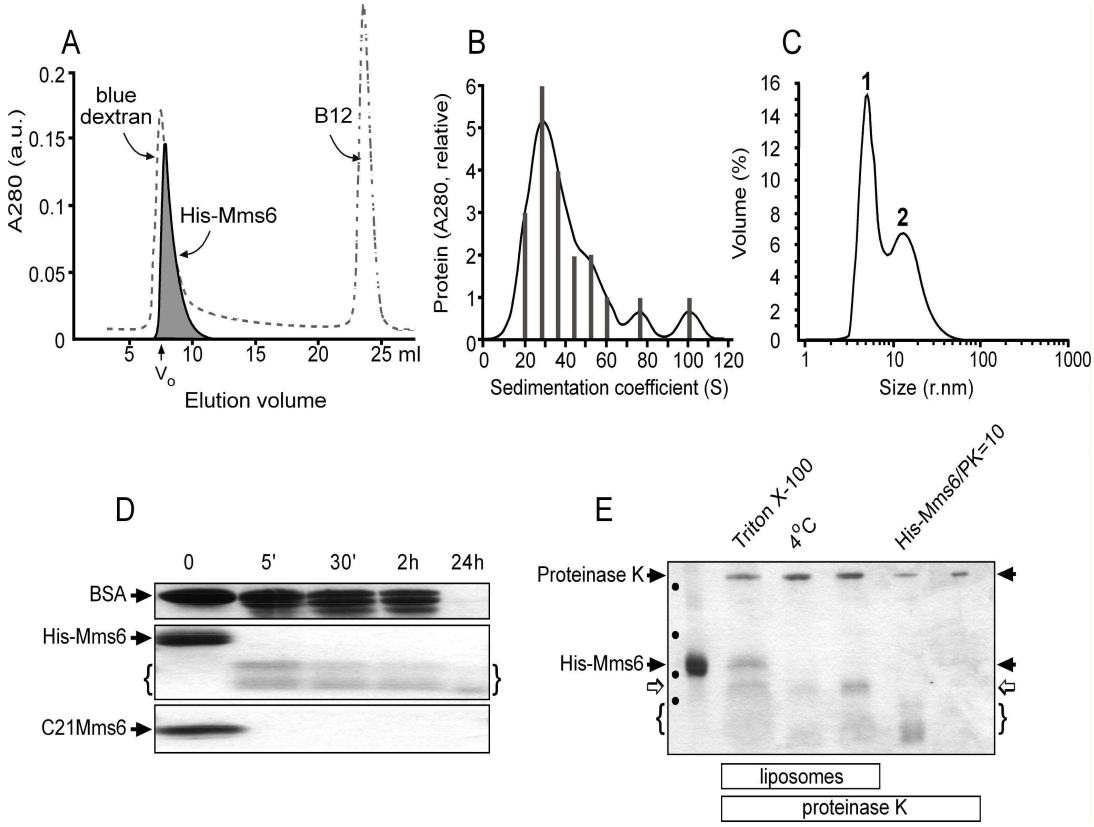
A
blue dextran
B12
His-Mms6
A280 (a.u.)
Elution volume
B
Protein (A280, relative)
Sedimentation coefficient (S)
C
Volume (%)
Size (r.nm)
D
0
5'
30'
2h
24h
BSA
His-Mms6
C21Mms6
E
Triton X-100
4°C
His-Mms6/PK=10
Proteinase K
His-Mms6
liposomes
proteinase K

Figure 4

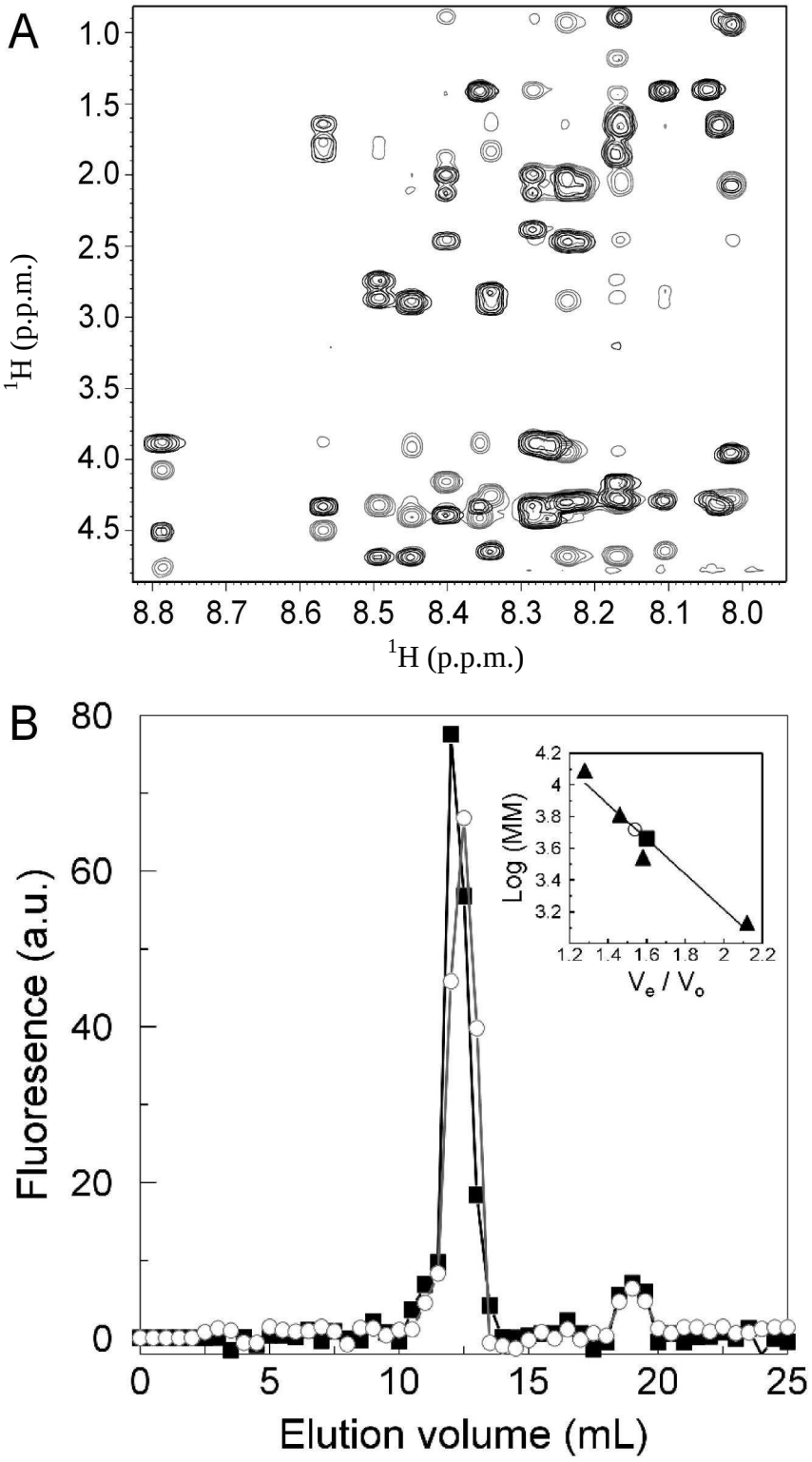
A
1.0
1.5
2.0
2.5
3.0
3.5
4.0
4.5
^{1}H (p.p.m.)
8.8 8.7 8.6 8.5 8.4 8.3 8.2 8.1 8.0
^{1}H (p.p.m.)
B
80
60
40
20
0
Fluoresence (a.u.)
0 5 10 15 20 25
Elution volume (mL)
4.2
4
3.8
3.6
3.4
3.2
Log (MM)
1.2 1.4 1.6 1.8 2 2.2
V_e / V_o

Figure 5

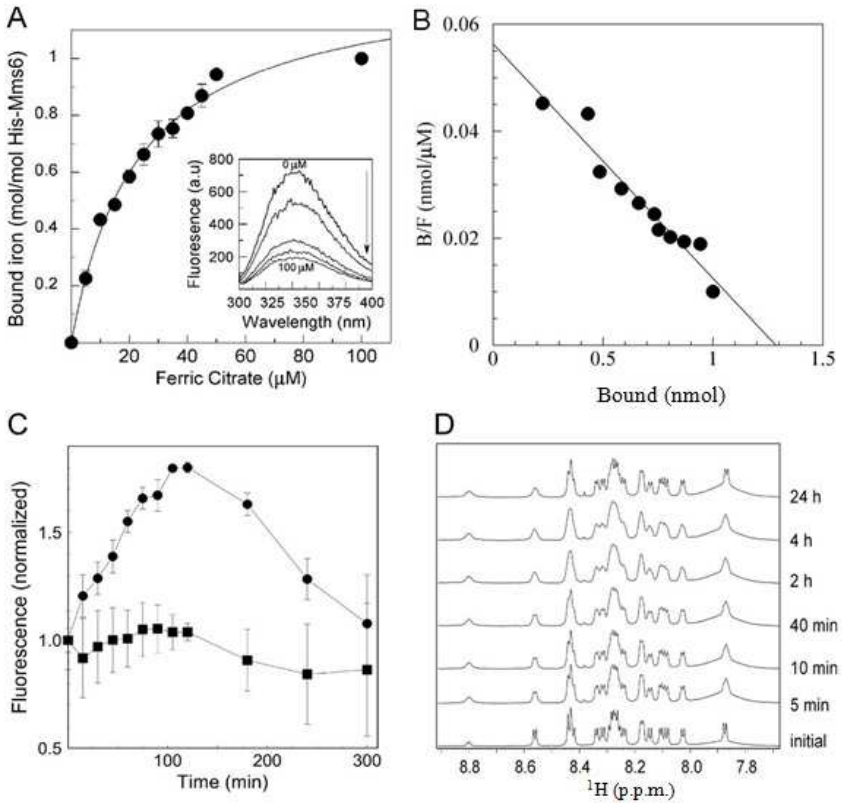
A
Bound iron (mol/mol His-Mms6)
Ferric Citrate (μM)
Fluoresence (a.u)
Wavelength (nm)
0 μM
100 μM
B
B/F (nmol/μM)
Bound (nmol)
C
Fluorescence (normalized)
Time (min)
D
24 h
4 h
2 h
40 min
10 min
5 min
initial
¹H (p.p.m.)

Figure 6

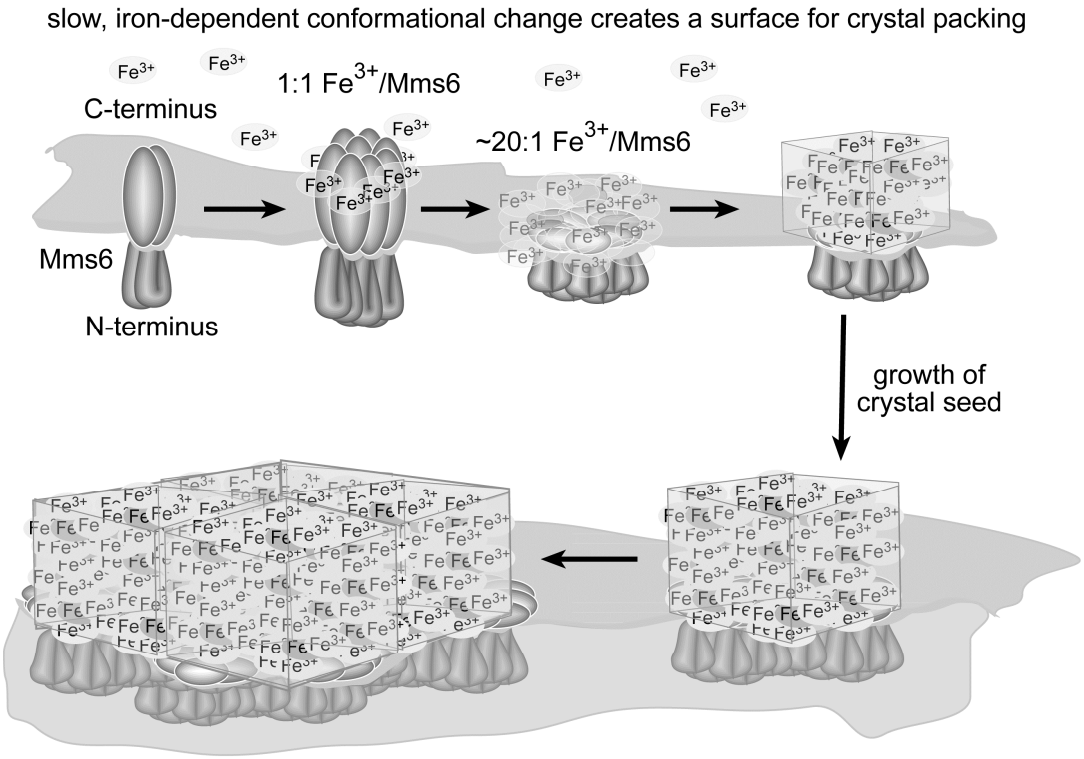
slow, iron-dependent conformational change creates a surface for crystal packing
1:1 Fe3+/Mms6
~20:1 Fe3+/Mms6
C-terminus
Mms6
N-terminus
growth of
crystal seed
mobility of Mms6 islands and fusion of crystal seeds resulting in crystal growth

CHAPTER 3: MAGNETITE BIOMINERALIZATION PROTEIN UNDERGOES AN IRON-DEPENDENT STRUCTURAL CHANGE AND DISPLAYS REDUCTASE ACTIVITY

In preparation for *The Journal of Biological Chemistry*

Lijun Wang[†,¶], Shuren Feng[†,¶], Pierre Palo[†,] D. Bruce Fulton[¶], Tanya Prozorov[£], Xunpei Liu[£], Wenjie Wang[†], David Vaknin[†], Surya Mallapragada[†£] and Marit Nilsen-Hamilton[†,¶,*]

†Ames Laboratory, U. S. Department of Energy, Ames, Iowa 50011, ¶Department of Biochemistry, Biophysics and Molecular Biology, Iowa State University, £Department of Biological and Chemical Engineering, Ames, IA 50011

Address correspondence to: Marit Nilsen-Hamilton, 3206 Molecular Biology Building, Dept of Biochemistry, Biophysics and Molecular Biology, Iowa State University, Ames, IA 50011; Phone: 515-294-9996; Fax: 515-294-0453; Email: marit@iastate. edu

Abstract

Nature uses a bottom-up process to build the hierarchical structures in living organisms. The sizes and morphologies of magnetites formed by magnetotactic bacteria are genetically defined and thus the consequence of the biomineralization protein(s). The mechanism of this process remains elusive. Here, we discussed our studies of Mms6 protein promoted magnetic nanoparticles formation. We

observed that Mms6 undergoes a periodic structural change with increasing iron/protein ratio. The observed structural change occurs in the N-terminal domain, but reflects iron binding by the C-terminal domain. A mutant Mms6 that does not promote the formation of superparamagnetic magnetite also does not undergo the periodic structural change. The correlation between the ability to form magnetic nanoparticles and the periodic structural change suggests that this structural change might participate in the mechanism of magnetite formation. The C-terminal domain of Mms6 displays ferric reductase activity that is diminished in the mutant C-terminus. Although it does not play a role in the *in vitro* formation of magnetite during which both ferrous and ferric forms of iron are provided, this reductase activity may participate in magnetite formation *in vivo*.

Introduction

Biomineralization is the process by which living organisms to form highly ordered mineralized structures with hierarchical structure at nanometer scales. The mechanisms regarding biomineralization are poorly understood. However, in those cases for which there is some understanding of the biological mechanisms involved in biomineralization, proteins have been found responsible for forming the mineral structures(1-3). It has been proposed that the mechanism(s) involved in biomineralization may include the control of size, morphology, orientation, composition and the location of crystals synthesized (4). The role of proteins in the biomineralization process is critical considering the physiological environments that

biomineralization occurs and the high temperatures and pressures required to achieve the same goals *in vitro*.

Magnetotactic bacteria that can synthesize highly uniformed magnetic nanoparticles provide an ideal model for the studies of biomineralization process. Magnetotactic bacteria are aquatic prokaryotes which can migrate when oriented along local geomagnetic lines to find the optimal microaerobic environment to survive. The magnetic nanoparticles are surrounded by magnetosomal lipid bilayers and aligned in chain(s), which provides the physical basis of the magnetotactic trait (5-9).

Mms6 is a magnetosome membrane-associated protein. Its mature form consists of 59 amino acids with a hydrophobic N-terminal half and a highly charged hydrophilic C-terminal half (10). Recent studies have showed that deletion of Mms6 did not completely abolish the formation of magnetite particles, the particles formed by these mutant bacteria are smaller and of a different shape than in the wild type (11). Although these results show that Mms6 may not be the only protein required to promote the formation of iron particles in magnetotactic bacteria, it has not yet been determined if the particles produced by the mutant bacteria have the same magnetic characteristics as the wild-type particles. The possibility of gene redundancy may also complicate the interpretation of these results. The exact function of Mms6 protein *in vivo* remains elusive, however its ability to promote the formation of magnetic nanoparticles *in vitro* is conclusive (10,12-14).

Here, we show that Mms6 undergoes periodical structural change upon iron binding. Analysis of the quaternary structure of Mms6 protein and its C-terminal domain reveals that the C-terminal domain contributes to the overall stability of the quaternary structure of Mms6. Magnetic property measurements of the nanoparticles that are produced in the presence of His-Mms6 and its C-terminal mutants further confirm that the ability to undergo structural changes is correlated with the function of Mms6 protein *in vitro*. In addition, we show that the C-terminal domain of Mms6 displays iron reductase activity, which could be part of the mechanism of crystal packing that is promoted by Mms6.

Experimental Procedures

Materials— His-Mms6 and its mutants (His-m2Mms6 and His-m3Mms6) were expressed and purified as described previously (12,15). The C-terminal domain of Mms6 (C21Mms6: KSRDIESAQSDEEVELRDALA) and its mutants (m2C21Mms6: KDRSIDEAQESDSVELREALA; m3C21Mms6: QSLERAEDEDADISAVEKLSR) were chemically synthesized by Genscript (Genscript Corp., www.genscript.com).

Fluorescence spectroscopy— Tryptophan fluorescence of His-Mms6 was measured in a 96-well plates with a fluorescence spectrophotometer (Varian, Model: Cary Eclipse) at 25 ℃, and at excitation and emission wavelengths of 290 nm and 340 nm respectively. In this assay, five μM His-Mms6 or His-m2Mms6 in 50 mM sodium formate, 100 mM KCl, pH 3 were mixed with or without $FeCl_3$ at molar ratios of protein:$FeCl_3$ from 1:1 to 1:23 (inclusive of all unit values) and monitored

by fluorescence (Ex: 290 nm, Em: 340 nm) after having been incubated at 25 ℃ for 2 h.

Size exclusion chromatography— Chromatography was performed with an AKTA FPLC system (GE healthcare) by passing the samples through a prepacked Superdex G75 10/300GL (separation range: 1 kDa-75 kDa) or Superdex Peptide 10/300GL column (separation range: 700 Da-20 kDa) (GE healthcare). The elution profiles of His-Mms6, His-m2Mms6 and His-m3Mms6 were generated using a flow rate of 0.4 mL/min at 4℃ through a Superdex G75 column and monitored by A280. The elution profiles of C21Mms6, m2C21Mms6 and m3C21Mms6 were generated using a flow rate of 0.4 mL/min at 4 ℃ through a Superdex Peptide 10/300GL column and detected by o-phtalaldehyde(16,17) (OPA, Thermo Scientific). In this assay, 200 μL of OPA was added to 20 μL of each fraction from gel filtration chromatography and the fluorescence of each sample was read in a 96-well plate by a fluorescence spectrophotometer (Varian, Model: Cary Eclipse), at excitation and emission wavelengths of 350 nm and 450 nm respectively. All samples were centrifuged at 14,000 *g*, 4 ℃ for 1 h before loading on the column.

Blue dextran was used to determine the void column volume (V_o) of each column. The elution volumes (V_e) of bovine serum album (MM 66 kDa), ovalbumin (MM 44.3 kDa), carbonic anhydrase (MM 29 kDa), myoglobin (MM 17.6 kDa), aprotinin (MM 6.5 kDa) and B12 (MM 1355 Da) (all from Sigma) obtained by Superdex G75 10/300GL were used to generate the standard curve for the apparent molecular mass estimations of His-Mms6, His-m2Mms6 and

His-m3Mms6. The elution volumes (V_e) of cytochrome c (MM 10.37 kDa, aprotinin (MM 6.5 kDa), insulin B chain oxidized form (MM 3495 Da) and B12 (MM 1355 Da) (all from Sigma) from a Superdex Peptide 10/300GL column were used to generate the standard curve for the apparent molecular mass estimations of C21Mms6, m2C21Mms6 and m3C21Mms6.

UV spectroscopy— The interaction between His-Mms6 and C21Mms6 was investigated by monitoring the absorbance change of His-Mms6 at A280 upon C21Mms6 addition at 25 ℃. In this assay, His-Mms6 (40 μM) was mixed with C21Mms6 at molar ratios of His-Mms6: C21Mms6 from 0 to 1:10 for 1h followed by 15 min of centrifugation at 14000 *g* at 25 ℃. The absorbance at 280 nm of the resulting supernatants was then measured by spectrophotometer (Nanodrop, model: ND-100).

Nuclear magnetic resonance (NMR) Spectroscopy— NMR analysis was performed on a Bruker AVII700 equipped with a 5 mm TCI cryoprobe. All NMR analyses were performed at sample temperature of 25 ℃. 2D 1H-1H TOCSY and NOESY spectra were collected using standard experimental protocols (Bruker pulse programs mlevgpgp19 and noesygpph19, respectively) with WATERGATE solvent suppression. The TOCSY experiment consisted of 256 time increments of 8 scans each, with a total acquisition time of 43 min and MLEV17 mixing time of 80 ms. The NOESY experiment consisted of 512 time increments of 64 scans each, with a total acquisition time of 7.5 h and NOESY mixing time of 400 ms. All NMR data were processed and analyzed using Bruker Topspin 2.1 software.

Ferric reductase assay— The ferric reductase assay was measured in 96-well plates aerobically at 25 ℃ with a microplate reader (Bioteck Ceres 900C). The ferric reductase activities of C21Mms6 were measured by detecting the ferrous iron reduced from ferric iron using ferrozine.(18-20) The assay mixture contained 0.1 mM NADH, 25 μM or 75 μM ferric citrate, 1 μM flavin mononucleotide (FMN), 1 mM ferrozine (all from Sigma) and 85 μM C21Mms6 in 20 mM Tris-HCl, 100 mM KCl, pH 7.5 in a total volume of 250 μL. The reaction was initiated by addition of C21Mms6. The increase of A562 was recorded every 2 min on a microplate reader (Biotek, Model: Ceres 900). A mixture containing the same components (exclude C21Mms6) as the assay mixture was used as blank. The concentration of ferrous iron was determined by A562 using extinction coefficient of 28 mM^{-1} cm^{-1}.(21) The specific activity is expressed as nmol Fe^{2+} formed/min/mmol protein.

Magnetic measurements— Magnetization measurements were carried out using a *Quantum Design* SQUID (Superconducting Quantum Interference Device) 5T MPMS (Magnetic Properties Measurement System). Specimens were cooled in zero magnetic field to 5K, a negative magnetic field of – 5T was applied and then reversed to 500 Oe to insure complete magnetization reversal in each particle and removal of any metastable states. Measurements were taken while warming the sample to 296K (ZFC-W process) and then on cooling back to 5 K (FC-C process). The blocking temperature was determined as a maximum on the ZFC-W curve.

Transmission electron microscopy— Samples were imaged with a Tecnai G^2 F20 Scanning Transmission Electron Microscope (FEI Company, Hillsboro OR)

equipped with high angle annular dark field (HAADF) and energy dispersive X-ray spectroscopy (EDX) detectors at operating voltage 200 KV. Washed magnetites (20 µL of aqueous suspension) were dispersed in 2 mL of ddH_2O and 20 µl of this suspension was deposited on a carbon-supported electron microscopy copper grid.

Results

Mms6 undergoes periodically structural changes with increasing iron concentration. Our previous studies have shown that His-Mms6 undergoes slow (over a period of hours) structural changes upon ferric iron binding.(15) Here we further examined the effect of ferric iron on the structure of His-Mms6 by monitoring the tryptophan fluorescence quenching upon ferric iron binding. There are two tryptophan residues in the N-terminal domain of Mms6 (W5 and W21) and quenching of tryptophan fluorescence was observed upon ferric iron binding. A periodic tryptophan quenching profile was observed with respect to the molar ratio of iron to protein with a periodicity of 12 Fe^{3+}/His-Mms6 (Fig. 1,■,●). Fig. 1B shows the averaged results from 5 independent experiments for His-Mms6 (●) and His-m2Mms6 (○). Although all experimental datasets show the same periodicity, the amplitude varies greatly and thus the standard deviation is large when all datasets are averaged. We do not know the reason for this variability. No significant change in fluorescence was observed with His-m2Mms6 (Fig. 1,□, ○).

Ability to undergo structural changes correlates with the ability to form particles. To examine the possible significance of the periodic structural changes in Mms6

when binding iron, we determined the structure and magnetic properties of the magnetites formed in the presence of His-Mms6 and His-m2Mms6 (Fig. 2). The results showed that crystals of about 30 nm in diameter were formed in the presence of His-Mms6 but not in the presence of His-m2Mms6 (Fig. 2 Inset). The blocking phenomenon (and its characteristic “blocking” temperature) is a signature of the superparamagnetic regime that depends on the particle size, degree of crystallinity and interparticle interactions. Below the blocking temperature, the random magnetic moments of individual nanoparticles cannot align with the applied field. The blocking temperature is reduced when the size or crystallinity of the the particles are reduced (11). The particles synthesized in the presence of His-Mms6 exhibited a blocking temperature (Fig 2, ☆) typical of superparamagnetic particles compared with the lower blocking temperatures that characterized the particles produced in the presence of His-m2Mms6 (Fig 2, ▽) and in the absence of protein (Fig 2, ●).

C-terminal domain contributions to the overall stability of His-Mms6 quaternary structure. Our previous studies showed that His-Mms6 forms a stable micellar quaternary structure in an aqueous environment (15). From its primary sequence, which contains a large proportion of Leu-Gly repeats and hydrophobic amino acids (Supplementary Table.2), we speculate that the driving force for the formation micelles are hydrophobic and van der waals interactions. However, we have also observed that the C-terminal domain, which is replete with hydrophilic amino acid side chains, also forms quaternary structures. We used size exclusion chromatography to examine the contribution of the C-terminal domain to the

quaternary structure of His-Mms6. Whereas the chromatogram of His-Mms6 appeared as a single peak in the void volume of the column, the chromatograms of His-m2Mms6 and His-m3Mms6 both revealed multiple peaks on Superdex G75 column (Fig. 3A). The apparent molecular mass of the 3 peaks corresponded to multimeric (≥75 kDa), trimeric (~30 kDa) and monomeric (~10 kDa) forms of His-m2Mms6 (multimeric (≥75 kDa), dimeric (~20 kDa) and monomeric (~10 kDa) forms for His-m3Mms6). When examined by denaturing (SDS) PAGE gel the samples from all the peaks migrated to the same position, thus confirming that all peaks on the column contained the same monomeric form of His-Mms6 mutants. To examine if the separated peaks of protein multimers are in equilibrium, the void volume samples for His-m2Mms6 and His-m3Mms6 were retrieved and run again through the column. These rerun samples distributed similarly as multiple peaks when separated through the column for both (Supplementary Fig.9). These results showed that the changes in the Mms6 C-terminal domain result in decreased stability of the overall quaternary micellar structure of Mms6.

We further examined the structures of the 21 amino acid C-terminal domain of His-m2Mms6 and His-m3Mms6 (referred to here as m2C21Mms6 and m3C21Mms6 respectively). The elution profile of m2C21Mms6 and m3C21Mms6 also reveals multiple peaks (Fig. 3B, ◊, ●). The apparent molecular mass corresponded to trimeric (~6.9 kDa) and dimeric (~4.6 kDa) forms of m2C21Mms6 (trimeric (~6.9 kDa, dimeric (~4.6 kDa and monomeric (~2.3 kDa) forms for m3C21Mms6). The NOESY spectrum of m2C21Mms6 revealed less non-sequential, inter-residue amide

to side-chain NOE cross peaks than that of C21Mms6 (Fig. 4) (the assignments of spectra and structural modeling of m2C21Mms6 are ongoing, Bruce Fulton, personal communication).

If the C-terminal domain contributes to the overall quaternary structure of His-Mms6, we might be able to destroy that structure by interfering with the C-terminal domain interactions. SDS-PAGE gel showed that when C21Mms6 and His-Mms6 were mixed, a precipitant containing His-Mms6 and C21Mms6 was formed (Supplement Fig 3). To determine the stoichiometry, we titrated His-Mms6 with C21Mms6. Increasing molar ratios of C21Mms6 to His-Mms6 resulted in graded precipitation of His-Mms6 starting after a molar ration of 3:1 (C21Mms6:His-Mms6) with complete precipitation occurring at a ratio of 7:1 and above (Fig. 5). These results show that the quaternary structure of His-Mms6 is disrupted by additional C21Mms6 with the outcome that the protein is no longer soluble. Similar results were obtained when the C-terminal domain was cleaved from the protein with proteinase K. Thus, we speculate that C21Mms6 may dislodge the C-terminal domain from its structural integration in the His-Mms6 micelle and thereby expose the N-terminal hydrophobic core of the micelle to water. Another possible explanation is that the free C-terminus may act as a cross-linker of His-Mms6 micelles and promote the formation of higher ordered structures that precipitate. The results suggest that each C-terminal domain of Mms6 can interact with 7 other C-terminal domains and therefore suggest that the C-terminal domain of Mms6 exists as an octamer on the surface of the micelle.

C21Mms6 has ferric reductase activity. With the observation that Mms6 cannot bind ferrous iron to incorporate it into the growing magnetite crystals (Supplementary Fig. 10), we speculated that instead Mms6 may incorporate Fe^{2+} into the crystals by way of reducing bound Fe^{3+}. We observed that C21Mms6 has ferric reductase activity in an assay in which ferric citrate was the source of Fe^{3+} and NADH was the electron donor with the addition also of FMN (Fig. 6). The specific reductase activity of C21Mms6 was determined to be 48.5±3.0 nmol Fe^{2+}/min/mmol C21Mms6 (turnover rate: 14.3 days) and 128.6±8.9 nmol Fe^{2+}/min/mmol C21Mms6 (turnover rate: 5.4 days) when the ferric citrate concentration was 25 μM (Fig. 6A, ●) and 75 μM (Fig. 6B, ●) respectively. The m2C21Mms6 had no reductase activity at 25 μM ferric-citrate (Fig. 6A, ○), but had some activity at 75 μM ferric citrate (59.0±6.0 nmol Fe^{2+}/min/mmol m2C21Mms6, turnover rate: 17.8 days) (Fig. 6B, ○). To establish that the reductase activity observed in these experiments reflects a specific property of the Mms6 C-terminal domain, we tested m3C21Mms6 under these experiment conditions and found no activity at either concentration of iron (Fig. 6 ■).

Discussion

In our previous studies, we reported that, in aqueous solution, Mms6 forms a micellar quaternary structure that has two phases of iron binding; a stoichiometric high affinity binding phase and a high capacity but low affinity binding that is cooperative with respect to iron concentration (15). Here, we further investigate

the relation between quaternary structure of Mms6 and the ability of this protein to promote the formation of superparamagnetic magnetite particles.

An important driving force for the formation of His-Mms6 protein micelle is likely to be the hydrophobic interactions as it is evident that the primary sequence of Mms6 protein contains a large portion of Leu-Gly repeats and hydrophobic amino acids. Our previous studies showed that the quaternary structure of Mms6 to be a bipolar micellar structure with the C-terminal domain exposed on the surface of the molecule (15). The results of titration of the C-terminal domain with C21Mms6 suggests that this domain may interact on the surface of the micelle as an octamer and that disrupting the surface interactions of adjacent C-terminal domains by an external domain destabilizes the quaternary structure of the multimer resulting in its precipitation. Coincidently, similar observations have been made with amelogenin which is responsible for the biomineralization of enamel (22,23).

Following up on our observation that Mms6 undergoes a slow structural change on binding iron, we investigated the effect of molar ratio of iron on the Mms6 structure and discovered curious periodic relationship with the periods extending over a 12 molar units of iron to Mms6. Although we do not yet understand the molecular basis for this structural change, we note that the periodic relation is a multiple of three and that the high capacity iron binding activity of Mms6 is cooperative with respect to iron and with a Hill value of 3. Thus, an iron to Mms6 ratio of three might be the minimal grouping by which the protein incorporates iron into a magnetite crystal. This number is also compatible with the magnetite iron

composition, which is iron II:III in a 1:2 ratio. From these deductions, we speculate that Mms6 might bind iron in a 3:1 ratio of iron:Mms6 and with this grouping Mms6 reduces one of the iron atoms. The structural change of Mms6 returns to the original condition at a ratio of iron:Mms6 of 12, which could involve 4 sets of 3 iron molecules incorporated into a growing magnetite crystal by an octamer of the C-terminal domain. The periodic change in environment of the N-terminal tryptophan(s) as iron is added to the protein may reflect a rotation of the protein as it incorporates iron into a crystalline structure.

Although we observed the reductase activity with the isolated C-terminal domain of Mms6, this peptide cannot form magnetic particles without being linked to the N-terminal domain or a polymer that forms a micelle (13). Even without these linkages C21Mms6 interacts as a dimer. However, in the context of the N-terminal domain we have observed that this protein is a multimer and speculate that the multimer is the functional unit for the formation of magnetite. Our evidence suggests that both the N- and the C-terminal domains contribute to maintaining the structure of the multimeric form of Mms6, which is a micelle in aqueous solution, but could exist as islands of interacting proteins in a bacterial membrane.

The surface fluorescence measurements show that His-Mms6 and His-m2Mms6 selectively binds ferric iron not ferrous iron (Supplementary Fig. 10). The observation led us to examine the C-terminal domain for ferric reductase activity and we observed that the C-terminal domain (C21Mms6) of Mms6 has ferric reductase

activity and that m2C21Mms6 also shows some reductase activity, although at higher ferric iron concentration. These results suggest that the high affinity binding of iron is important for organizing C21Mms6 structurally so as to bring the appropriate amino side chains into position to form that catalytic site of this reductase. Shuffling the positions of the –COOH and –OH groups as was done for m2Mms6 left this protein with a lower affinity for iron, which is consistent with the observation that a higher concentration of iron is required for catalytic activity. Implicit in this interpretation is the expectation that the critical residues that form the active reductase catalytic site are not those residues that were shuffled in m2C21Mms6 and that even the low affinity binding of iron to the debilitated iron binding site results in a structure that supports catalytic activity in m2C21Mms6. The observation of reductase activity suggest that reduction of ferric iron may be part of the mechanism of magnetite formation by Mms6 as previously proposed (24).

An important finding in this study is the correlation between the ability of Mms6 to undergo periodic structural changes and the ability to template the formation of magnetic nanoparticles. High-resolution transmission electron microscopy of the iron oxy-hydroxide crystals formed by iron-oxidizing bacteria revealed that the mechanism of the crystals formation involves the aggregation of adjacent 2-3 nm particles followed by the orientation of these particles to parallel in three dimensions (25). The sizes and shapes of crystals formed by magnetotactic bacteria are genetically defined and thus the consequence of the biomineralization protein(s) (26-29). Knockout bacteria that lack Mms6 gene produce altered crystal shapes.

Our results suggest that the iron binding properties and quaternary structure of Mms6 is responsible for formation of the cubo-octahedral crystal structures of *Magnetospirillum magneticum* strain AMB-1. We speculate that biomineralization proteins from magnetotactic bacteria that form different crystal structures might adopt different quaternary structures. However, the possession of a quaternary structure and the ability of that structure to change as iron is incorporated into a crystal, may be more fundamental aspects of the mechanism by which a small protein such as Mms6 can promote the formation of magnetite crystals that are 10-fold larger.

References

1. Moradian-Oldak, J. (2001) *Matrix Biology* **20**, 293-305
2. Cölfen, H. (2010) *Nat Mater* **9**, 960-961
3. Cha, J. N., Shimizu, K., Zhou, Y., Christiansen, S. C., Chmelka, B. F., Stucky, G. D., and Morse, D. E. (1999) *Proceedings of the National Academy of Sciences of the United States of America* **96**, 361-365
4. Gower, L. B. (2008) *Chem. Rev.* **108**, 4551-4627
5. Dunin-Borkowski, R. E., McCartney, M. R., Frankel, R. B., Bazylinski, D. A., Pósfai, M., and Buseck, P. R. (1998) *Science* **282**, 1868-1870
6. Penninga, I., de Waard, H., Moskowitz, B. M., Bazylinski, D. A., and Frankel, R. B. (1995) *Journal of Magnetism and Magnetic Materials* **149**, 279-286
7. Blakemore, R. (1975) *Science* **190**, 377-379
8. Bazylinski, D. A., and Frankel, R. B. (2004) *Nat Rev Microbiol* **2**, 217-230
9. Frankel, R. B., Bazylinski, D. A., Johnson, M. S., and Taylor, B. L. (1997) *Biophys J* **73**, 994-1000
10. Arakaki, A., Webb, J., and Matsunaga, T. (2003) *J. Biol. Chem.* **278**, 8745-8750
11. Tanaka, M., Mazuyama, E., Arakaki, A., and Matsunaga, T. (2011, In press) *Journal of Biological Chemistry*
12. Prozorov, T., Mallapragada, S. K., Narasimhan, B., Wang, L., Palo, P., Nilsen-Hamilton, M., Williams, T. J., Bazylinski, D. A., Prozorov, R., and Canfield, P. C. (2007) *Advanced Functional Materials* **17**, 951-957
13. Prozorov, T., Palo, P., Wang, L., Nilsen-Hamilton, M., Jones, D., Orr, D., Mallapragada, S. K., Narasimhan, B., Canfield, P. C., and Prozorov, R. (2007) *ACS Nano* **1**, 228-233
14. Arakaki, A., Masuda, F., Amemiya, Y., Tanaka, T., and Matsunaga, T. (2010) *J Colloid Interface Sci* **343**, 65-70
15. Wang, L., Feng, S., Palo, P., Fulton, D. B., and Nilsen-Hamilton, M. (2011) *Submitted*
16. Benson, J. R., and Hare, P. E. (1975) *Proceedings of the National Academy of Sciences of the United States of America* **72**, 619-622
17. Drescher, D. G., and Lee, K. S. (1978) *Analytical Biochemistry* **84**, 559-569
18. Stookey, L. L. (1970) *Anal. Chem.* **42**, 779-781
19. Dailey, H. A., Jr., and Lascelles, J. (1977) *J. Bacteriol.* **129**, 815-820
20. Noguchi, Y., Fujiwara, T., Yoshimatsu, K., and Fukumori, Y. (1999) *J. Bacteriol.* **181**, 2142-2147
21. Carter, P. (1971) *Analytical Biochemistry* **40**, 450-458
22. Moradian-Oldak, J., Bouropoulos, N., Wang, L., and Gharakhanian, N. (2002) *Matrix Biology* **21**, 197-205
23. Du, C., Falini, G., Fermani, S., Abbott, C., and Moradian-Oldak, J. (2005) *Science* **307**, 1450-1454

24. Frankel, R. B., Papaefthymiou, G. C., Blakemore, R. P., and O'Brien, W. (1983) *Biochimica et Biophysica Acta (BBA) - Molecular Cell Research* **763**, 147-159
25. Banfield, J. F., Welch, S. A., Zhang, H., Ebert, T. T., and Penn, R. L. (2000) *Science* **289**, 751-754
26. Murat, D., Quinlan, A., Vali, H., and Komeili, A. (2010) *Proceedings of the National Academy of Sciences* **107**, 5593-5598
27. Ding, Y., Li, J., Liu, J., Yang, J., Jiang, W., Tian, J., Li, Y., Pan, Y., and Li, J. (2010) *J. Bacteriol.* **192**, 1097-1105
28. Yang, W., Li, R., Peng, T., Zhang, Y., Jiang, W., Li, Y., and Li, J. (2010) *Research in Microbiology* **161**, 701-705
29. Scheffel, A., Gardes, A., Grunberg, K., Wanner, G., and Schuler, D. (2008) *J. Bacteriol.* **190**, 377-386

Footnotes

This work was supported by the U. S. Department of Energy, Office of Basic Energy Science, Division of Materials Sciences and Engineering. The research was performed at the Ames Laboratory. Ames Laboratory is operated for the U. S. Department of Energy by Iowa State University under Contract No. DE-AC02-07CH11358.

Figure Legends

Fig. 1. His-Mms6 undergoes periodical structural change. A) The two independent representative results for His-Mms6 (■, ●) and His-m2Mms6 (□,○). The fluorescence values were normalized to the value of Fe^{3+}-free sample of each data set. B) The averaged results from 5 independent experiments for His-Mms6 (●) and His-m2Mms6 (○).

Fig. 2. His-Mms6 promotes the formation of superparamatic nanoparticles. Shown are the magnetization measurements of particles synthesized in the presence of His-Mms6 (☆), His-m2Mms6 (▽) or no-protein (●). **Inset**: TEM images of particles synthesized in the presence of His-Mms6, His-m2Mms6 or no-protein.

Fig. 3. C-terminal domain contributes to the overall His-Mms6 quaternary structure. A) The elution profile of His-Mms6, His-m2C21Mms6 and His-m3C21Mms6 in 20mM Tris-HCl, 100 mM KCl, pH7.5 from a Superdex G75 10/300GL column with a flow rate of 0.4 mL/min at 4 ℃. B) The elution profile of C21Mms6 (□), m2C21Mms6 (◊) and m3C21Mms6 (●) in 100 mM KCl, pH7.5 from a Superdex peptide 10/300GL column with a flow rate of 0.4 mL/min at 4 ℃.

Fig. 4. Altered structure of m2C21Mms6. A) The Overlay of the 1H NOESY spectra of C21Mms6 (grey) and m2C21Mms6 (black) spectra in 5% (v/v) D_2O, 100mM KCl, pH 4.9. B) The overlay of The 1H TOCSY spectra of C21Mms6 (grey)

and m2C21Mms6 (black) spectra in 5% (v/v) D_2O, 100mM KCl, pH 4.9 (The assignments of spectra and structural modeling of m2Mms6 are ongoing).

Fig. 5. C-terminal domain of Mms6 exists as an octamer on the surface of the micelle. Shown is the titration curve of 40 μM His-Mms6 in 20 mM Tris-HCl, 100 mM KCl, pH 7.5 titrated with C21Mms6. The absorbance of the supernatant was normalized to 40 μM His-Mms6.

Fig. 6. C21Mms6 exhibits ferric reductase activity. Shown are progress curves of ferric reduction catalyzed by C21Mms6 (●), m2C21Mms6 (○) and m3C21Mms6 (■) when ferric citrate concentration was 25 μM (A) and 75 μM (B).

Figure 1

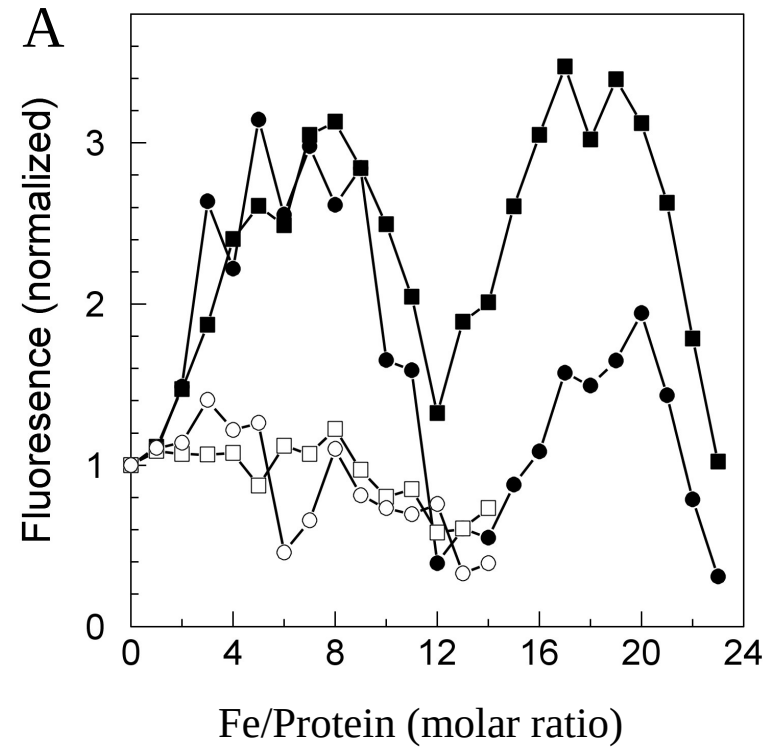
A
Fluoresence (normalized)
0
1
2
3
0
4
8
12
16
20
24
Fe/Protein (molar ratio)

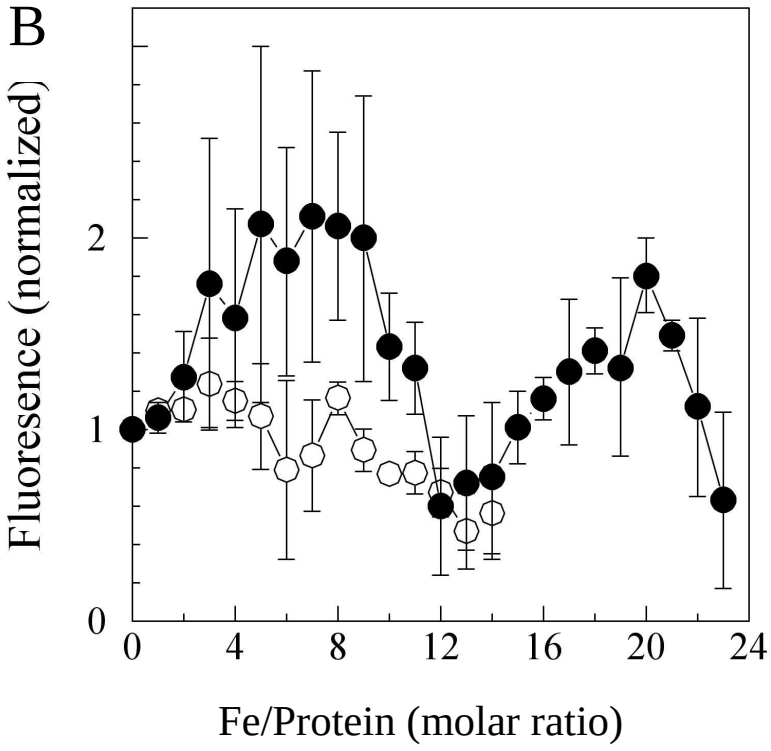
B
Fluoresence (normalized)
0
1
2
0
4
8
12
16
20
24
Fe/Protein (molar ratio)

Figure 2

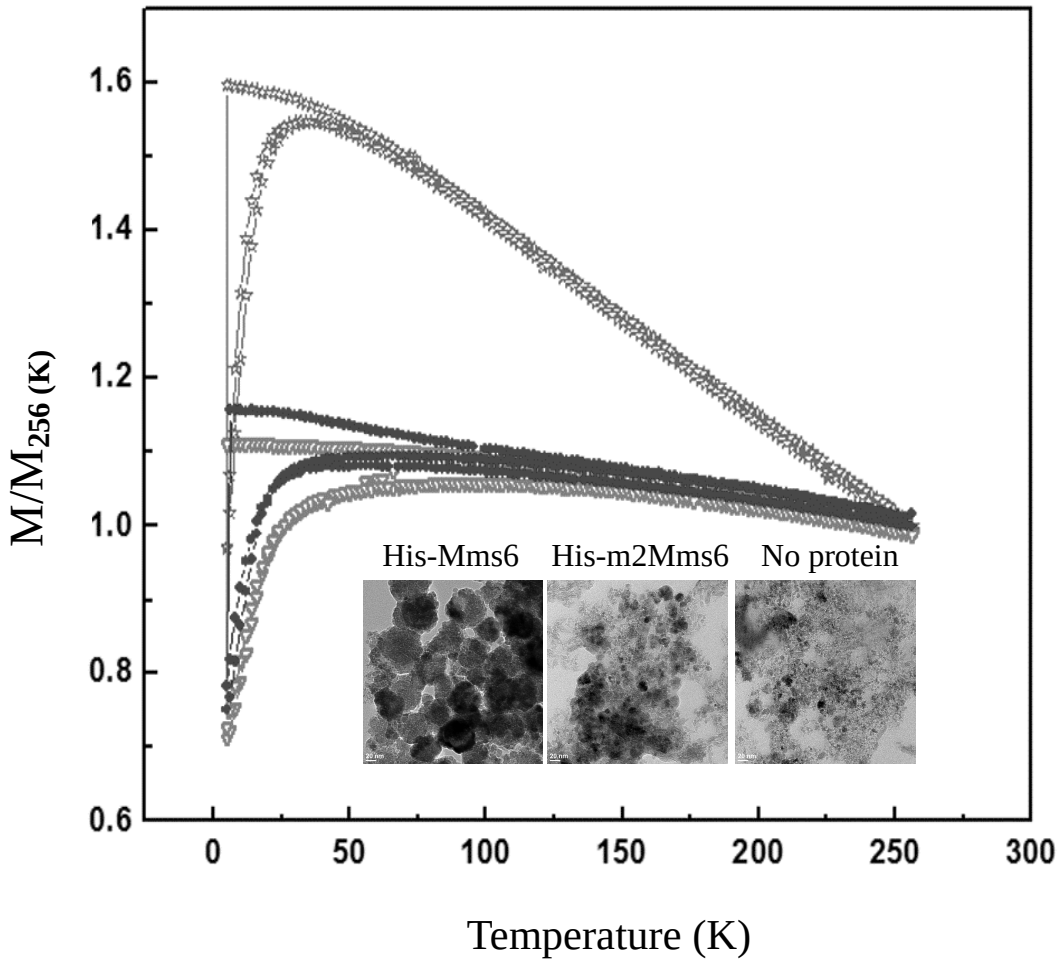
1.6
1.4
1.2
1.0
0.8
0.6
M/M256 (K)
0
50
100
150
200
250
300
Temperature (K)
His-Mms6
His-m2Mms6
No protein

Figure 3

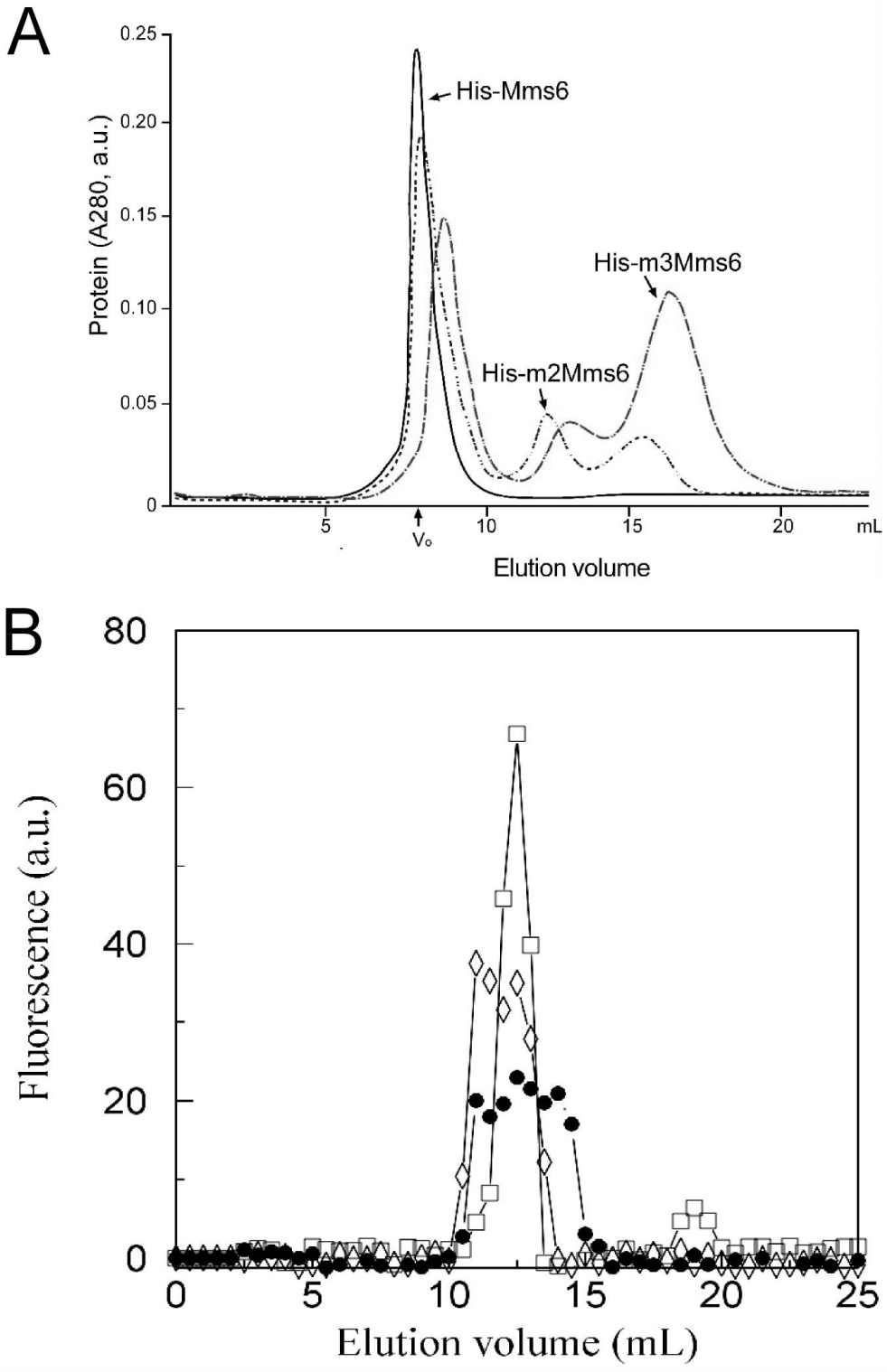
A
Protein (A280, a.u.)
0.25
0.20
0.15
0.10
0.05
0
His-Mms6
His-m3Mms6
His-m2Mms6
5
10
15
20
mL
Vo
Elution volume
B
Fluorescence (a.u.)
80
60
40
20
0
0
5
10
15
20
25
Elution volume (mL)

Figure 4

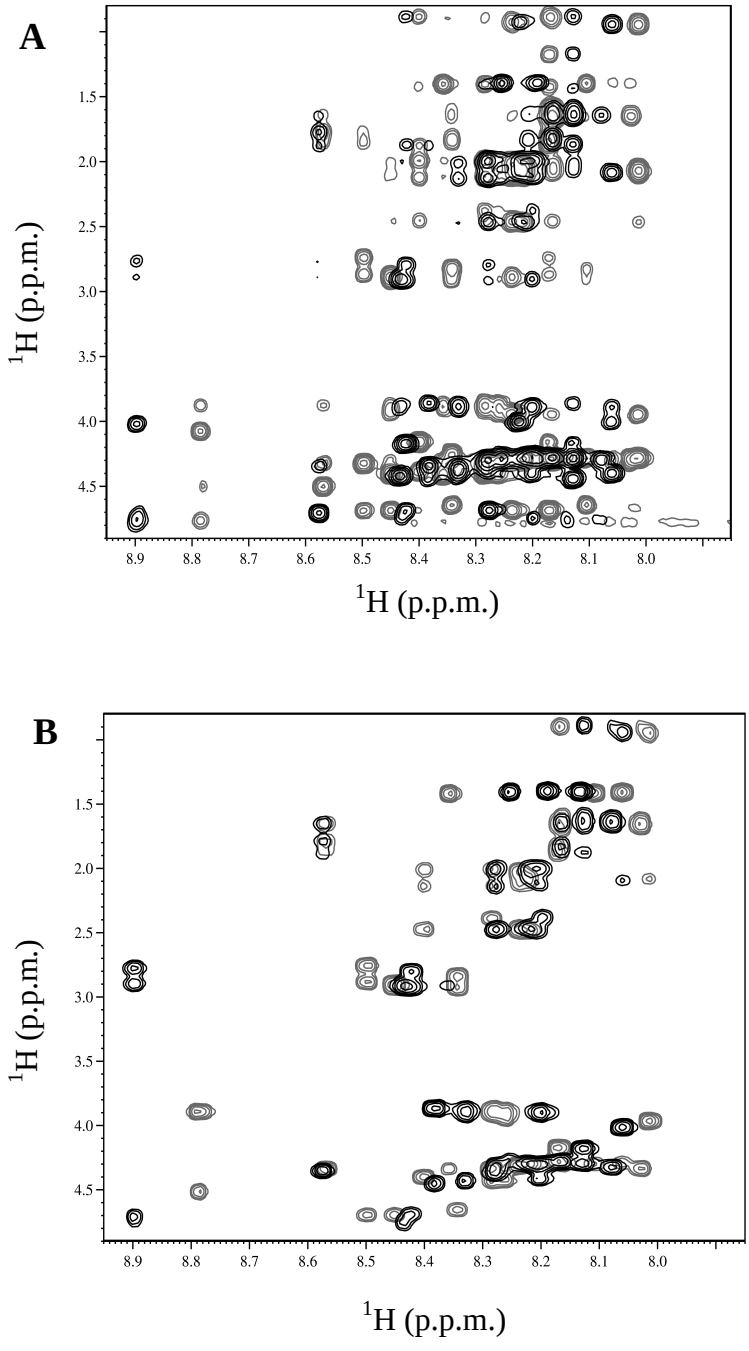

Figure 5

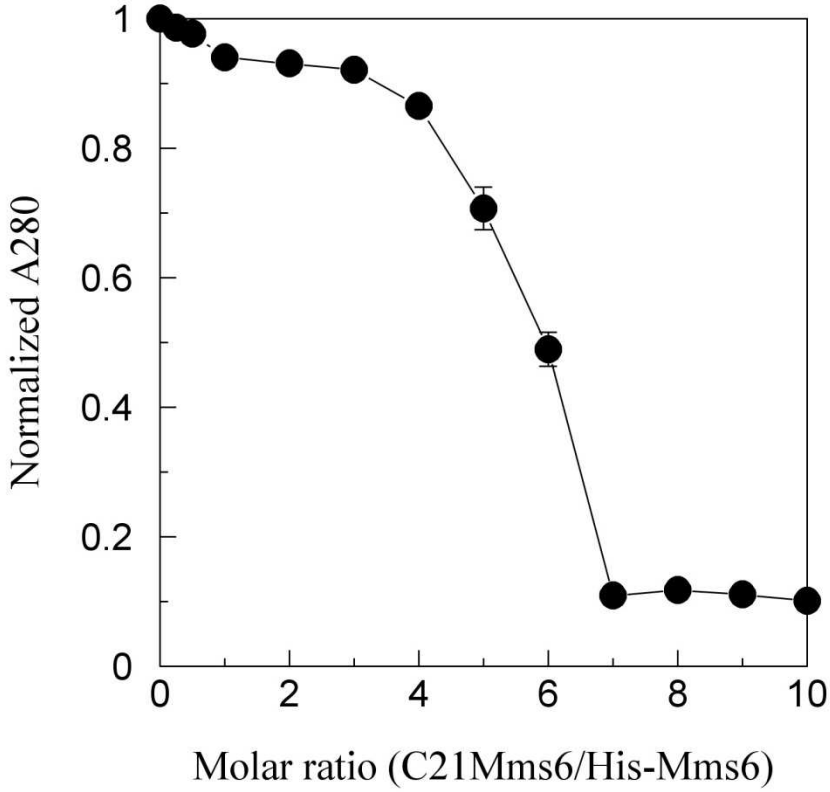
Normalized A280
1
0.8
0.6
0.4
0.2
0
0
2
4
6
8
10
Molar ratio (C21Mms6/His-Mms6)

Figure 6

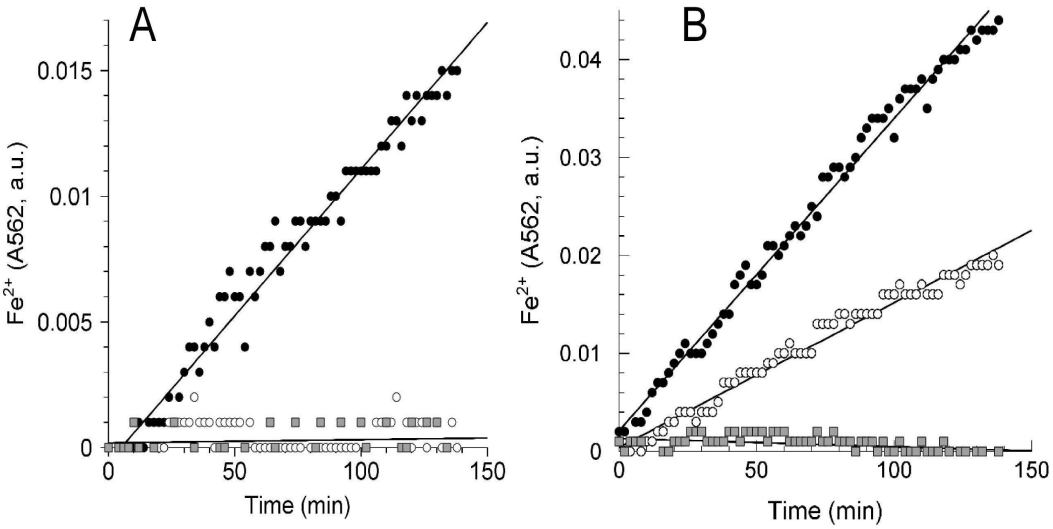

CHAPTER 4: GENERAL CONCLUSIONS AND FUTURE DIRECTIONS

General conclusions

Here we report structural and functional studies of Mms6, a biomineralization protein that can promote the formation *in vitro* of magnetic nanoparticles with sizes and morphologies similar to the magnetites synthesized by magnetotactic bacteria. We found the binding pattern of Mms6 to ferric ion to be two-phase and multivalent. We quantatively determined that Mms6 binds one Fe^{3+} with a very high affinity ($K_d = 10^{-16}$ M). The second phase of iron binding is multivalent and cooperative with respect to iron with a K_d in the μM range and a stoichiometry of about 20 ferric ion per protein molecule.

We found that Mms6 exists in large particles of two sizes, one consisting of 20-40 monomeric units and the other of 200 units. From proteolytic digestion, ultracentrifugation and liposome fusion studies, we found that Mms6 forms a large micellar quaternary structure with the N-terminal domain self-assembling into a uniformly sized micelle and the C-terminal domain on the surface.

The two-phase iron-binding pattern may be relevant to iron crystal formation. We propose that the first high affinity phase may stabilize a new conformation of the C-terminal domain that allows interaction with other C-terminal domains leading to a structural change in the multimeric protein complex that enables the second low affinity iron binding phase to organize iron and initiate crystal formation.

We also observed a dimeric apparent molecular mass of the Mms6 C-terminal peptide (C21Mms6). We speculate that the C-terminal domain may form higher

order quaternary arrangements on the surface of the micelle or when anchored to a membrane by the N-terminal domain. The change in fluorescence quenching in the N-terminal domain with iron binding suggests a structural integrity between the C- and N-terminal domains. The slow change in trp fluorescence as a function of time after adding iron suggests a very slow conformational change in the protein that involves both N- and C-terminal domains. We interpret these results to mean that there is a coordinated global change in Mms6 structure that involves multiple Mms6 monomers.

Based on our observations, we propose a mechanism by which Mms6 can promote the formation of crystalline nanoparticles. Upon binding ferric iron at very high affinity with a molar ratio of 1, the C-terminal domains undergo a conformational change, coordinated with the N-terminal domain that initiates a slow rearrangement of the multiprotein complex to create a surface on which many iron atoms can organize. This slow rearrangement allows the initiation of a crystal that is propagated on the protein surface to form a crystal seed.

We also observed that Mms6 undergoes a periodical structural change with increasing molar ratios of iron to protein. The observed structural change occurs in the N-terminal domain, but reflects iron binding by the C-terminal domain. A mutant Mms6 that does not promote the formation of superparamagnetic magnetite also does not undergo the periodic structural change. The correlation between the ability to form magnetic nanoparticles and the ability to undergo the periodic

structural change suggests that this structural change might participate in the mechanism of magnetite formation.

Analysis of the quaternary structure of Mms6 protein and its C-terminal domain reveals that the C-terminal domain contributes to the overall stability of the quaternary structure of Mms6. The C-terminal domain of Mms6 displays ferric reductase activity that is diminished in the mutant C-terminus. Although it does not play a role in the *in vitro* formation of magnetite during which both ferrous and ferric forms of iron are provided, this reductase activity may participate in magnetite formation *in vivo*.

Our results suggest that the iron binding properties and quaternary structure of Mms6 is responsible for formation of magnetic nanoparticles. The ability for Mms6 protein to form a quaternary structure and the ability of that structure to change as iron is incorporated into a crystal may be fundamental aspects of the mechanism by which a small protein such as Mms6 can promote the formation of magnetite crystals.

Future directions

Biomineralization has been a hot topic for decades while its mechanism remains elusive. The studies presented here are just a beginning towards fully understanding protein-promoted magnetic nanoparticle formation. Some critical questions remain to be answered.

The His-tagged recombinant form of Mms6 used in this study may cause some misinterpretation regarding the results, so it will be desirable to obtain the Mms6

without His-tag. In this regard, a C-terminal His-tagged recombinant form of Mms6 might be a good choice because the C-terminal domain of Mms6 protein is expected to be easy accessible to proteases.

The model presented here needs further testing. The question of whether the overall structural change is caused by the high affinity binding to iron or the cooperative binding to iron remain to be answered. In this regard, it is necessary to identify the binding sites responsible for the high affinity binding to iron by site-directed mutagenesis.

The correlation between the slow and periodic structural changes of Mms6 and the ability to promote the formation of magnetic nanoparticles needs to be investigated. Because Mms6 forms large protein micelle, solid state nuclear magnetic resonance spectroscopy will be the ideal technique to use. It will be interesting to see whether these changes in Mms6 structure reflect a process of orienting bound iron clusters to certain positions or angles that promote the formation of magnetites with specific morphologies.

The ability of Mms6 to template the formation of magnetic nanoparticles is amazing. Cobalt ferrite has also been successfully synthesized in the presence of Mms6. It will be interesting to determine if Mms6 promotes the formation of other metal nanoparticles such as Ru, Mn or Ni.

The reductase activity of Mms6 protein is another interesting aspect worth exploring. In this regard, an alanine scan of the –OH and –COOH groups in the C-terminal domain of Mms6 will be useful to identify the residues responsible for

the reductase activity. It will be interesting to see whether the groups responsible for the reductase also participate in the high affinity iron binding.

Both the C-terminal domain and His-Mms6 show reductase activity. However, the nature of the His-Mms6 reductase activity is as yet not fully understood because in some cases the activity appears hysteretic, being delayed in time in its appearance after the addition of iron, and in other cases the activity begins immediately after adding iron. Thus, the reductase activity of Mms6 needs to be fully characterized. Conditions such as pH and buffer components used in the experiment need further optimization and different electron donors (such as NADPH) and cofactors (if any is required) should be tested. The enzymatic constants, such as K_m and V_m, need to be determined. The inhibitory effect of another metal irons, such as Ni, Ca or Co need to be examined. It will be interesting to see whether factors that inhibit the reductase activity will also inhibit the formation of magnetic nanoparticles.

SUPPLEMENTARY FIGURES AND TABLES

Fig 1: His-Mms6 forms monolayer at the liquid-air interface. The surface pressure isotherms of His-Mms6 were measured by a Langmuir-Blodgett trough (Type611, Nima Technology). The His-Mms6 protein sample (2.36 μg) was directly added onto the surface of 500 ml of buffer, which containing 20 mM Tris-HCl, 100 mM KCl, pH 7.5 or pH 3 at 25 ℃ hold by the trough. The surface pressure isotherms were then measured with a compression speed of 10 cm^2/min. His-Mms6 forms a monolayer at the liquid-air interface on a buffer containing 20 mM Tris, 100 mM KCl, pH 7.5 (solid line) or pH 3 (dash line). When the monolayer is compressed, the surface pressure is increased. The increase of the surface pressure due to individual protein molecules making contact can be used to estimate the molecular area (1-4). The molecular area can be obtained by dividing the surface area at which the increase in surface pressure observed by the number of molecules spread on the surface. The molecular area was about 8000 $Å^2$ at both pHs. The ability of His-Mms6 to form a monolayer at both pH 7.5 and pH 3 indicates that the quaternary structure of His-Mms6 is a micelle and not protein aggregates (5,6).

Fig 1

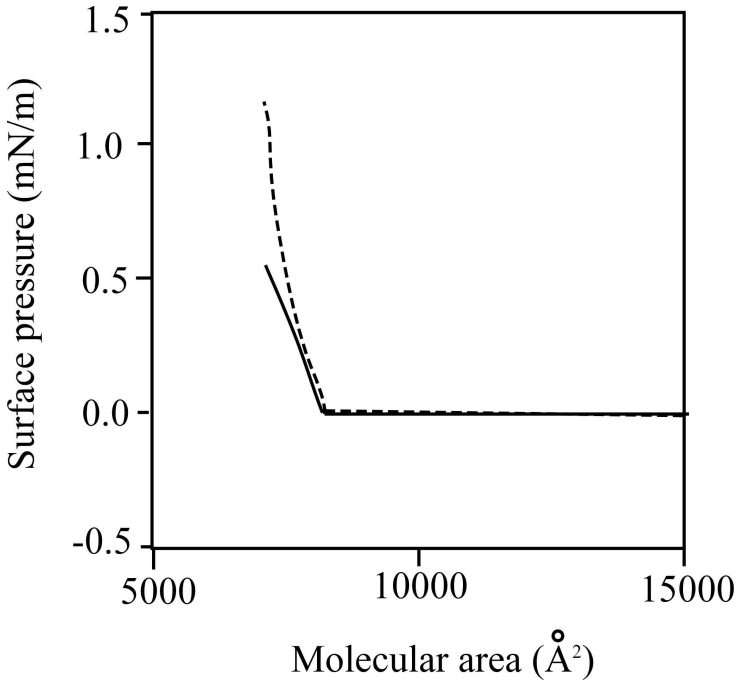
1.5
1.0
0.5
0.0
-0.5
Surface pressure (mN/m)
5000
10000
15000
Molecular area (Å²)

Fig 1

Fig 2: C21Mms6 runs as a monomer in 6 M GnCl (guanidine hydrochloride). Shown are the standard curve (A) used to estimate the apparent molecular mass of C21Mms6 in 20 mM Tris, 100 mM KCl, 6 M GnCl, pH 7.5 and the chromatogram (B) of the samples used. Blue dextran was used to determine the void column volume (V_o) of the Superdex Peptide 10/300GL column (separation range: 700 Da-20 kDa). The elution volumes (V_e) of cytochrome c (MM 10.37 kDa, aprotinin (MM 6.5 kDa), insulin B chain oxidized form (MM 3495 Da) and B12 (MM 1355 Da) (all from Sigma) from a Superdex Peptide 10/300GL column run at 0.4 mL/min, 4℃ were used to generate the standard curve for the apparent molecular mass estimations of C21Mms6 (○: Standard used; ▲: C21Mms6; The linear regression formula used for MM estimation was Y=-1.54X+5.65). The C21Mms6 doesn't have trp, tyr or phe in its sequence. GnCl interferes with the OPA reagent, which fluoresces when bound to primary amines. So the elution volume of C21Mms6 in 6 M GnCl was identified by PAGE each fraction through a 15 % gel in the presence of 0.1 % SDS.

Fig 2

A

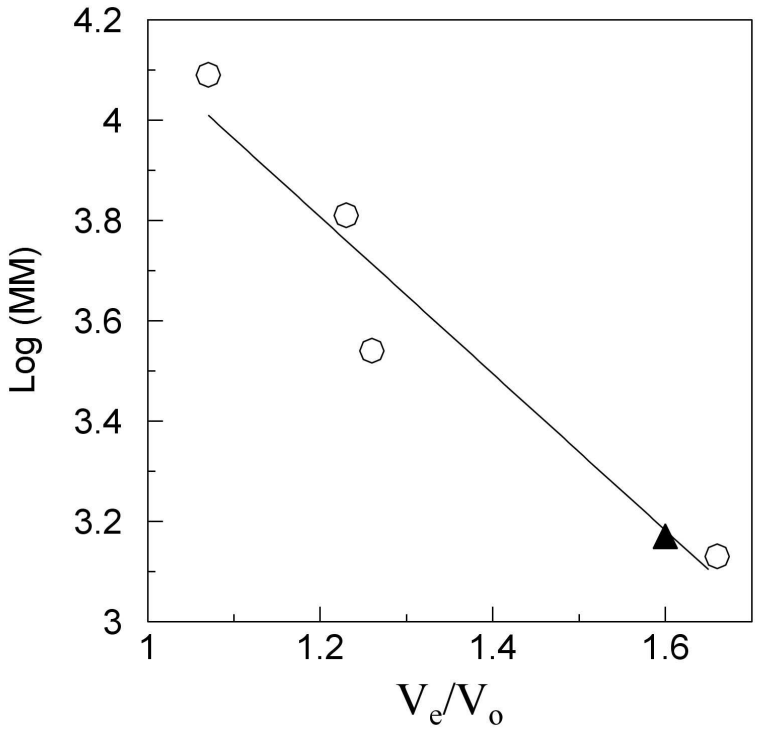
4.2
4
3.8
3.6
3.4
3.2
3
Log (MM)
1
1.2
1.4
1.6
Ve/Vo

B

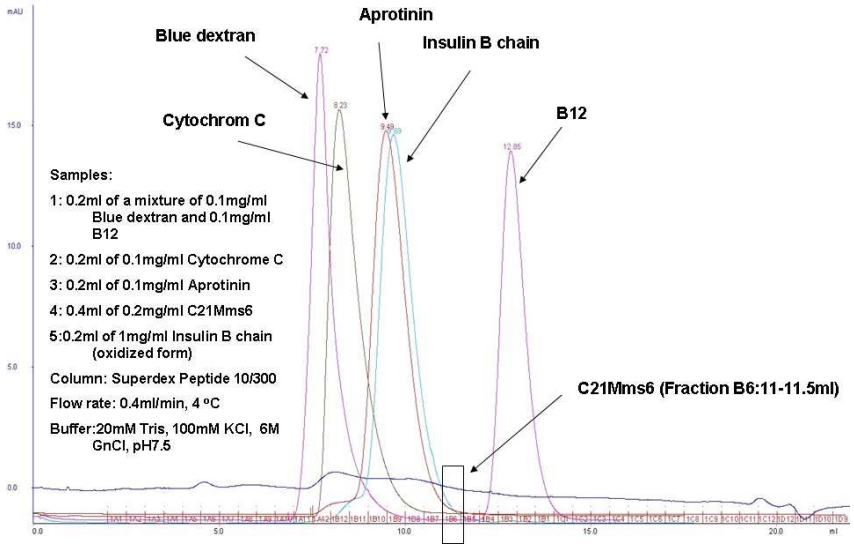
Blue dextran
Aprotinin
Insulin B chain
Cytochrom C
B12
Samples:
1: 0.2ml of a mixture of 0.1mg/ml Blue dextran and 0.1mg/ml B12
2: 0.2ml of 0.1mg/ml Cytochrome C
3: 0.2ml of 0.1mg/ml Aprotinin
4: 0.4ml of 0.2mg/ml C21Mms6
5:0.2ml of 1mg/ml Insulin B chain (oxidized form)
Column: Superdex Peptide 10/300
Flow rate: 0.4ml/min, 4 °C
Buffer:20mM Tris, 100mM KCl, 6M GnCl, pH7.5
C21Mms6 (Fraction B6:11-11.5ml)

Fig 2

Fig 3: C21Mms6 interacts with His-Mms6. Shown is the SDS-PAGE gel of 40 μM His-Mms6 incubated with or without 800 μM of C21Mms6 in 20 mM Tris, 100 mM KCl, pH 7.5 at 25 ℃ for 1 h followed by centrifugation at 14000 g for 15 min. M: Protein Marker (from top to bottom: 54 kDa, 42 kDa, 34 kDa, 26 kDa, 17 kDa, 10 kDa). S: Supernatant. P: Pellet. The gel shows that when mixed with C21Mms6, both His-Mms6 and C21Mms6 were found in the pellet (right panel). His-Mms6 alone did not precipitate under the same experimental conditions (middle panel). His-Lcn2 which has the same His-tag as His-Mms6 was used as control and no precipitation was found. These results indicate that the precipitation of His-Mms6 was caused by the interaction between free C21Mms6 and Mms6 (probably the C-terminal domain of Mms6) and not with the His-tag.

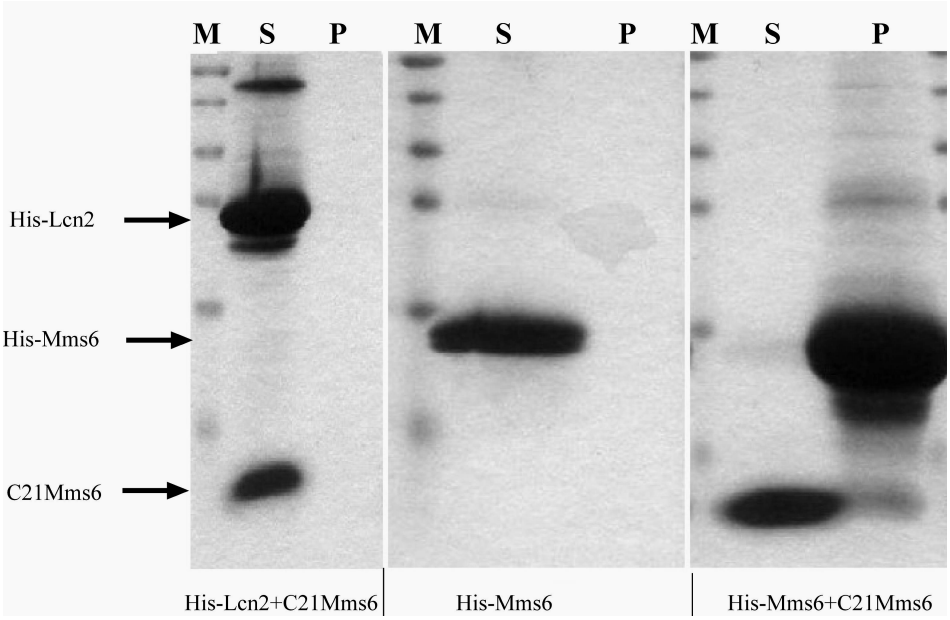

Fig 3

Fig 4: Analytical ultracentrifugation (raw data). One half mL of 0.46 mg/mL (A280=0.702) His-Mms6 in 137 mM NaCl, 2.7 mM KCl, 4.3 mM Na_2HPO_4,1.4 mM KH_2PO_4, pH 7.2 was loaded into the cell and placed in an AN60 rotor in a Beckman Proteome Lab XL-A Protein Characterization System (Beckman) for centrifugation. The time-dependent sedimentation of His-Mms6 was monitored at 280 nm, 65,520 x *g*, 4℃ for 2 h.

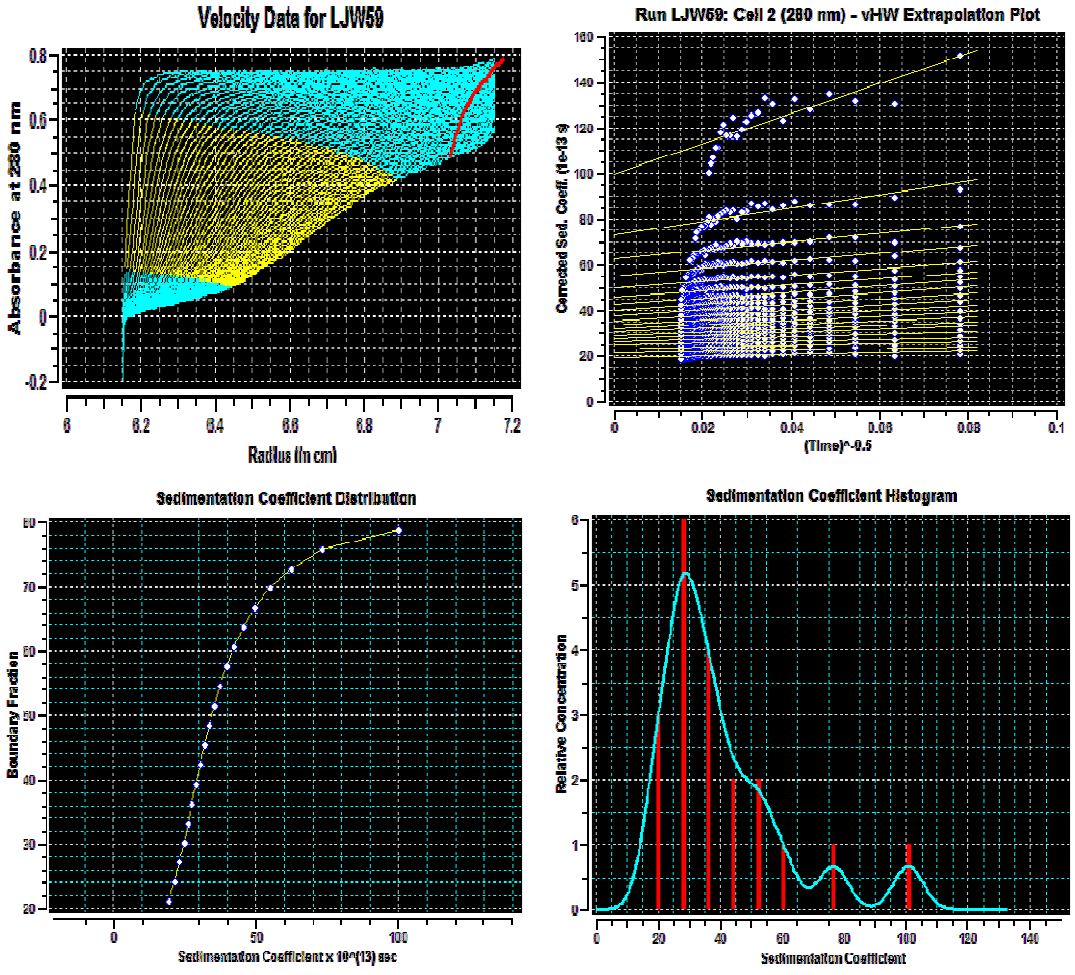

Fig 4

Fig 5: Comparison of the binding of ferric citrate for His-Mms6 and His-m3Mms6 measured by fluorescence spectroscopy. His-Mms6 (5 μM, ●) or His-m3Mm6 (5 μM, ▲) was incubated with ferric-citrate at concentrations ranging from 0 to 100 μM in 20 mM Tris-HCl, 100 mM KCl, pH 7.5 in separate brown test tubes for 2 h at 25 ℃ before the fluorescence measurements were taken (Ex:290 nm, Em: 345 nm).

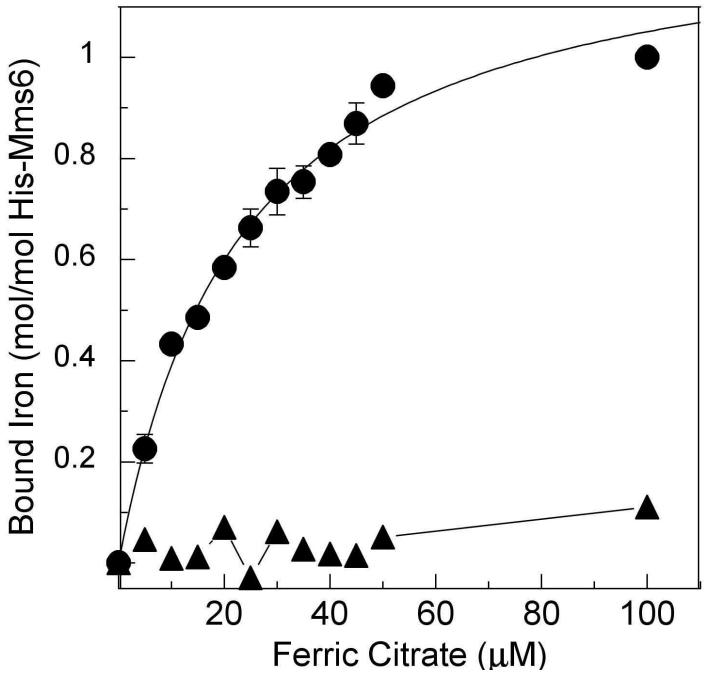

Fig 5

Fig 6: Size exclusion of His-Mms6 under denaturing condition. The quaternary structure of His-Mms6 appears quite stable as suggested by the size exclusion chromatography under denaturing condition. Shown are the chromatograms of 1 mL of His-Mms6 (0.5 mg/mL) in 4 M urea (A) or 6 M GnCl (B) run through Superdex G75 column with a flow rate of 0.4 mL/min. The chromatograms of BSA and ferritin in 6 M GnCl were used for comparison. Some of the His-Mms6 still exhibited large apparent molecular mass and appeared in the void volume of the Superdex G75 column in 4 M urea (A) or 6 M GnCl (B), 20 mM Tris, 100 mM KCl, pH7.5.

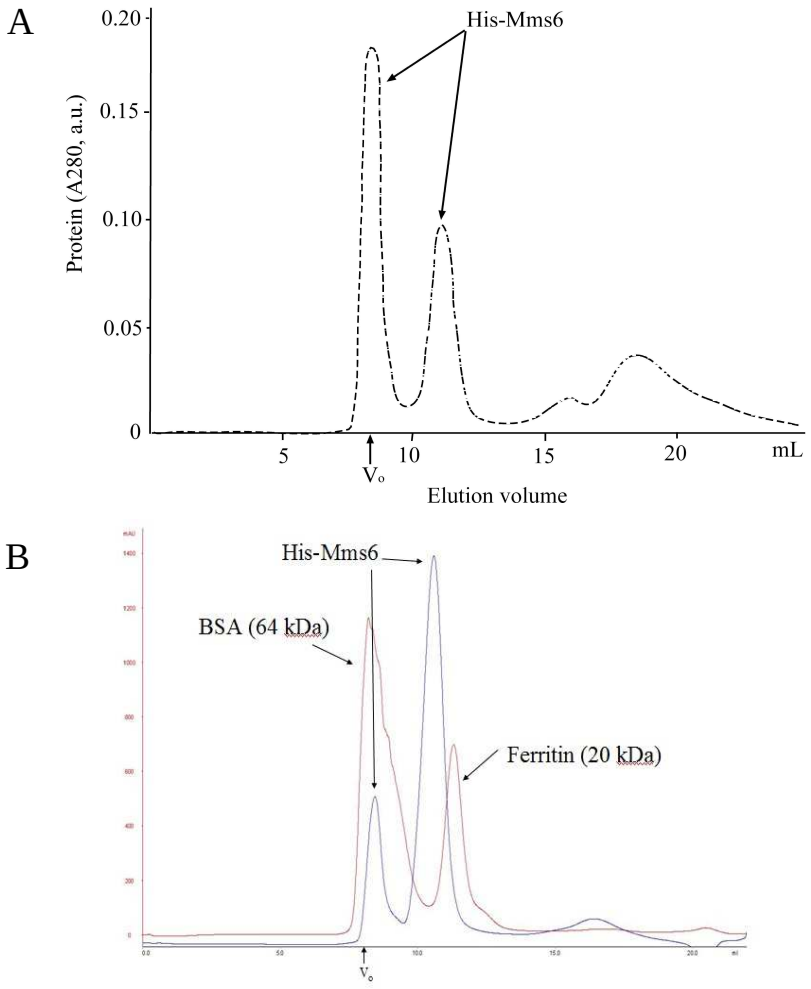

Fig 6

Fig 7: Enterokinase cleavage of His-Mms6 in the presence of detergent or under denaturing conditions. Shown are the SDS-PAGE analyses of His-Mms6 after its incubation with enterokinase (rEK) for 24 h in different buffer conditions (1xrEK cleavage buffer: 20mM Tris-HCl, 50mM NaCl, 2mM $CaCl_2$). Under these conditions, a slight shift of the His-Mms6 band was observed (A) but the western blot result (B: His-Mms6 after enterokinase cleavage detected by western blot. Lane 1,2,3 are samples of lane 2,3,4 in A respectively) indicated that the shifted bands have the His-tag still present. Two other proteins (His-Utc and His-EXFABP) which have the same His-tag and enterokinase cleavage site as His-Mms6 were used as controls to show that under these conditions the enterokinase can cleave the His-tag if the cleavage site is accessible (C).

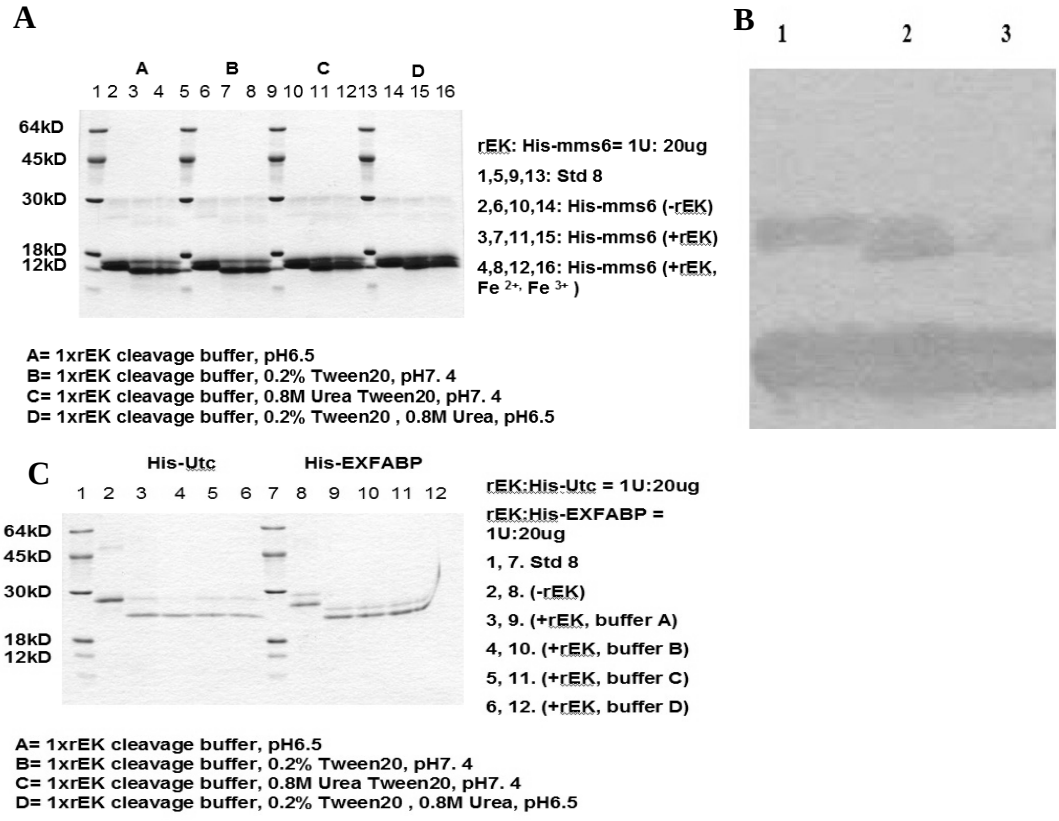

Fig 7

Fig 8: Chromatograms of standards used in Fig 4B inset (chapter 2)

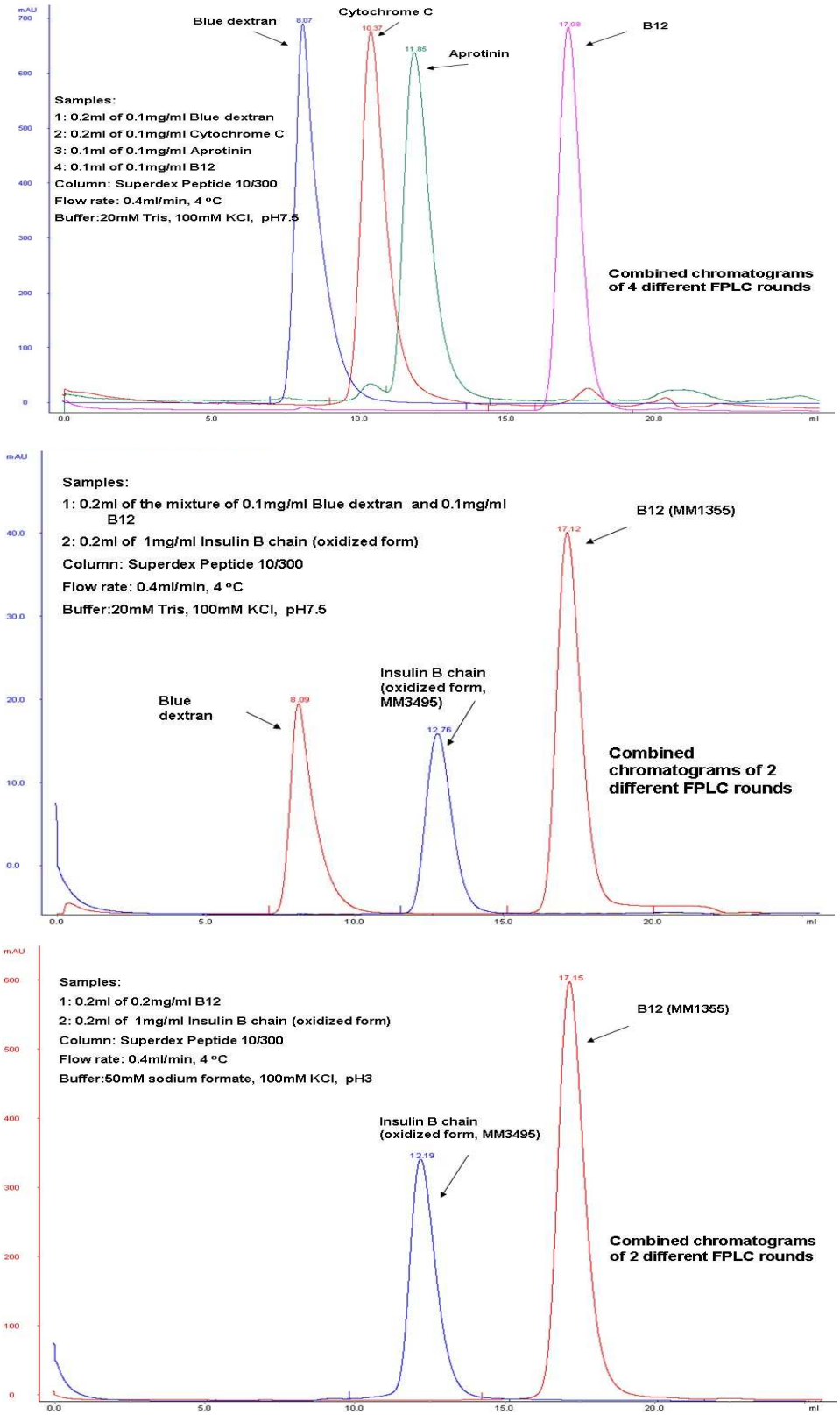

Fig 8

Fig 9: Chromatograms of the rerun of the void volume of His-m2Mms6 and His-m3Mms6 from Superdex G75 column (Fig. 3A, chapter 3). A: His-m2Mms6. B: His-m3Mms6.

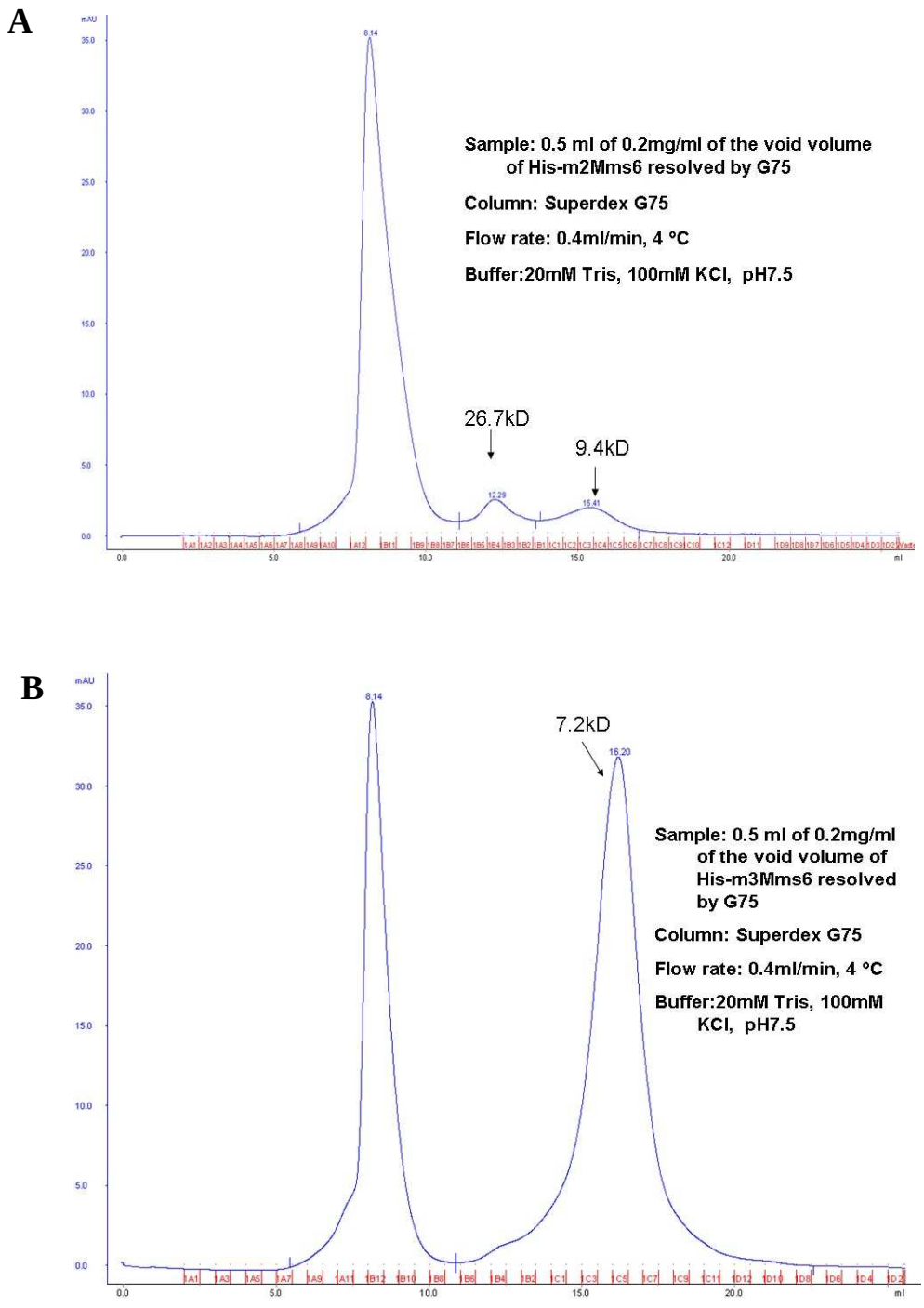

Fig 9

Fig 10: His-Mms6 specifically binds Fe^{3+} not Fe^{2+} (Data from Wenjie Wang and David Vaknin). Ferric chloride hexahydrate ($FeCl_3 \cdot 6H_2O$) and ferrous chloride tetrahydrate ($FeCl_2 \cdot 4H_2O$) each in 20 mM Tris, 100 mM KCl, pH 3 was used as the Fe^{3+} and Fe^{2+} bulk solutions respectively. Prior to taking X-ray measurements, an isotherm, in which the film was compressed at rate of $1Å^2$ per molecule per min in a Langmuir trough maintained at 20°C, was determined in order to make the film maximally compact. X-ray studies were carried out on the Ames Laboratory Liquid Surface Diffractometer at Advanced Photon Source (APS, 7.3 KeV). A beam of monochromatic x-ray selected by a downstream Si double crystal monochromator is deflected onto the liquid surface to a desired incident angle α_i by a second monochromator Ge (111). When the incident angle α_i is less than the critical angle for total external reflection, the x-ray penetration depth is ~60Å at the most. Also the photon energy of x-ray is sufficient to excite Fe elements to fluoresce (Kα and Kβ). The x-ray fluorescence intensity from the film was collected by a Vortex energy dispersive detector (EDD) at scattering vector Q_z ranging from 0.01 $Å^{-1}$ to 0.03 $Å^{-1}$ ($Q_z = 4\pi \sin\alpha_i/\lambda$, λ being x-ray wavelength). Shown are fluorescence signals below the critical angle for 10^{-3} M $FeCl_3$ (△) or 10^{-3} M $FeCl_2$ (○) with the His-Mms6 monolayer. The signals were integrated over a Q_z range as indicated in the figures. The results suggested that His-Mms6 specifically binds Fe^{3+} not Fe^{2+}.

Fig 10

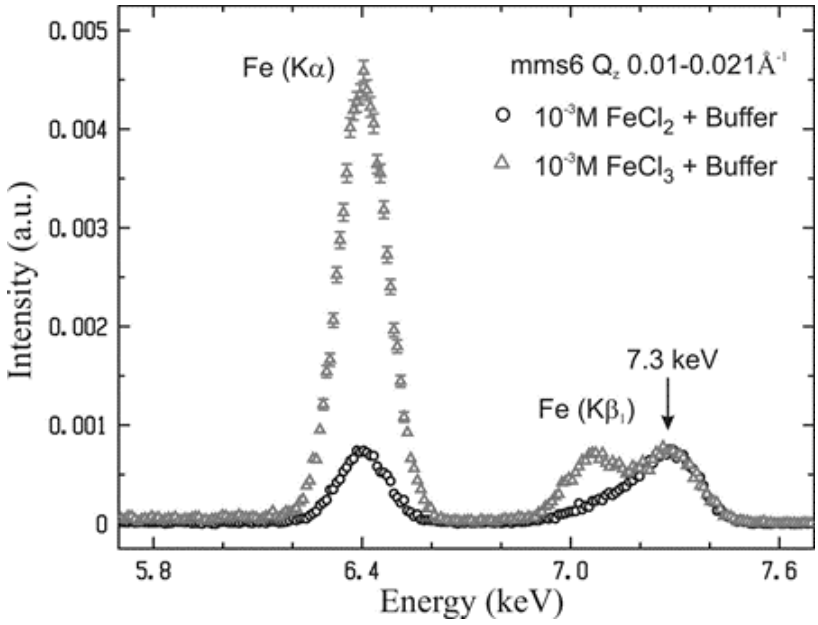

Figure 10

Table 1: The retention efficiency of His-Mms6 by nitrocellulose membranes. To check how much protein was captured by the 0.45 μm nitrocellulose membrane, 500 μL of 20 μM His-Mms6 in 20 mM Tris, 100 mM KCl, pH 3 was filtered through 0.45 μm nitrocellulose membranes followed by two consecutive 5 mL volumes of wash with 20 mM Tris, 100 mM KCl, pH 3. The flow through was collected and concentrated to 500 μL. The concentration of His-Mms6 was measured by A280. The retention efficient of His-Mms6 hold by the membrane was determined to be 89 % ±2 %.

Table 1

	Before filter by membrane (volume: 0.5mL)	**Flow through (volume:0.5mL)**	**Retention efficiency (%)**	**Average (%)**	**Standard deviation (%)**
A280	0.308	0.033	89	89	2
	0.291	0.026	91		
	0.287	0.037	87		

Table 2: N-terminal sequencing of the precipitate after proteinase K digestion of His-Mms6 for 24 h (Chapter 2, Fig. 3D, middle panel). The sample was centrifuged at *14000 g* for 1hr. The pellet was then collected and resolved by SDS-PAGE gel and transferred to membrane. The band was cut and sent for N-terminal sequencing.

Sequence of His-Mms6 (Bold italic: mature Mms6 sequence):

GGSHHHHHHGMASMTGGQQMGRDLYDDDDKDPTLGGHM***VGGTIWTGK GLGLGLGL<u>GLGAWG</u>PIILGVVGAGAVYAYMKSRDIESAQSDEEVELRDAL A***

Table 2

Cycle #	Amino Acid
1	**<u>G</u>**,D,Y
2	A,W,**<u>L</u>**
3	W,**<u>G</u>**,
4	**<u>A</u>**,
5	**<u>W</u>**,V

References

1. Ries, H. E. (1979) *Nature* **281**, 287-289
2. Smith, R. D., and Berg, J. C. (1980) *Journal of Colloid and Interface Science* **74**, 273-286
3. McFate, C., Ward, D., and Olmsted, J. (1993) *Langmuir* **9**, 1036-1039
4. Vaknin, D., Bu, W., Satija, S. K., and Travesset, A. (2007) *Langmuir* **23**, 1888-1897
5. Houmadi, S., Ciuchi, F., De Santo, M. P., De Stefano, L., Rea, I., Giardina, P., Armenante, A., Lacaze, E., and Giocondo, M. (2008) *Langmuir* **24**, 12953-12957
6. Szilvay, G. R., Nakari-Setälä, T., and Linder, M. B. (2006) *Biochemistry* **45**, 8590-8598

ACKNOWLEDGEMENTS

I would like to take this opportunity to acknowledge those who have helped me during my long journey towards the doctorate degree. First, I would like to thank my major professor: Dr. Marit Nilsen-Hamilton, whose encouragement, support and mentoring from the beginning to the end enabled me to go through everything. Without Dr. Marit Nilsen-Hamilton, my research and dissertation will be nothing like this. I would like to thank all my current and previous POS committee members: Dr. Gaya Amarasinghe, Dr. Alan DiSpirito, Dr. Surya Mallapragada, Dr. Monica Lamm, Dr. Mark Hargrove, Dr. Amy Andreotti and Dr. Paul Canfield for their kindly help and suggestions of my research. I would like to thank all my lab mates for their friendships and helps.

Finally, I would like to thank my parents and my sister for their consistent support. Special thanks go to my dear wife: Ping, and my dear son: Leo for their love and support.